# Gamma-Ray Burst Science in the Era of IACT Arrays

Ori Michael Weiner

Submitted in partial fulfillment of the
requirements for the degree of
Doctor of Philosophy
in the Graduate School of Arts and Sciences

**COLUMBIA UNIVERSITY**

2017

ABSTRACT

Gamma-Ray Burst Science in the Era of IACT Arrays

Ori Michael Weiner

In this thesis, we explore and improve on the science of gamma-ray bursts with particular attention to the very-high-energy regime. We begin by discussing Imaging Atmospheric Cherenkov Telescope Arrays (IACTs), which are the primary instruments of observation at very-high-energy gamma rays. We focus on a particular, state-of-the-art IACT array in southern Arizona: Very Energetic Radiation Imaging Telescope Array System (VERITAS). We then discuss the science of gamma-ray bursts and what can be learned from IACT observations. We follow with a couple of technical improvements, allowing one to better search for and characterize gamma-ray bursts with IACTs. The techniques focus on statistical methods for detection of transient sources, as well as angular reconstruction at arbitrary zenith angles of observation. We then use one of our new statistical methods to search for a signal in VERITAS observations of gamma-ray burst locations, with tests designed to search for particular bursts as well as for hints of emission in the entire sample of observations. We conclude that there is no evidence for a signal and follow with a discussion of a particularly interesting non-detection of GRB 150323A. We discuss the implications of this non-detection on the energetics and ambient environment of this burst. We conclude that the VERITAS observations might indicate gamma-ray bursts taking place in the dense wind of Wolf-Rayet stars.

# Contents

# List of Figures

# List of Tables

# *Acknowledgements*

This work would not have been completed without the help of many people. I will do my best to mention most of them, but there are too many to name in full.

My research has been guided by my advisor Reshmi Mukherjee, and also by Brian Humensky who served as an *de facto* additional advisor. I can now highly recommend this type of arrangement. They have both contributed to this work with their invaluable expertise in high energy astrophysics, on all topics related to this thesis.

I also thank the various former and current members of our research group, who always seem happy to help and lend their knowledge even when things are busy in their own lines of research. The Very Energetic Radiation Imaging Telescope Array System (VERITAS) community is often essential, not just by gathering the data that is used in this thesis, but also by helping in person. I thank all members and associates of the collaboration. In particular I want to thank: Andrei Beloborodov, Ari Brill, Jodi Christiansen, Valerie Connaughton, Manel Errando, Daniel Nieto, Andrii Petrashyk, Deivid Ribeiro, Marcos Santander, Gunes Senturk, Indrek Vurm, and David Williams. This list could go on for a while so I will stop here.

I also want to thank my parents, my sister, and my friends at Columbia University and elsewhere for all forms of help and support during my graduate school years.

# Introduction

Gamma-ray bursts (GRBs) were discovered accidentally in the 1960s by the VELA satellites (Klebesadel et al., 1973). They are the brightest sources of electromagnetic radiation known in the universe, releasing an energy on the order of $10^{51}$ erg in a short timescale of seconds to minutes (as observed on Earth). At least some events have been definitively associated with a supernova, and some others–shorter in timescale–are believed to be the result of mergers of compact objects. The underlying mechanisms responsible for the great variability and versatile nature of the observed prompt emission light curves are still largely unkonwn (Kumar and Zhang, 2015).

Very high energy (VHE) gamma-rays have yet to be detected from a GRB. This is likely due to a combination of technical constraints (slewing time, limited field of view), and the scattering of distant VHE gamma-rays by the ambient extragalactic background light, which greatly attenuates distant gamma-ray sources. A detection of VHE emission is a crucial aspect of model verification, and in particular can allow one to gain insight into the properties of the circum-burst medium (CBM) as well as the energetics of the burst.

This work begins with an introduction to VHE astronomy and gamma-ray burst science. In Chapter 1 we introduce the basic techniques and instruments that observe the gamma-ray sky,

with a special focus on the Very Energetic Radiation Imaging Telescope Array System (VERITAS), an array of Imaging Atmospheric Cherenkov Telescopes (IACTs) located in southern Arizona. In Chapter 2 we summarize some of the most important results on gamma-ray bursts obtained since they were first discovered in the 1960s. We then discuss processes that might lead to VHE emission, as the ejecta of the burst interact with the ambient medium, and what might be learned from either a detection or a non-detection of such emission.

The following chapters contain our original work: we first focus on improving IACT capability for detecting and analyzing GRBs. We then use our new techniques to analyze promising GRB data observed by VERITAS and to interpret the results.

In Chapter 3, we discuss the development of a novel test statistic for detecting and characterizing transient and variable gamma-ray sources, by use of maximum likelihood estimation. We first tackle the case of a time-independent background to derive a fundamental and elegant test statistic, and later expand our technique to a more realistic case involving IACT background rates which could change during the course of an observation. In Chapter 4, we discuss the implementation and testing of this technique on VERITAS software, by use of both data and Monte Carlo simulations.

In Chapter 5, we explore ways of improving the angular reconstruction of events, with particular attention to observations conducted at large zenith angles. GRBs are known to occur isotropically in the sky, and thus most VERITAS GRB observations happen at what we consider large zenith angles ($> 45\,\mathrm{deg}$). Observation of other, non-transient, gamma-ray sources at large zenith angles are typically avoided due to their detrimental effect on IACT sensitivity. We generalize on work done by others for angular reconstruction at large zenith angles, and test

a new approach that combines multiple algorithms into a single one for optimal response in a variety of circumstances.

In Chapter 6, we select a collection of promising VERITAS observations and analyze them using our time-dependent test statistic. We design *a priori* collective statistical tests that could extract a potentially weak signal present in multiple bursts. We find no detection in any individual observation or collective test. We then focus our attention on the particularly limiting non-detection of GRB 150323A. We discuss the upper limit obtained for this burst first in an empirical context, showing that it is fainter than one would expect from established GeV results. Then, we discuss how the upper limit constrains the CBM environment and the energetics of this burst.

# Chapter 1

# IACT array technology, with an emphasis on VERITAS

## 1.1 Introduction

The current generation of Imaging Atmospheric Cherenkov Telescope (IACT) arrays are the product of a rich history of experimentation in an attempt to observe and characterize astrophysical gamma-rays (Weekes, 2006).

In 1948 P. Blackett calculated that about 0.01% of the night-sky light is produced by Cherenkov radiation derived from cosmic-rays (Blackett, 1948). The process through which this happens is depicted in Figure 1.1: the incoming cosmic-ray particle produces a cascade of charged ultra-relativistic particles, travelling faster than the local (atmospheric) speed of light and producing

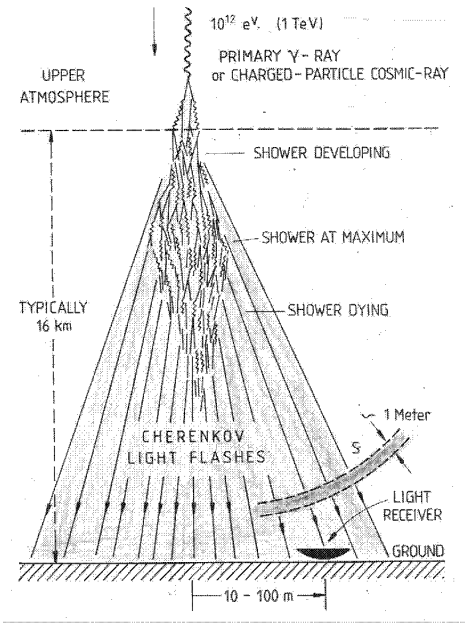


FIGURE 1.1: A cartoon of cosmic-ray-produced Cherenkov radiation, drawn by J. V. Jelley in 1993 and displayed by T. Weekes in Weekes (2006). A cosmic-ray or $\gamma$-ray impinges on the atmosphere and produces a shower of relativistic particles, some of which charged. The charged particles in the shower produce Cherenkov radiation which can be detected on the ground by a simple dish and receiver.

Cherenkov radiation as a result (Cherenkov, 1934). This emission can be detected through a simple setup such as a parabolic mirror and a photomultiplier tube.

The first such detection of Cherenkov light from cosmic rays is due to W. Galbraith and J. V. Jelley in their groundbreaking experiment in 1952 (Galbraith and Jelley, 1953). The experimental setup was remarkably simple with a small parabolic mirror and a photomultiplier tube placed inside of a dustbin (Figure 1.2). The detector was placed inside of an existing array of Geiger-Müller (G-M) tubes. Through a series of tests using an oscilloscope and a trigger connection to the G-M tube array, Cherenkov radiation was found and was strongly (and significantly) correlated to radiation detected by the G-M tubes.

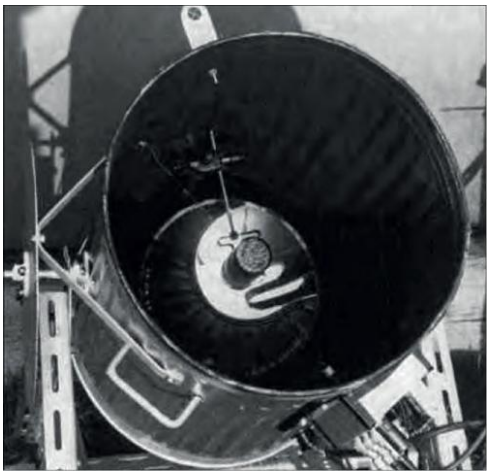

FIGURE 1.2: The detector used by Galbraith and Jelley for the first detection of Cherenkov radiation produced by cosmic rays. It consists of a parabolic mirror and a photomultiplier tube at its focus, placed inside of a dustbin for protection from ambient light. Taken from https://timeline.web.cern.ch/air-cherenkov-discovery-galbraith-jelley.

This new approach to detecting cosmic-rays had a lot of promise. One principal reason is the ability of optical detectors to observe a narrow field of view. An ability to observe Cherenkov light in a particular direction (taking into account the highly directional nature of atmospheric Cherenkov radiation) is very appealing in terms of the possibility of detecting sources of gamma-rays and characterizing their physics.

One major hurdle stood in the way of Cherenkov astronomy: It was already well known at the time that charged astrophysical cosmic-rays vastly outnumber gamma-rays (Cronin, 1999). Since charged particles are bent in magnetic fields on their way to Earth, they do not provide easily useful information on their direction of origin and on the physical nature of their sources. They also make it exceedingly difficult to detect gamma-ray sources, by creating a large Poisson-distributed background.

This gamma-ray to cosmic-ray (signal to noise) ratio meant that it took a much more sophisticated setup than the one used by Galbraith and Jelley to first detect an astrophysical source. The main challenge was to discriminate between showers produced by gamma-rays and cosmic-rays. This was eventually achieved by using telescope images of showers rather than traces of a single photomultiplier tube, in conjunction with sophisticated simulations of shower development to allow one to classify those images (Hillas, 1985). The first gamma-ray source detection was of the Crab Nebula in 1989 (Weekes et al., 1989). It was achieved using the Whipple telescope (Kildea et al., 2007).

Modern IACT arrays involve multiple telescopes, using their stereoscopic imaging to better determine the direction, energy, and type (gamma-ray or cosmic-ray) of shower observed. Both technique and instrumentation are still rapidly evolving. This chapter will focus on VERITAS (Very Energetic Radiation Imaging Telescope Array System), a state-of-the-art IACT array located in Southern Arizona, USA (Krennrich et al., 2004). Through exploration of VERITAS instrumentation, software, and technique, we will attempt to provide a detailed overview of how Cherenkov astronomy is done today.

## 1.2 The fundamental processes: extensive air showers and their Cherenkov radiation

Before we begin with an exploration of the VERITAS instrument, we will briefly discuss two vital physical aspects of the experimental process: the development of extensive air showers

and Cherenkov radiation. For more detailed information, particularly on the air shower development, we suggest Aharonian et al. (2008).

### 1.2.1 Extensive air showers

Extensive air showers can be the result of a cosmic-ray or gamma-ray impinging on the atmosphere. As we shall see, those different types of showers are (mostly) distinguishable in theory.

A high energy photon entering the atmosphere (henceforth known as a *primary* photon), with an energy exceeding two electron rest masses (about 1 MeV), will be capable of producing an electron-positron pair due to the atomic nuclei present in air. The charged particles will experience bremsstrahlung in air and will be capable of producing photons themselves.

It requires a primary with energy much greater than 1 MeV for this cycle to continue: if indeed the electron-positron pair produced by the primary photon has sufficient energy to create energetic gamma-rays through bremsstrahlung ($\gg$ 1 MeV), those will produce more electron-positron pairs, and the cycle will continue (when the energy of the electron-positron pairs drops sufficiently, ionization losses will compete with bremsstrahlung, and the shower will come to a halt). The exact development of the shower will depend on the primary energy, composition of the atmosphere, and statistics that are inherent in particle interactions. Figure 1.3 shows a simulated Monte-Carlo shower for a 300 GeV primary entering the atmosphere. Experimentally speaking, it is very difficult to observe showers from primary photons of less than a few tens of GeV. Their distance, faintness, and the abundant night sky background is enough to make them difficult to see, let alone reconstruct (i.e. determine their primary energy and direction).

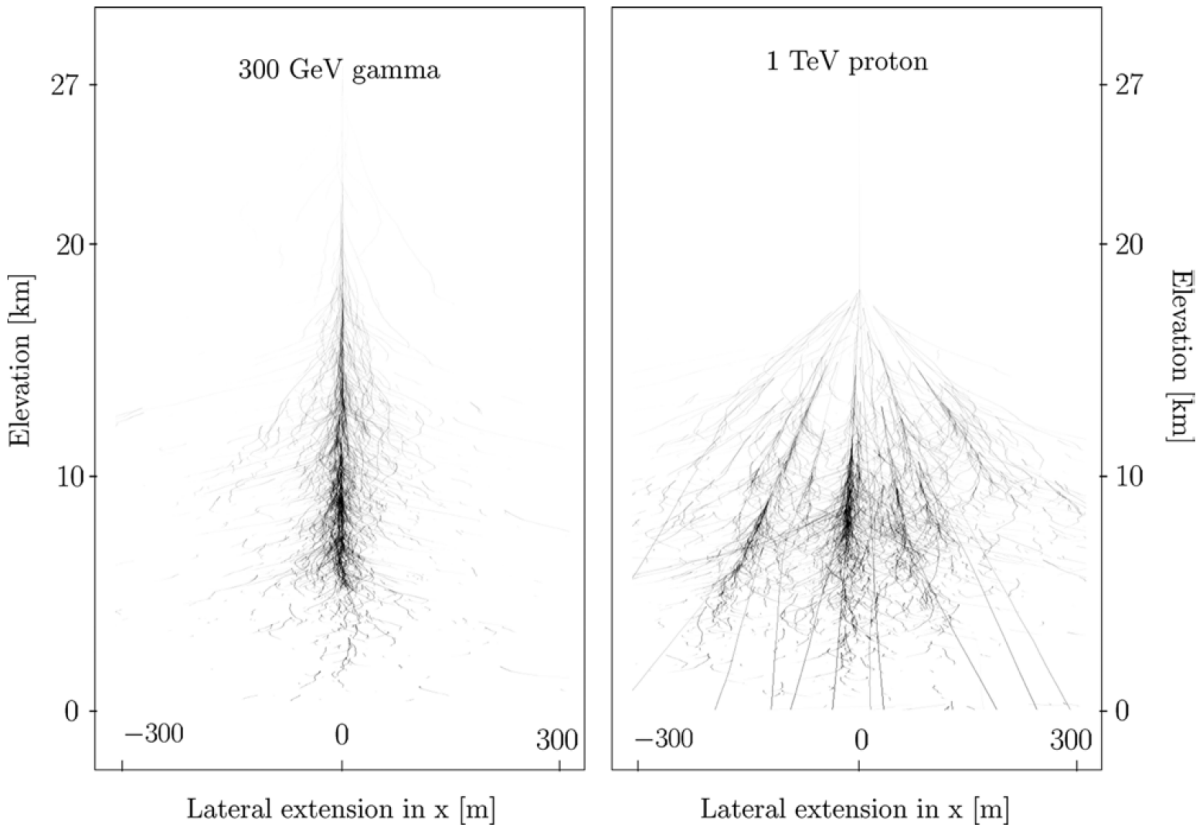


FIGURE 1.3: Side-view images of extensive air showers, produced by a Monte-Carlo simulator. The lines correspond to tracks of charged particles. **Left:** EAS originating from a primary gamma-ray with energy 300 GeV. **Right:** EAS originating from a primary proton (cosmic-ray) with energy 1 TeV. From Aharonian et al. (2008).

A primary high energy cosmic-ray proton or nucleus will generally fragment nuclei in air as well as produce pions, both neutral and charged. The pions will generally have relatively large transverse momentum, as opposed to an electron-positron pair produced by a high energy photon–a feature that is key in rejection of the cosmic-ray background. Neutral pions will decay into high energy gamma-rays which will initiate their own showers by the same process we described for a primary gamma-ray. The charged pions will decay into muons and neutrinos. The high energy muons will often reach all the way to the ground level without interacting, producing

Cherenkov radiation (see § 1.2.2) in the process and creating a significant source of background. Figure 1.3 shows a simulated shower of a 1 TeV proton, demonstrating the dramatic effect the transverse momentum of the pions has on the structure of the shower. While this typical example can be identified by a Cherenkov telescope, it is impossible to distinguish all cosmic-ray showers from gamma-ray showers, due to proton and nuclei-induced showers that happen to evolve in a way that looks similar to a gamma-ray shower (Sobczyńska, 2007), as well as some electron-induced showers that are generally very similar to photon-induced showers (though some work has been done on attempting to separate the two; see for example Sahakian et al. (2006)). Thus Cherenkov telescope arrays always have to cope with some level of irreducible cosmic-ray background.

### 1.2.2 Cherenkov radiation

Cherenkov radiation was initially observed in experiments involving radioactivity as a faint blue light, and was poorly understood. Most of the early work in understanding the effect is due to Cherenkov, Frank, and Tamm (Jelley, 1955).

When a charged particle travels through a dielectric medium, it polarizes nearby atoms and molecules. In any given small region, or molecule, the polarization will very quickly relax, producing a quick pulse of radiation. One can show that these pulses will interfere coherently if and only if the charged particle travels faster than the local speed of light. The angle at which they interfere will depend on the refractive index of the medium as well as the velocity of the charged particle.

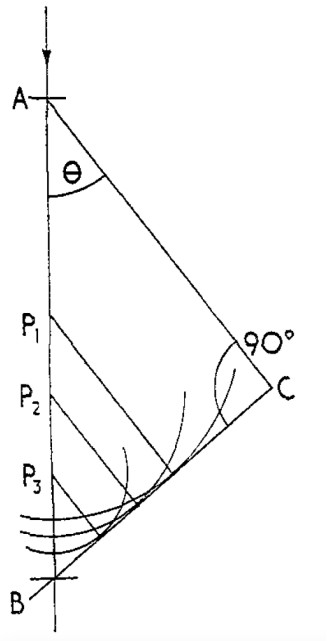


FIGURE 1.4: From Jelley (1955). A diagram demonstrating the constructive interference responsible for Cherenkov radiation (more information in the text).

The geometry of the Cherenkov effect is demonstrated in Figure 1.4. The charged particle travels in a straight line from point A to B at a velocity given by $\beta c$, where $c$ is the speed of light in vacuum. Consider two pulses of light originating at nearby points along the line AB, such as the point P1, and a slightly farther point a distance of $\Delta x$ farther down the line (much closer than P2). We would like to solve for an angle $\theta$ at which the spherical wavelets (pulses) interfere constructively. Since the form of the wavelets (in phase an amplitude) should be identical, it is sufficient that we require the wavelets to arrive at a point at the exact same time. We suppose a point of interference is much farther away from the charged particle than $\Delta x$, thus simplifying the geometry (since $\Delta x$ is very small, this does not require a large distance). This fact allows us to easily solve for the Cherenkov angle by equating the time it takes the particle to travel the distance $\Delta x$ with the extra time the light from point P1 takes to reach a far away

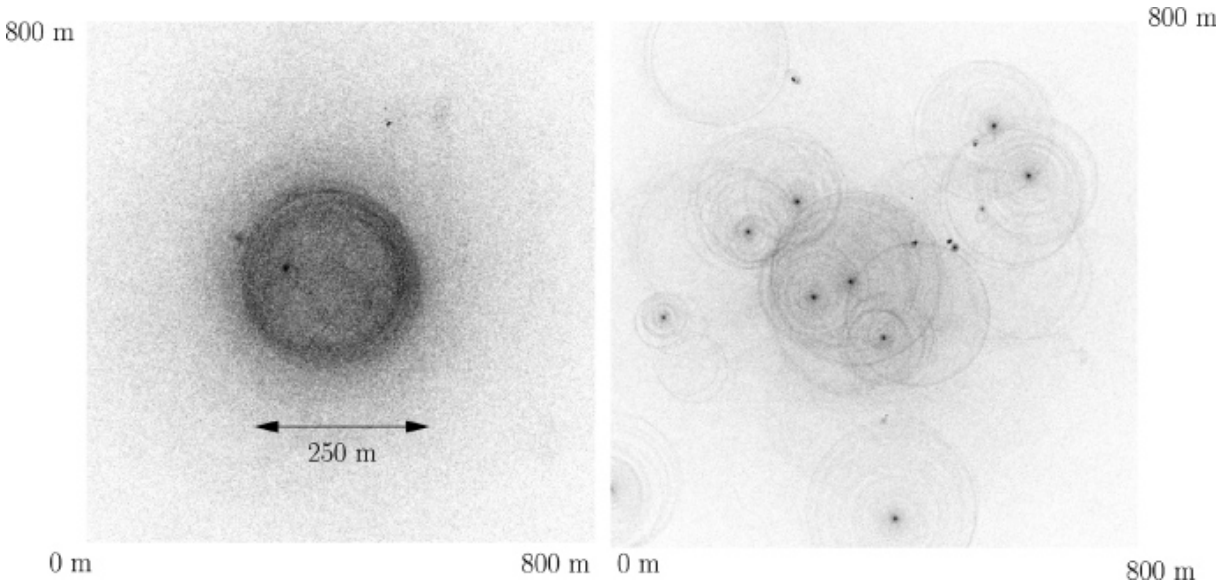


FIGURE 1.5: From Aharonian et al. (2008). Simulation of the Cherenkov light pool of an EAS. **Left:** Light pool from a 300-GeV photon-induced shower. **Right:** Light pool from a 1-TeV proton-induced shower. One can again see the effect of the transverse momentum of the pions on the angular extent of the proton shower.

point: $\frac{cos(\theta)\times\Delta x}{c/n} = \frac{\Delta x}{\beta c}$, giving $\theta = cos^{-1}(\frac{1}{\beta n})$, where n is the refractive index of the material.

The Cherenkov wavefront will appear as a cone due to the time the wavefront had to travel from each section of the particle's trajectory. In Figure 1.4, this is represented by the line BC, as can be seen by the wavefront of points P1, P2 and P3, at the time the particle reaches point B.[1]

We refer to Tamm (1939) for a full derivation of the amplitude and spectrum of the Cherenkov radiation. Those details will be less important to understanding the technique of IACT arrays.

#### 1.2.2.1 Cherenkov Light Pool

IACT experiments observe Cherenkov radiation produced by extensive air showers in the atmosphere. The atmosphere has a relatively low refractive index, and thus a small Cherenkov angle, even if the radiation-inducing charged particle travels infinitesimally close to the speed of light. For example, a typical refractive index at a height of $\sim 7$ kilometers is $1 + 2.9 \times 10^{-4}$ (Aharonian et al., 2008), giving a Cherenkov angle of about $1.4^\circ$ (if the charged particle travels at c). However, the substantial height at which the EAS develops in the atmosphere, as well the opening angle of the shower itself, can contribute to a substantial "pool" of Cherenkov light on the ground.

An IACT must be within the Cherenkov light pool to be capable of detecting it. Thus, it's interesting to note that because of the definite and narrow Cherenkov angle, a telescope imaging the shower may not see it even if it is within its field of view. This is why Cherenkov telescopes can only observe the TeV sky that resides within their field of view, and possibly about $1^\circ$ outside of it. What's perhaps even more interesting is that some extensive air showers are within the field of view, their primary is from a source within the field of view, and yet they cannot be detected by the telescope.[2]

[1] The full Cherenkov cone projection to this two dimensional diagram would also include the line mirroring BC around the AB axis.

[2] This is the main reason one should not think of a Cherenkov telescope as simply "imaging" the charged particles in the EAS.

## 1.3 Overview of the instrument

VERITAS is located in Mount Hopkins, Arizona, USA, at an altitude of 1,268 meters (Holder et al., 2011). It consists of 4 telescopes, each of which has a 12 meter diameter and of a Davies-Cotton (Davies and Cotton, 1957) design. Each telescope contains 350 aluminum-coated glass mirrors of hexagonal shape, with a camera consisting of 499 photomultiplier tubes (PMTs) and a $\sim$3.5$^\circ$ field of view (Galante, 2012). In the standard mode of operation all telescopes point to the same position in the sky. Figure 1.6 shows the array as well as an individual telescope and camera.

The amount of data that would be needed to record all information (photons) impinging the PMTs is extremely difficult to store and process. A mechanism for selecting the important times for storage and analysis is thereby implemented, using a sophisticated system of multi-stage hardware triggers (Cogan (2006); Weinstein (2007); Zitzer (2013)):

1. The first stage occurs in each telescope individually. All PMTs are connected to a constant fraction discriminator (CFD) - a device whose purpose is to find the maximum of a pulse. A threshold value for this maximum is required to activate the first level trigger. This threshold is experimentally decided and updated every few months to reflect PMT aging. The goal is to include as many possible *events* without overloading the readout hardware. An event corresponds to about 10 ns around the trigger, in what hopefully captures the Cherenkov signature of an EAS, rather than night sky background (NSB, light coming from stars and other nearby ambient sources). As the CFD threshold is lowered, too many events are in fact related to the NSB and overload the capacity of the hardware.


FIGURE 1.6: **Top:** A panoramic view of Whipple Observatory Base Camp in Southern Arizona, containing the VERITAS array. From Sentürk (2013). **Bottom:** An image of a single telescope of the array as well as its camera. The diameter of the telescope is 12 meters. The camera consists of 499 photomultiplier tubes corresponding to a field of view of approximately 3.5°. From Holder (2015).

2. The second stage trigger also occurs in each telescope individually. It requires multiple neighboring CFDs to trigger (recall each CFD corresponds to a single PMT in the camera). This trigger relies on the compact angular extent of extensive air showers compared

to that of the NSB, which is largely uncorrelated on pixel-to-pixel angular scales. The exact requirements are for 3 neighboring pixels to activate a first stage trigger within about 5 ns of each other (Zitzer, 2013).

3. The third trigger stage is an array trigger. It requires at least two telescopes to have activated the second stage trigger within a programmable time frame, between 10 ns and 250 ns. This time is usually chosen to be around 50 ns. It serves both as quality assurance, and as a way to filter muon-related Cherenkov light (Vacanti et al., 1994) from muons that are produced in extensive air showers, and which usually appear on a single telescope only.

The typical after-trigger data rates are around 300 Hz, but depend largely on choice of trigger parameters, zenith angle of observation, and other conditions such as NSB levels (for example rates can rise substantially when the Moon is above the horizon). The hardware readout capacity requires the third level trigger to be suppressed while an event is being recorded, resulting in a dead-time of approximately 10% for a rate of 300 Hz (Weinstein, 2007).

## 1.4 Modes of operation: standard runs and calibration runs

### 1.4.1 Introduction

The standard mode of operation for VERITAS relies on 30-minute long *runs* during which all telescopes in the array point to the same position in the sky, continually tracking it as the Earth rotates. However, there are some exceptions to this rule, for example during special

calibration runs and observations of extended sources. We will discuss the most pervasive types of observations without being fully exhaustive. We note that new IACT array observing strategies are constantly being discussed and researched (for example, Actis et al. (2011)).

### 1.4.2 Calibration runs

Calibration runs are typically taken during the start of an observing night, and when conditions have changed sufficiently to warrant a reanalysis. A fast LED flasher system was developed for the purpose of PMT calibration (Hanna et al., 2009). The LEDs are turned on to flash 300 times per second, and data taking is synchronized with an artificial trigger, to make sure that no external events are recorded. The response of each PMT can be monitored, and later used to correct for differences in gain and timing when data is being analyzed.

There are additional types of calibration performed occasionally on all telescopes or individual ones (for some detailed examples, see Hanna (2007)). This includes measuring mirror reflectivity, calibrating pointing monitors (small optical cameras that help measure the pointing error of every telescope), and studying the event rate as a function of CFD threshold to find an optimal setting.

### 1.4.3 ON/OFF observations

The oldest method of observing a potential gamma-ray source is to point the instrument to observe the source for an *ON* observation, and to subsequently point it to a nearby background (*OFF*) region with similar characteristics (for example zenith angle, or distance to the Moon).

This was the method of choice in the early stages of IACT astronomy when instruments lacked angular reconstruction (beyond the angular precision that is given by the entire FOV). Ideally, one would observe a much higher rate of events during the ON observation in a statistically significant manner, establish the existence of a source and analyze its properties. For more details on the statistical tools involved here, see § 1.5.3.

### 1.4.4 Camera acceptance and *wobble* observations

The ability to reconstruct the direction of an incoming gamma-ray to an accuracy of $\sim 0.1^{\circ}$ (Lessard et al., 2001) opened up new possible modes of observation. Once this was achieved, OFF observations were no longer needed at all, since the background could be sampled from an independent part of the field of view.

To come up with a good observing strategy, one has to consider that the rate of background events observed near the camera center per unit angular area is much higher than at the edges of the FOV, and in fact declines smoothly in between (Berge et al., 2007). Figure 1.7 shows this effect in both simulation and data.

This radial drop in the rate of events can be explained primarily as a result of the narrow angular distribution of Cherenkov light radiating from the imaged showers. A simple thought experiment should shed some light on this effect. One can imagine starting with a shower that is directly overhead to the telescope (resulting in a compact radially symmetric image) and shifting it in the horizontal plane, without changing its angular direction; after it has been moved by about one degree, or about 200 meters at the typical EAS height, the Cherenkov light pool will no longer cover the telescope and thus the shower will not be visible (contrary to what one

would expect based on usage of the word "imaging"). This fact alone would suggest that the rate of events will remain fairly constant until one reaches about 1 degree away from the edge of the camera, at which point it will begin to rapidly decline. However, since multiple telescopes are used and a multiplicity is required for an event to trigger the array, even showers with a directionality near the center of the FOV may fail to trigger a sufficient number of telescopes on the ground. The exact details will depend on the orientation of the telescopes on the ground, the choice of triggering parameters, as well as the energy of the shower. In general a more energetic shower will have a larger Cherenkov light pool, and will more easily trigger multiple telescopes in the array; thus the trigger rate for energetic showers will remain fairly constant near the center of the field of view. To illustrate, we show a few normalized plots of the rate as a function of radial distance–also known as *acceptance curves*–produced for different energy ranges in Figure 1.8.

It turns out to be a good approximation under most circumstances that the rate of cosmic-ray events is indeed symmetric around the camera center (Berge et al., 2007). However, some deviation can be expected, for example, due to a zenith angle effect on the brightness of a shower because of atmospheric absorption of Cherenkov photons, as well as on the interaction height, which will increase with zenith angle, thus forming a larger Cherenkov light pool on the ground.

#### 1.4.4.1 *Wobble* observations and the reflected region model

Keeping that in mind, a typical observing strategy is thus to point the telescopes slightly away from the source, typically by 0.5° (sometimes more for extended sources). This strategy, known as a *wobble* observation, allows one to construct background regions in the FOV that are of the

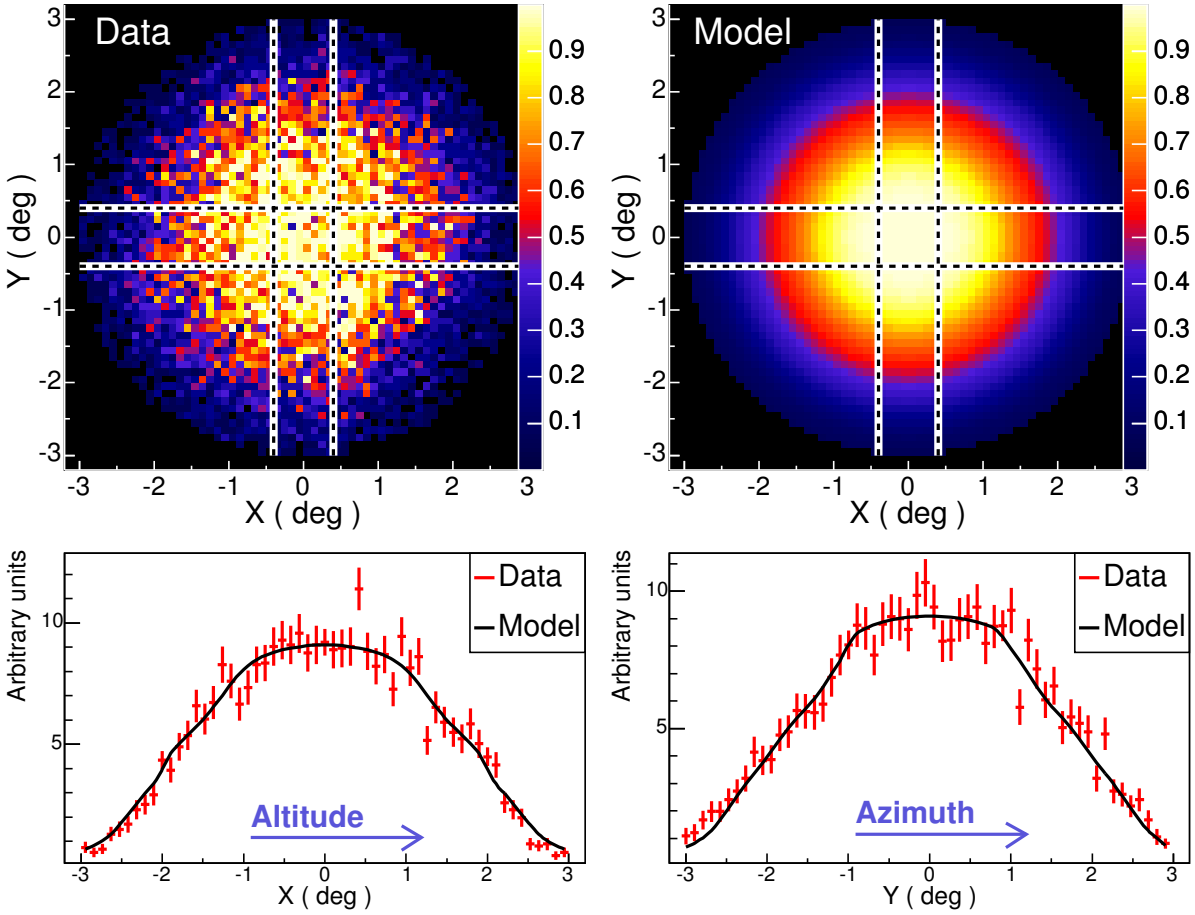


FIGURE 1.7: Inhomogeneous, radially symmetric, background rates in IACT observations. **Upper Left:** A data observation consisting of mostly background. One can see the concentration of counts in the center being much higher than at the edges with a smooth, continuous decay. **Upper Right:** The same effect is modelled in a Monte Carlo simulation of an IACT observation. **Lower Right and Left:** Using the area between the vertical (Y, Azimuth) and horizontal (X, Altitude) lines to compare data and model. The plots produced show the rate in arbitrary units as a function of displacement from the camera center, showing the data and model to be in good agreement. These curves resemble acceptance curves, but are not equivalent. An acceptance curve would use the entire area of the camera, with the rate being plotted against the distance from the center. From Berge et al. (2007).

same distance to the center of the camera, and from which (to a good approximation) one can expect similar background rates. These regions are sometimes referred to as *reflected regions*. We show an example of this construction in Figure 1.9. In an attempt to correct for small deviations from the assumed background symmetry around the center, the 0.5° displacement from the source is rotated between 4 different directions: North, South, West, and East. Each 30 minute run is taken in a different direction.

#### 1.4.4.2 Ring background model

Sometimes a reflected region analysis is either impossible or undesirable, for example, if bright stars are located near many of the possible reflected regions. Also, sometimes a very detailed understanding of the background rate is desired, and the small amount of camera area covered by the reflected regions is too small, resulting in large statistical uncertainties in the background estimation. One method that can address these concerns is the very popular *ring background model* (RBM). The model requires an *acceptance curve*, as shown in Figure 1.8. This curve identifies the rate of background as a function of the distance to the camera center. A concentric ring is then formed around the ON region and the background is calculated and normalized based on the acceptance curve. One of the author's contributions–discussed in later in this work–involves a generalization of the RBM model. We will discuss the RBM in more detail later in this chapter, and our work on generalizing it to detect transient sources in Chapter 3.

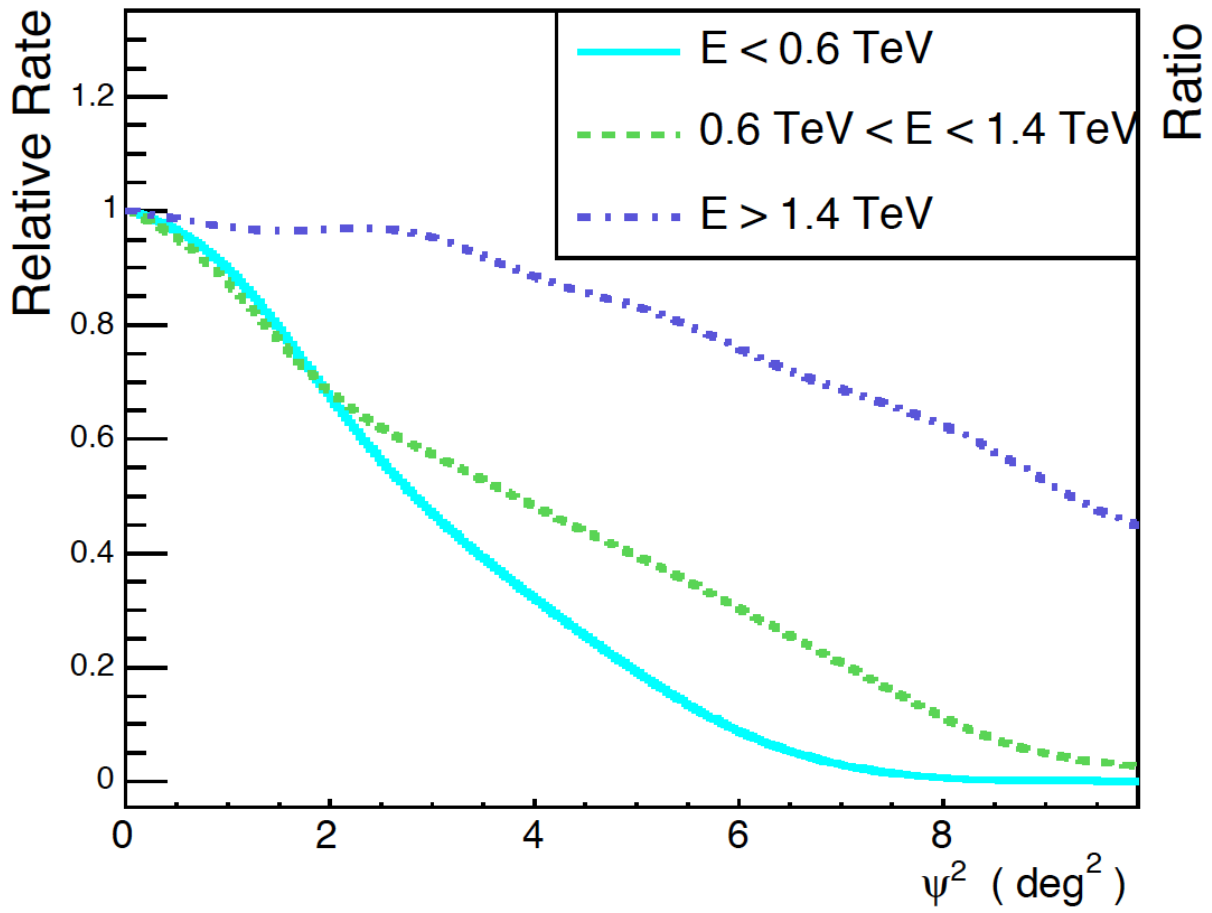


FIGURE 1.8: Acceptance curve dependence on energy of the primary. Three acceptance curves are shown, with energies indicated by the legend. A couple of effects are immediately clear. First, acceptance declines rapidly as a function of radial distance. Second, the decay appears to be much slower for energetic events. This can be explained as a result of the larger Cherenkov light pool on the ground, resulting in an almost certain triggering of multiple telescopes by a high energy shower with directionality corresponding to near the center of the FOV. From Berge et al. (2007).

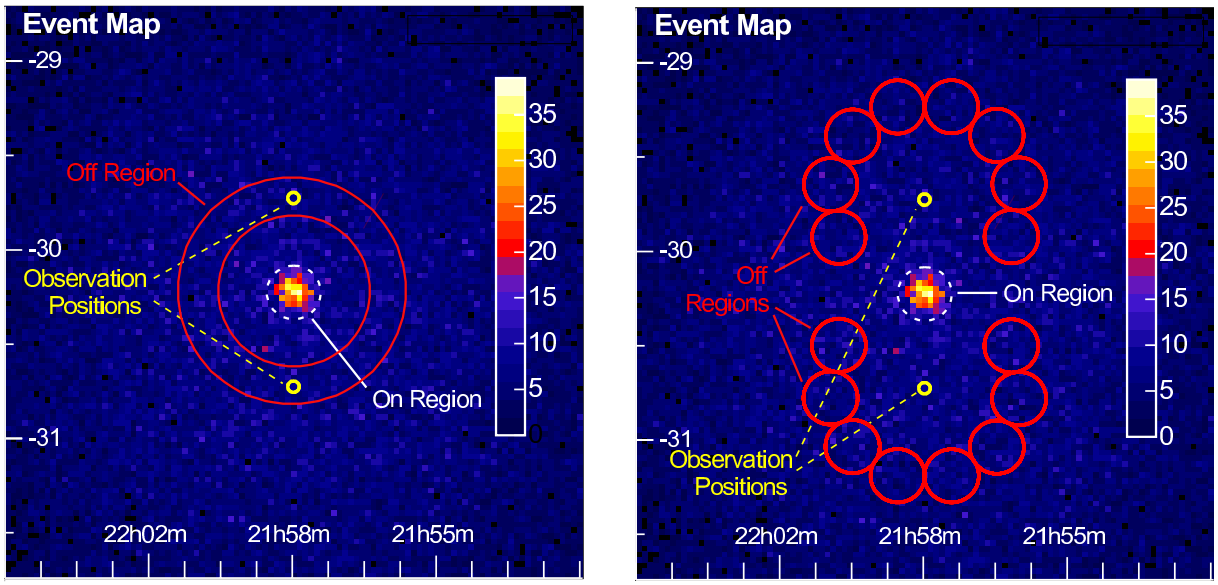


FIGURE 1.9: Two separate ways of obtaining the background of a wobble observation. Note that while the source appears in the center of the map, the observing positions are half a degree away, denoted as yellow circles. **Right:** The reflected region approach. Reflected regions are drawn symmetrically around the center of the camera for each observation. Due to approximate radial symmetry, one expects the background rates in these regions to be similar to that of the ON region. **Left:** The RBM approach. A ring is drawn concentric to the source in order to obtain the background. To interpret the background rate, one must have knowledge of the background rate as a function of the distance from the camera center (known as the acceptance curve). The ring background is normalized based on how distant each point was from the center of the FOV for each run. The strengths of this method lie in the ability to use large and flexible parts of the FOV for studying the background, as well as its symmetrical nature around the source which generally reduces systematic errors related to the assumption of radial symmetry. From Berge et al. (2007).

## 1.5 Software and analysis methods

### 1.5.1 Overview

VERITAS has two full, independent, analysis packages: Event Display and VEGAS (VEritas Gamma-ray Analysis Suite). While this duplicity can create some overhead and isn't the fastest

way to achieve results, it serves the important purpose of verifying results in addition to spotting and correcting possible errors. The basic methods used by both packages are similar. The author of this work has focused on VEGAS for both analyzing data and improving analysis methods. We will therefore focus on VEGAS in the following subsections whenever such a distinction is required.

Both VEGAS and Event Display are designed to process VERITAS data from raw after-trigger data into scientific results, which include but are not limited to:

- Detecting a source
- Estimating flux and/or fluence
- Producing an upper limit on flux or fluence
- Fitting a spectrum for a detected source
- Producing a light curve and establishing variability of a source

VEGAS does this in five stages as given in the overview below. Each stage is designed as an executable of its own and has as its input and output CERN ROOT (Antcheva et al., 2015) files. ROOT libraries are also heavily used in the C++ infrastructure of VEGAS. For more detail see Cogan (2007) and Cogan (2006).

- **Stage 1:** This stage is operated separately on calibration runs and data runs. It calculates various hardware and calibration dependent quantities, some of which are read from an online database. These quantities are then stored in a way that makes them easily accessible to later stages of analysis.

- **Stage 2:** Calculates analysis related parameters from every event in the data. This includes, but is not limited to, Hillas parameters (geometrical characterization discussed in Chapter 5). The calculation of parameters is nontrivial and involves the need to filter out noises, both ambient and electronic. For example, image cleaning has been extensively studied and is still being researched (for example, Shayduk (2013)). Applications of calculated parameters are left to later stages.

- **Stage 3 no longer exists and has been combined with (into) Stage 2.**

- **Stage 4:** The parameters that were calculated in Stage 2 are used to reconstruct the physical characteristics of the primary. These include the energy, direction, and core position (the "landing" position of the primary if it were to survive atmospheric interactions). While most events we observe are induced by charged cosmic rays, the reconstruction techniques employed here are designed for gamma-ray events and only work properly for those events. We attempt to filter out as many cosmic-ray events as possible in Stage 5.

- **Stage 5:** In this stage we attempt to filter out a large number of cosmic-ray events, using parameters obtained in Stage 2, as well as some parameters that are byproducts of Stage 4 reconstruction (the latter is only true for some types of filtering techniques, especially newer and more experimental).

- **Stage 6:** This final stage uses the events that passed the Stage 5 filtering procedure to produce meaningful scientific content. The most simple tools can plot a map of all counts received, and calculate the significance associated with an observation. There are many statistical tools employed in this stage, and more are being developed in recent years. In Chapter 4 we will discuss an implementation of the author's method for detecting and characterizing transient sources which has been implemented in this stage.

In this work we will discuss the methods in stages 4 and 6 often, as these are related to the author's work in improving IACT analysis. The author has worked extensively on both stages.

### 1.5.2 Monte Carlo simulations

Many of the techniques we use rely on the results of Monte Carlo simulations of gamma-ray events. This need arises out of the obviously complex and probabilistic nature of extensive air shower development, as well as the complexity of the noise involved in imaging those showers (including details such as mirror roughness and slight misalignment of mirror panels). Independent simulation packages have been developed for this purpose (Maier, 2007). The EAS simulator and the detector simulator are generally developed separately, and a few separate options exist for each.

When estimating a physical parameter of the primary, simulations can be used to construct *lookup tables*: tables that map parameters of the telescope images into the required physical parameter. For example, a lookup table is used to reconstruct the energy of the primary. Choosing which shower parameters to use as inputs for the lookup tables relies on physical arguments, intuition, and trial-and-error. In recent years, an inclusion of more sophisticated multivariate techniques is taking place. Techniques such as Boosted Decision Trees, Neural Networks and more are supposed to be superior to the construction of tables when used under the right circumstances, with their parameters tuned correctly (see, for example, Fiasson et al. (2010)).

Sometimes there is a favorable analytical technique for reconstruction of a physical parameter. One such example is the geometrical method for direction reconstruction, which we discuss in Chapter 5.

### 1.5.3 Significance calculations, best-fit amplitudes, and upper limits

The first robust way of statistically inferring the existence of sources and finding their amplitudes was published by Li & Ma in 1983 (Li and Ma, 1983), using maximum likelihood estimation. At the time, angular reconstruction was not available and all observations operated in the ON/OFF mode, where the telescopes observe a source for a time $T_{on}$ and then observe a nearby background region for a time $T_{off}$. Due to obvious reasons such as the desire to collect statistics on a source, the typical observation spent more time on the source than on the background region. Li and Ma define a parameter $\alpha = \frac{T_{on}}{T_{off}}$, where typically $\alpha > 1$. Denoting the number of events found within the ON and OFF observations as $N_{on}$ and $N_{off}$ respectively, they find the Gaussian significance to be (Li and Ma (1983), Eq. 17):

$$S = \sqrt{2}\left\{ N_{on} \ln\left[\frac{1+\alpha}{\alpha}\left(\frac{N_{on}}{N_{on}+N_{off}}\right)\right] + N_{off} \ln\left[(1+\alpha)\left(\frac{N_{off}}{N_{on}+N_{off}}\right)\right]\right\}^{1/2} \tag{1.1}$$

We will derive this expression using a somewhat different notation in Chapter 3, and later in the same chapter expand on this technique for detecting time-varying sources.

As IACTs developed angular reconstruction, the possibility of extracting the background from the field of view, by either using reflected regions or a ring background region, has changed the meaning of this test statistic. For one, usually $\alpha < 1$, but more importantly, the estimation of the "observing time" is done on an exposure basis. If one uses $n$ reflected regions, then $\alpha = \frac{1}{n}$, assuming all reflected regions indeed have the same exposure to background as the source region (thus neglecting differences in, for example, elevation, and absorbing small systematic errors). The exposure for a ring background is calculated using the acceptance curve. These calculations are all performed in stage 6 of VEGAS.

One important note about finding source fluences, is that the likelihood model devised by Li & Ma finds the best-fit source fluence (which we consider valid only for a 5 sigma detection) to be a very straightforward $F = N_{on} - \alpha N_{off}$, where we use units based on counts observed by the array. The fluence can be converted into physical units by introducing the effective area of the telescope array. In Chapter 3 we will see that the time-dependent generalization we derive does not appear to have an analytical solution for the amplitude of emission or fluence: they can only be found using numerical methods.

In the absence of a detection, upper limits can be interpreted using Bayesian or frequentist probability (Röver et al., 2011). The standard way to obtain upper limits in IACT observations has been strictly frequentist using a Neyman construction. There is some freedom in constructing such upper limits. The two standard approaches are described in Feldman and Cousins (1998) and Rolke et al. (2005).

### 1.5.4 Background rejection, and different levels of cuts

As previously discussed, the cosmic-ray background is the dominant component of almost every IACT observation except for when observing the brightest gamma-ray sources. This fact is true even when one only considers the angular region around the source which is bounded by the PSF of the instrument. While this is the case regardless of the quality of background rejection, it makes reducing the background a very crucial task for the sensitivity of IACTs.

The important *separation* parameter which is typically used to determine whether an EAS event is signal or background is the angular width of the image. In fact this is typically calculated

*scaled* by the expectation of how large an imaged EAS is supposed to be, relative to its brightness and reconstructed impact distance–where the expected width is found in a large sample of Monte Carlo simulations. This ratio is calculated for each telescope that has a legible image, and the mean is computed. This parameter is termed *mean scaled width* (MSW). We've seen in § 1.2.1 that wider showers are much more likely to be background events.

Other parameters that are typically used to distinguish signal to background are the length of the imaged shower as well as the reconstructed height of first interaction. There has been a significant amount of work on improving background rejection, both by including new separation parameters, and by using machine learning algorithms (e.g., Krause et al. (2017)).

The traditional technique for background rejection is make a "cut" on the value of the separation parameters, such as MSW, allowing only EAS events with less (or more) than that value to pass through the analysis. These cuts are studied extensively on gamma-ray sources with various levels of spectral steepness, and designed accordingly to perform optimally for such sources. VEGAS has three such standardized sets of cuts, termed soft (optimized for photon index[3] of around $-3.5$ to $-4$), medium ($-2.5$ to $-3$), and hard cuts (harder spectrum).

One reason that spectral steepness is so important for determining cuts is that the rate of cosmic-ray events drops very rapidly with increasing energy. A source which is expected to have a hard spectrum, can be much more easily detected by cutting away faint images, even though that is likely to filter out some signal events. Thus, for hard sources the brightness of an image can be

[3]The photon index is a measure of how rapidly the photon flux of a source declines as a function of energy, using a power law approximation (which is often a good approximation in VHE astronomy). Thus the differential flux of incoming photons per unit energy, $dN/dE$, is approximated by $Ae^{\alpha}$, where $A$ is the amplitude and $\alpha$ the photon index.

used itself as a quasi-separation parameter. Note that the signal events being filtered by a hard-source analysis are mostly low energy events (with a low image brightness), therefore causing a significant increase in the energy threshold of the analysis.

### 1.5.5 Sensitivity

Since the historic detection of the Crab Nebula, a very bright TeV emitter, IACT arrays have become capable of detecting much fainter sources. VERITAS can now detect the Crab Nebula at a 5-sigma level in about a minute of observation. Instruments with a well known background rate would be able to detect fainter sources with longer observing duration in proportionality to $1/\sqrt{T}$, however as we've seen this is not case for the Li & Ma scenario. The simple square-root-of-time formula becomes a better approximation with longer observing durations.

In Figure 1.10 we show various plots related to the sensitivity of VERITAS. All plots assume a high elevation and good weather conditions.[4] In the bottom plot, one can especially note the effect of the cuts on the energy threshold of the instrument. Hard cuts make it very difficult to detect emission at below 400 GeV, while soft cuts can detect emission at around 100 GeV, sacrificing sensitivity at higher energies. One can also note the very large effective area associated with the experiment, which is the biggest advantage IACT arrays have over satellites; this is a direct result of the typically-large Cherenkov light pool on the ground as discussed earlier.

VERITAS has an angular resolution that depends on the cuts used, the energy of the shower, and the elevation of observing. It is usually around 0.1 degrees. We will discuss the topic of angular reconstruction in detail in Chapter 5.

[4]Low elevation observing affects the sensitivity of the instrument significantly; for more details on how these conditions and other details may affect sensitivity we suggest Park (2015).

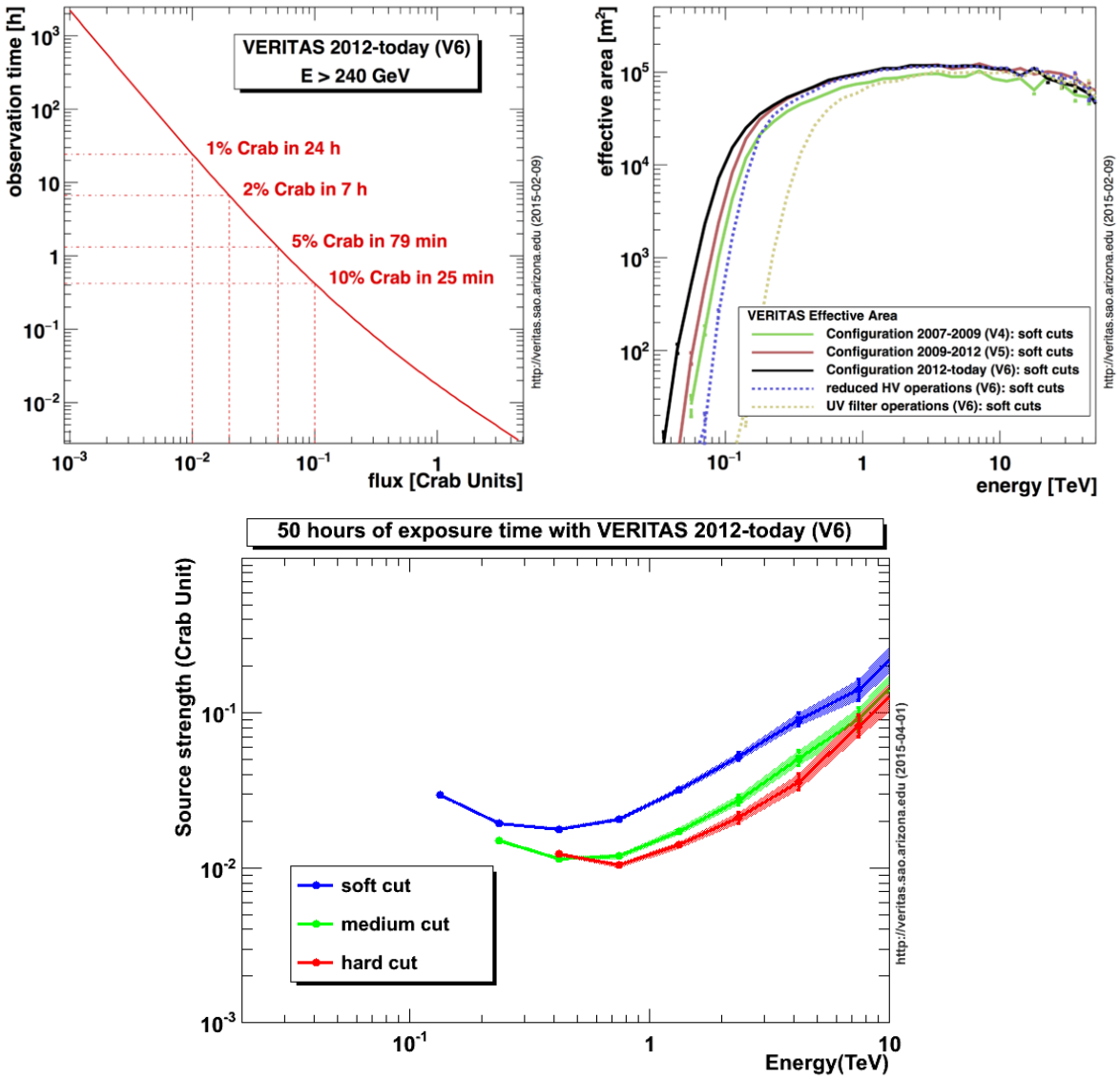


FIGURE 1.10: Various plots related to the sensitivity of VERITAS. All plots assume a high elevation observation as well as good weather conditions. **Top/Left:** A plot of the time-to-detection against source flux. **Top/Right:** The effective area of the detector as a function of energy. **Bottom:** Sensitivity is plotted against energy for three standardized sets of cuts: soft, medium, and hard. One can see the strong impact the cuts have at the lowest energies. For example, at the lowest energy bin medium and hard cuts essentially block both the signal and the noise, resulting in an increased threshold for the energy. From the official VERITAS webpage: http://veritas.sao.arizona.edu.

## 1.6 Beyond IACTs: the high energy sky

We will briefly describe some instruments that complement TeV observations by IACTs. These instruments are sensitive to radiation in nearby energy bands, and can be used to complement scientific results, as well as to trigger an IACT observation–which is usually the case in gamma-ray burst observations (see § 2.4).

We first note that other IACT arrays are currently in operation, which have comparable sensitivity to VERITAS. Those are H.E.S.S. (Hinton, 2004) and MAGIC (Cortina et al., 2009), operating out of Khomas Highland of Namibia and the Canary Islands of Spain, respectively. There is also FACT (Bretz et al., 2013), a Cherenkov Telescope based on silicon photon detectors, thus being versatile enough to operate in various conditions, including during bright moonlight. FACT was designed in part to test the feasibility of silicon detectors for the next generation IACT array, the Cherenkov Telescope Array (CTA). CTA will operate out of two sites and will have a sensitivity exceeding current generation IACT arrays by about an order of magnitude, as well as other advantages such as a wider field of view and a lower energy threshold (Actis et al., 2011).

### 1.6.1 The Fermi Gamma-ray Space Telescope

The Fermi Gamma-ray Space Telescope (McEnery et al., 2012) is a space observatory that was launched in 2008 with two detectors on board, the Large Area Telescope (LAT) (Atwood et al., 2009) and Gamma-ray Burst Monitor (GBM) (Meegan et al., 2009).

LAT is based on the pair-conversion technique, whereby layers of thin high-Z metal induce a crossing gamma-ray to produce an electron-positron pair. A particle detector and calorimeter can then find the pair and estimate the energy of the primary gamma-ray. LAT is sensitive at energies of approximately 20 MeV to 300 GeV. The angular resolution is several degrees at the lowest energies and improves to about 0.1 degrees at the highest energies. The effective area is limited by the size of the detector, to about one square meter. LAT covers about 20% of the sky at any given moment, and the entire observatory rotates in a way that exposes the entire sky every two orbits, or around three hours (the LAT is at near-earth orbit with a period of about 90 minutes).

GBM, in contrast, is designed to observe the entire visible sky at any moment. It is sensitive in the energy range of about 8 keV to 40 MeV, and ideally suited to search for gamma-ray bursts. It computes their position based on relative intensities in sensors that are oriented in different directions, thus having rather crude localization of about 5 degrees. We note that while GBM is a major contributor to alerts that trigger a VERITAS observation of a burst, the Swift space observatory[5] (Gehrels et al., 2004) can often deliver better localization that is suited for an IACT field of view. VERITAS will follow alerts generated by both observatories and a few others, with an expanding list of instruments that are sending burst alerts and locations through the GRB Coordinates Network (GCN) (Barthelmy, 2000).

One last note, is that while the instrument is configured to allow LAT to observe a source continuously, if not blocked by the Earth, this is usually not used and is reserved for the most

[5]The Swift space observatory has three detectors on board: The Burst Alert Telescope (BAT) which covers a large fraction of the sky and can locate bursts with a good accuracy of a few arc-minutes, using hard X-ray detectors. The X-ray telescope provides better spectral and temporal information at softer X-rays, as well as a more accurate position of a few arc-seconds. The Ultraviolet/Optical Telescope (UVOT) can detect a GRB afterglow at optical and ultraviolet energies.

bright or otherwise interesting gamma-ray bursts.

### 1.6.2 High Altitude Water Cherenkov (HAWC) observatory

The High Altitude Water Cherenkov (HAWC) observatory has become recently operational (Smith, 2015), replacing its much less sensitive predecessor, Milagro. HAWC consists of 300 water-filled tanks, designed to induce and detect Cherenkov radiation by particles from extensive air showers that survived the atmosphere to the detector, at an altitude of 4100 meters in Sierra Negra, Mexico (DeYoung, 2012). Each water tank contains 4 PMTs for this purpose. The observatory is most sensitive at energies above 1 TeV, since a lower-energy EAS is unlikely to survive to its altitude. At the highest energies of about 10 TeV, the angular resolution is between 0.1 and 0.2 degrees. As a water Cherenkov observatory, HAWC can operate during sunlight and essentially any other ambient conditions, therefore being most suitable for detecting a nearby, powerful GRB. To date, there has not been any detection of a gamma-ray burst by a water Cherenkov observatory.

# Chapter 2

# Gamma-ray bursts

## 2.1 Introduction

Gamma-ray bursts (GRBs) were discovered accidentally in the 1960s by the Vela satellites (Klebesadel et al., 1973), which were originally intentioned for the monitoring of nuclear tests in the atmosphere and in space. While much progress has since been made on understanding their origin–which is attributed to supernovae and the merging of compact objects–the internal mechanism responsible for the GRB initial radiation output (also known as the prompt radiation) is still largely unknown (Kumar and Zhang, 2015). This radiation is characterized by intense and irregular behaviour over a short time period; it tends to be composed of multiple pulses without clear periodicity. The prompt emission is generally found in the keV-MeV range, but GeV emission has been observed by Fermi-LAT for several bursts (Ackermann et al., 2013). The energy output in this prompt phase is typically around $10^{51}$ erg, making them the most luminous events known in the universe. In Figure 2.1, we show a collection of prompt GRB

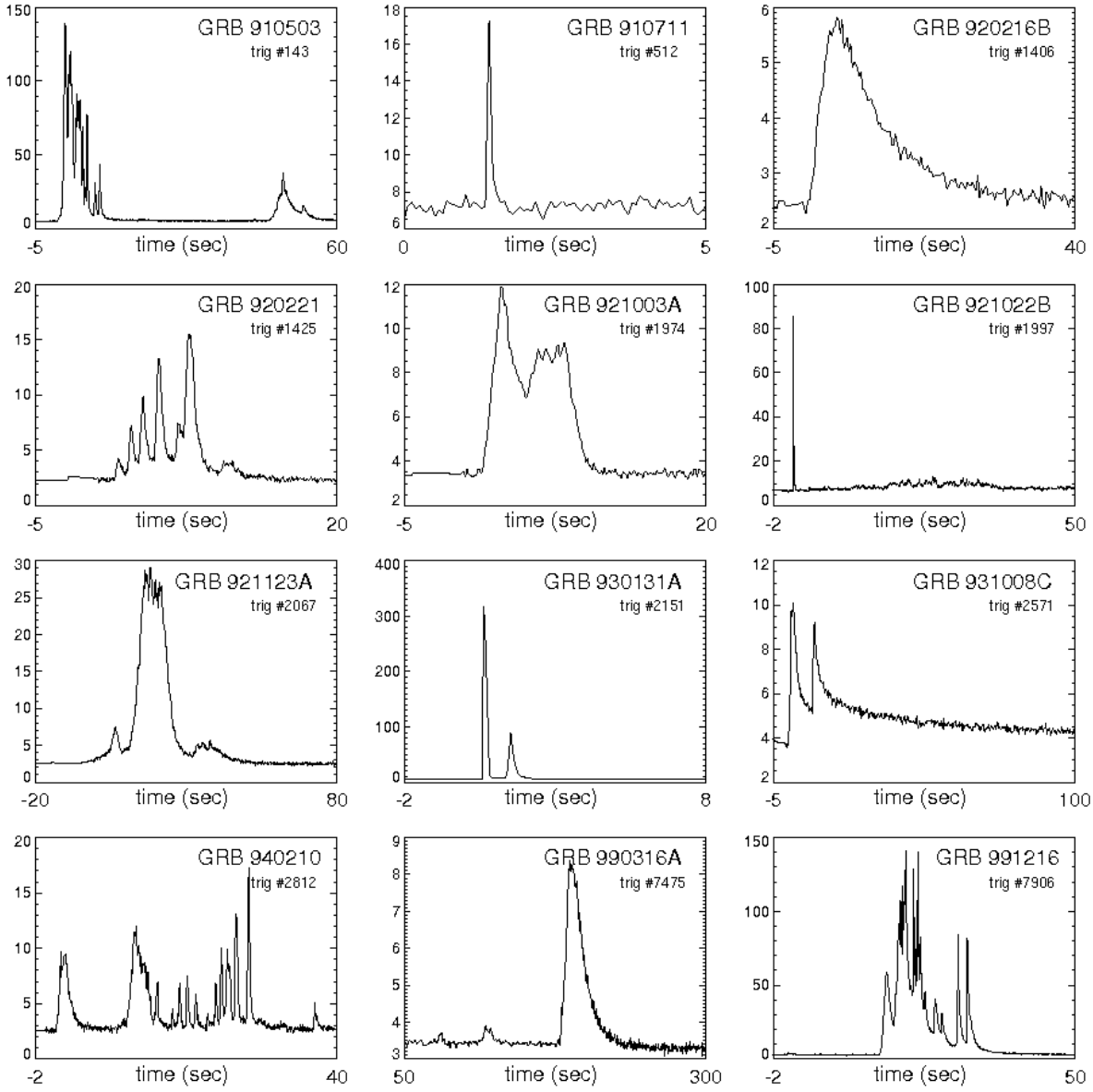


FIGURE 2.1: A collection of GRB light curves observed by the Burst and Transient Source Experiment (BATSE), composed by Daniel Perley (2009). This collection shows the versatile nature of these light curves, as well as the rapid variations that occur within most.

light curves observed by the Burst and Transient Source Experiment (BATSE) (Paciesas et al., 1999).

GRBs exhibit an afterglow which has been observed in radio, optical, X-ray, and GeV gamma-rays (Panaitescu and Kumar, 2001). Both the optical and gamma-ray afterglow fluxes appear to temporally decay as a power-law. In particular, studies of Fermi-LAT light curves in the GeV energy range show the decay index to cluster around -1 (Ackermann et al., 2013). The afterglow radiation is produced by the relativistic ejecta of the burst interacting with the ambient medium, which can lead to a significant amount of TeV emission through inverse Compton scattering, as we will discuss later in this chapter.

Gamma-ray burst sky coordinates have been observed by imaging atmospheric Cherenkov telescope arrays (i.e., the burst locations were followed up after satellite detection, see § 2.4), and are considered a high-priority target. None has been detected by any IACT array as of this date (e.g., Acciari et al. (2011)). Water Cherenkov detectors which are most sensitive at energies above $\sim$10-TeV have also failed to detect any of the bursts that were in their field of view (Abdo et al., 2007; Atkins et al., 2004).

A detection of VHE emission from a gamma-ray burst can be used for probing some fundamental physics questions. For example, GRBs may provide one of the best opportunities to detect a possible change in the speed of light at energies close to the Planck scale due to their cosmological distance and rapid variability. This Lorentz-invariance violation is predicted by some quantum gravity models (Abdo et al., 2009; Amelino-Camelia et al., 1998). A VHE detection would be particularly useful since any possible time-delay between photons within an energy band would be much greater at $\sim$1-TeV compared to $\sim$1-GeV. This is especially true of quantum gravity models that predict a lowest-order quadratic dependence of velocity on the energy difference.

Gamma-ray bursts can also be used to probe cosmological models, to the extent that even a mere detection can provide information about star formation rates and their properties in the early universe (Lamb and Reichart, 2000). While more difficult to achieve, GRBs can be used to study cosmology in the context of the ΛCDM model, but a better understanding of their physics is required because they are not uniform enough to serve as standard candles (Liang and Zhang, 2005).

In this chapter, we will cover some of the basic observed properties of GRBs. Later, we will discuss the VERITAS observing program, as well as a model that we have used to interpret the results of our observations. The application of the model to one of the VERITAS GRB observations will be discussed in Chapter 6.

## 2.2 Evidence for two cosmological GRB classes

As high quality information about gamma-ray bursts was collected by the Burst and Transient Experiment (BATSE) (Pačiesas and S., 2004), a couple of properties of GRBs as a group were made evident. Their distribution in the sky was observed to be statistically uniform (Figure 2.2), indicating a cosmological origin and contradicting some early models which assumed a more local origin in order to explain the typically large observed energy fluences (Ruderman, 1975). One other feature that was very clear from early on observations of GRBs is that they were divided into two groups, short ($< 2s$) and long ($> 2s$). This division appears most distinctly when a scatter plot is made of the spectral hardness and the burst duration, as shown in Figure 2.3. Burst duration is often defined as the time during which 90% or 50% of the prompt radiation is received, denoted as $T_{90}$ and $T_{50}$, respectively. The spectral hardness is defined in somewhat

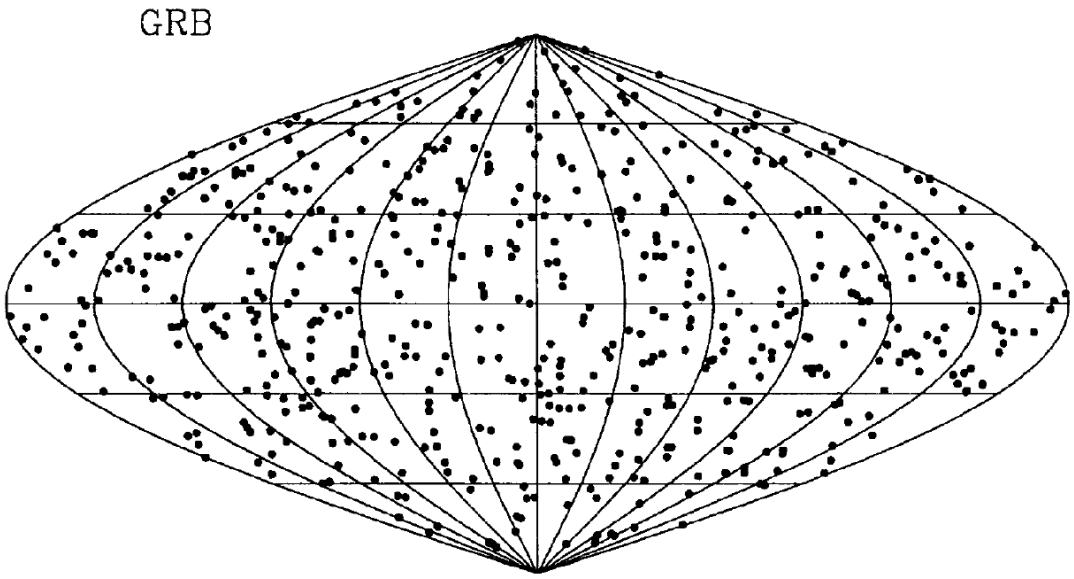


FIGURE 2.2: The cosmological origin of GRBs, from Paczynski (1995). An unbiased sample of 585 BATSE bursts are plotted in galactic coordinates, demonstrating isotropy and indicating that their origin is cosmological.

arbitrary units, and in the case of Figure 2.3 it is related to the sensors on board BATSE. In Kouveliotou et al. (1993), the existence of the two separate groups is found to be statistically significant, and this result has held on to further investigation.

Later studies involving a satellite observing prompt emission and triggering an observation of a corresponding optical afterglow, have given us a redshift distribution, which is somewhat biased by instrument selection effects. Nonetheless, some studies attempting to correct for the bias have concluded that the redshift distribution roughly follows the star formation rate (Coward et al., 2012), but without much confidence at the highest redshifts. In any case, it is very clear that nearby bursts are more likely to be detected, but despite that fact even the *observed* distributions tend to be quite cosmological, with a typical redshift $> 1$.

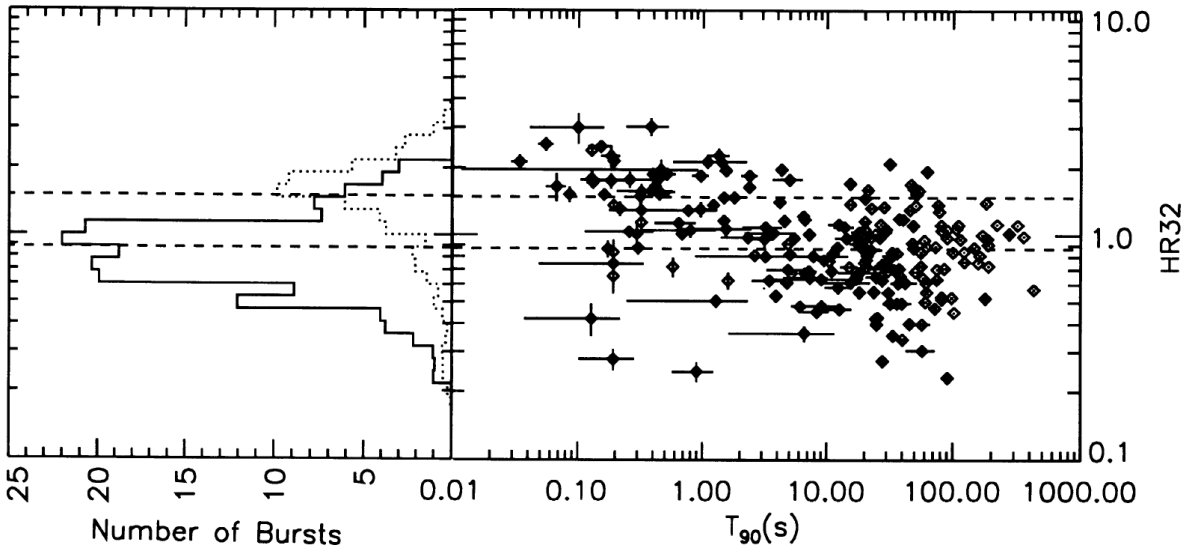


FIGURE 2.3: Observations of two separate GRB classes, from Kouveliotou et al. (1993). **Right:** A scatter plot of $T_{90}$ vs hardness ratio for BATSE bursts. The hardness ratio is (arbitrarily) defined as a relative number of counts observed by different BATSE sensors, the 100-300 keV and 50-100 keV. **Left:** Histogram of hardness ratio, separated into short ($< 2s$, dotted line) and long ($> 2s$, solid line) bursts.

## 2.3 Origin of GRBs

Some long gamma-ray bursts have been associated with a corresponding supernova, for example GRB980425 (Galama et al., 1998) and GRB030329 (Hjorth et al., 2003). However, some nearby gamma-ray bursts triggered a special search for an associated supernova, which was not found, strongly suggesting that at least some long GRBs are of a different origin (for example, Gal-Yam et al. (2006)). This has led to speculation that nearby GRBs may encompass additional processes, but the distant ones are generally supernova related. Still, the exact type of supernova required–and whether it needs to occur in a binary system or a single rapidly rotating star–is unclear (Davies et al., 2007).

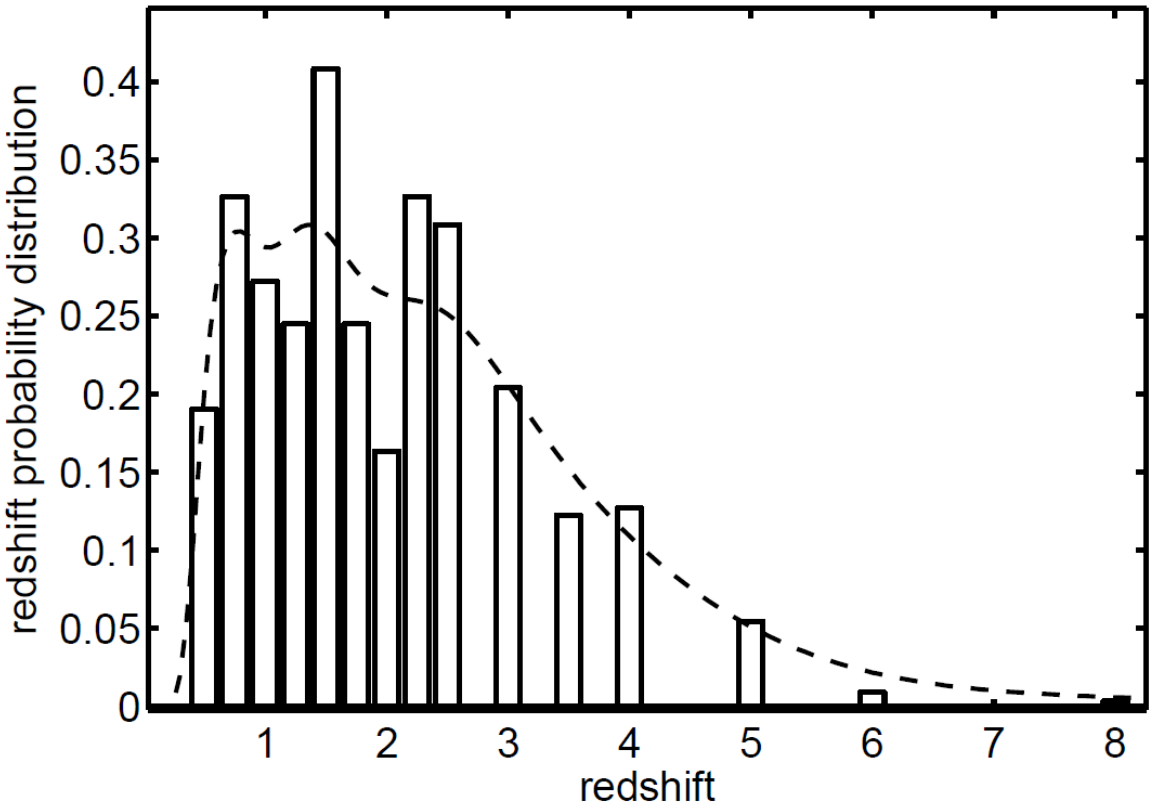


FIGURE 2.4: A sample of 147 redshifts from Swift observations, from (Coward et al., 2012). While this sample is likely biased towards lower redshifts due to selections effects, it still shows a strong majority of detected bursts at $z > 1$.

The origin of short gamma-ray bursts is even more speculative. Mergers of compact objects are considered to be the leading contenders (Nakar, 2007). The merger could involve two neutron stars or a neutron star and a black hole. This belief stems at least partially from the association of some short GRBs with early-type galaxies (e.g. Gehrels et al. (2005)).

In Bromberg et al. (2012), it is argued that the distinction between short and long gamma-ray bursts is too superficial; it also lends strong support to the "collapsar" model of long GRBs. In the collapsar model, long gamma-ray bursts are a result of an imploding core of a dense

star, creating a jet which later has to break through the remaining envelope. The key insight is that the activity time of the core is rather independent of the amount of material the jet has to break through. Therefore, one would expect to find the following features in the distribution of gamma-ray burst durations:

- *For short times, the probability (distribution) should be essentially constant with respect to duration.* Denote the time the jet takes to break though the envelope as $t_b$, and the engine activity time is $t_a$. Both have probability distributions, denoted as $p(t_b)$ and $p(t_a)$: the former is likely not to vary much in general and the latter will vary on timescales corresponding to the typical long burst duration (around 100 seconds). Therefore, $p(t_a) - p(t_b)$ should be fairly constant on few-second timescales. Note that the outcome $p(t_a) - p(t_b) < 0$ corresponds to "failed" bursts, which are likely to be common.

- *Over a longer time scale, the distribution of burst duration when $t_a \gg t_b$ will be essentially dominated by the engine activity time, and show the corresponding features.*

We note that the difficulty of observing a constant probability distribution in early durations is due to contamination by short gamma-ray bursts. In Bromberg et al. (2012), this is handled by examining the duration distribution after applying a filter on spectral hardness, which was clearly observed to be a feature of short gamma-ray bursts. In Figure 2.5, we show a plot demonstrating the probability distribution after such filtering. It serves as convincing evidence for both the collapsar model and the need to reconsider the standard short/long classification (because at least some short-duration bursts are of a collapsar origin).

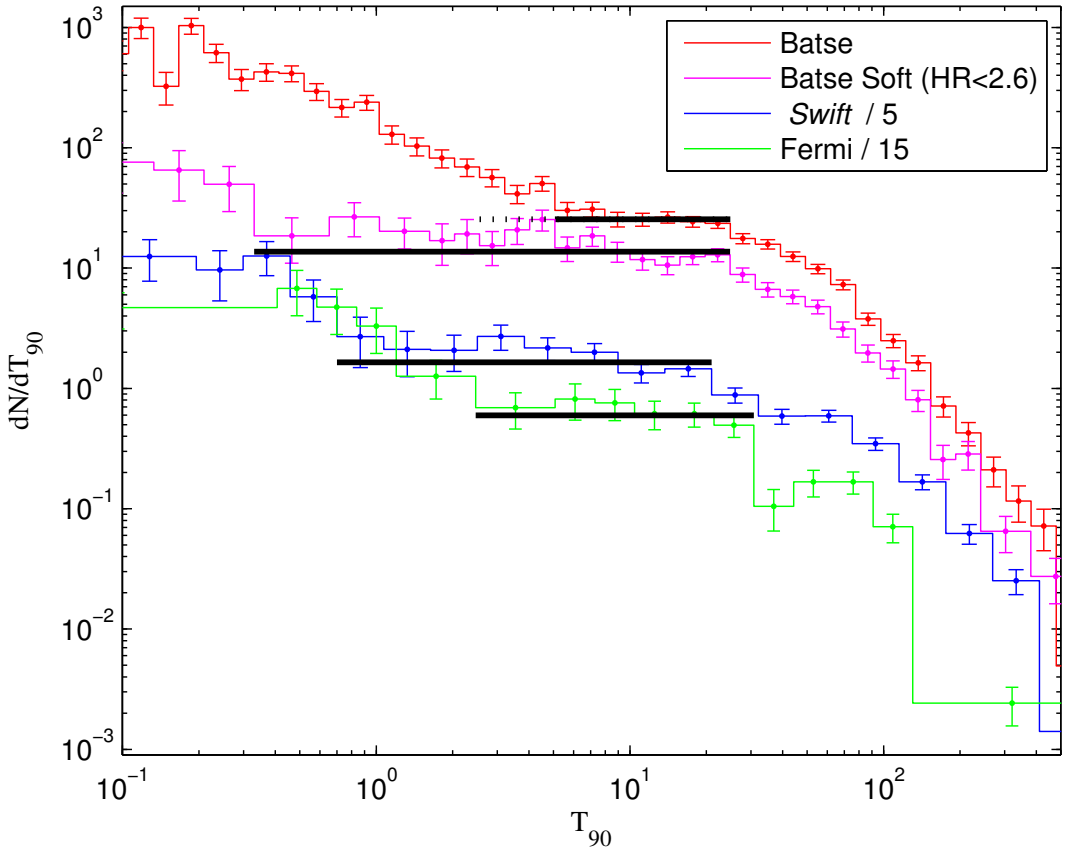


FIGURE 2.5: Distributions of burst durations (as defined by $T_{90}$). The following distributions are plotted without filtering: BATSE (red), Swift (blue), and Fermi GBM (green). In addition, a BATSE distribution with a filter requiring a hardness ratio of less than 2.6, is plotted in magenta. Note that while the distributions are plotted on a log axis, the values themselves are from a probability distribution in linear time (as opposed to the standard way of plotting such distributions). Swift values are divided by 5 and Fermi by 15, for clarity purposes. From Bromberg et al. (2012).

## 2.4 On the VERITAS GRB observing program

When VERITAS receives a burst alert through the GRB Coordinates Network (GCN), the on-site observers are prompted to slew the telescopes to the burst position barring any constraints

such as the position of the Moon or the elevation of the burst. The response time from trigger to observation, which involves arrival time for the alert, response by VERITAS observers and telescope slewing, is usually on the order of a few minutes (Acciari et al., 2011). Previous observations of Swift GRBs by VERITAS placed limits on the possibility of particularly strong VHE emission from those bursts (Acciari et al., 2011).

At the time of this work, VERITAS has observed 159 gamma-ray burst positions, with 50 of those within 180s of satellite trigger time. Simultaneous observations exist for 96 bursts with Swift-BAT, 93 with Fermi-GBM and 12 with Fermi-LAT.

### 2.4.1 Expectations of VHE emission detectable by VERITAS

While the exact nature of the prompt radiation is unknown, and neither the afterglow nor the prompt emission were ever detected in very high energies (more than $\sim$ 100 GeV), there are reasons to be optimistic. The effective area of IACT arrays is very large, being about four to five orders of magnitude greater than satellites, with a manageable background level. Fermi-LAT has detected GeV emission from multiple bursts (Ackermann et al., 2013). In Aliu et al. (2014), the Fermi-LAT emission for a few bright bursts is spectrally extrapolated with no cut-off. This is used to estimate detectability by VERITAS with extremely encouraging results, as shown in Figure 2.6.[1]

IACTs have some obvious limitations in detecting gamma-ray bursts, which are probably responsible to the lack of detection as of yet:

[1]For example, at early times GRB090510 would produce an expected photon rate or about 10 per second, compared to a background rate of about 1 count per minute.

- The cosmological distance of bursts, while not a major impediment for satellite observations,[2] significantly attenuates VHE gamma-rays due to pair production with the extragalactic background light (for example, Gilmore et al. (2009)). One hopes to observe one of the more nearby bursts, which can occur at distances without overwhelming absorption by the extragalactic background light (recall that this absorption is taken into account in Figure 2.6).

- IACTs are not in operation most of the time. The sensitive equipment involved in IACTs is often shut down during rain, lightning, and even moonlight (the shut down is also partly related to usefulness of data taken in such conditions). The Sun needs to go significantly below the horizon before it allows low enough ambient light levels for observation. Cloudy conditions can significantly impede the quality of the data. This leaves only a small fraction of the year as observable, typically around 1100-1400 hours per year.

- IACTs function best when they observe a high elevation source, for reasons that are largely related to atmospheric absorption of Cherenkov light. VERITAS will observe a burst as low as 20 degrees in elevation, but in such cases some aspects of IACT performance are suboptimal.

- An IACT field of view is usually only a few degrees in diameter (typically 3-5°), therefore requiring the telescopes to slew to a source. This slewing time can be substantial, especially when added to the time it takes a GCN alert to get processed and arrive at Earth. In Acciari et al. (2011), it is shown that the time from satellite trigger to initiation of VERITAS observation is typically no more than a few minutes.

[2] Satellite observations are sensitive at much lower photon energies.

- An additional constraint related to the narrow field of view is that some satellites have large uncertainties in their burst positioning, at least initially. When that is larger than the IACT field of view, performance often has to be sacrificed in favor of coverage, resulting in searching patterns for the telescopes. Sometimes, the center of the reconstructed satellite position is used, and one hopes to be fortunate enough to have the burst within the field of view.

One can note that all of the constraints can be mitigated in the case of a fortunate observation. A low-redshift, high-elevation, good weather burst, with an accurate satellite position (and with a reasonable IACT slewing time) is certainly possible. Based on the results in Figure 2.6, a detection of such a source would be highly likely, and a non-detection would be a strong statement of its own. In Chapter 6, we discuss the case of GRB 150323A, a VERITAS-observed burst that came closest to satisfying all of the requirements above, and which was not detected.

## 2.5 Ingredients in a theory of the afterglow

As mentioned in the introduction, there is much ongoing speculation about the central engine and processes that lead to the prompt emission of GRBs. The afterglow, however, is better understood, and involves some basic ingredients that are shared by all plausible central engine theories (Kumar and Zhang, 2015). Experimentally, the afterglow is often seen for days, much longer than the typical time scale of even a long GRB at $\sim$ 100 seconds. It is important to explore this topic further, particularly because IACT observations typically require a telescope slewing time which puts the most plausible observed VHE emission in the afterglow phase. On that note, the Fermi-LAT GRB catalog (Ackermann et al., 2013), which provides the closest

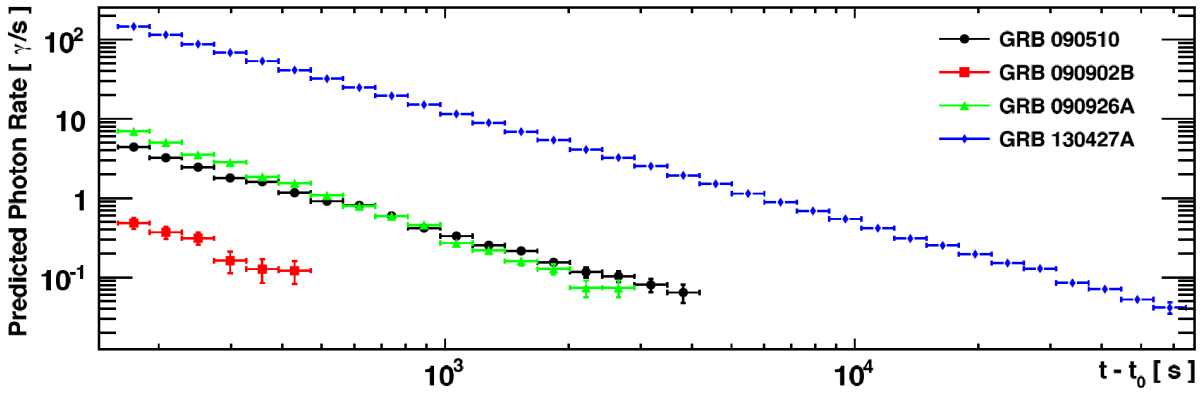


FIGURE 2.6: Predicted VERITAS photon rates form four bright Fermi-LAT bursts. The modelling is based on power-law extrapolation from the Fermi-LAT spectrum, and includes EBL absorption based on the GeV absorption model in Gilmore et al. (2009). A 70 degree elevation at the time of observing is assumed. The VERITAS background rate is on the order of one count per minute. Each bin corresponds to at least three Gaussian standard deviations in expected significance (given the approximately known VERITAS background rate). From Aliu et al. (2014).

observed energy range to IACTs, indicates that most GeV emission is generally seen during the afterglow. One would expect the same to be true at TeV energies.

We will follow the treatment given by Kumar and Zhang (2015), citing articles with more detail when necessary.

### 2.5.1 Blast wave dynamics

After the activity of the central engine, every scenario would lead to a jet and an accompanying blast wave expanding through the circum-burst medium, or CBM (this medium could be a stellar-wind, or the interstellar medium). The large amounts of energy output by the central engine would suggest a relativistically moving blast wave. A solution to the dynamics of the

blast wave was derived in Blandford and McKee (1976) in the context of AGNs. Here we will state only the essential parts of the solution which are required for understanding the afterglow.

We denote the Lorentz factor of the shock front as $\Gamma = \Gamma(R)$, which will generally slow down with increasing radius (R) relative to the center of explosion, as it sweeps the material of the CBM. From the point of view of the shocked fluid, as seen in Figure 2.7, the upstream particles of the CBM are travelling at Lorentz factor $\Gamma$ in its direction. As they collide with the shock front, their direction of motion is randomized, but their kinetic energy is nearly unchanged. The shock also compresses the particle density by a factor of 4. The kinetic energy of an upstream particle of mass $m$ is given by $\Gamma mc^2$. This kinetic energy is then converted into thermal energy, as the directions are randomized. Lorentz transforming back into the lab (progenitor) frame, the mean energy of a downstream particle is $\Gamma^2 mc^2$.

We can now use energy conservation arguments to describe the evolution of the blast wave under simple conditions at a large radius. For example, in the absence of prompt radiation (at a time when it has already passed), we compute in the lab frame the energy of the swept up fluid being the swept up mass times the energy per unit mass ($\Gamma^2 c^2$). This is given by:

$$E_{kin} = \Gamma^2 c^2 \int 4\pi R^2 \rho(R) dR. \tag{2.1}$$

where $\rho(R) \propto R^{-k}$ stands for the density of the CBM. For the case of the interstellar medium (ISM) $k = 0$, and for a stellar wind approximately $k = 2$ (if the mass loss rate of the progenitor was fairly constant in time).

By requiring the energy to be conserved, we find for the ISM case $\Gamma \propto R^{-3/2}$ and for a stellar wind $\Gamma \propto R^{-1/2}$.

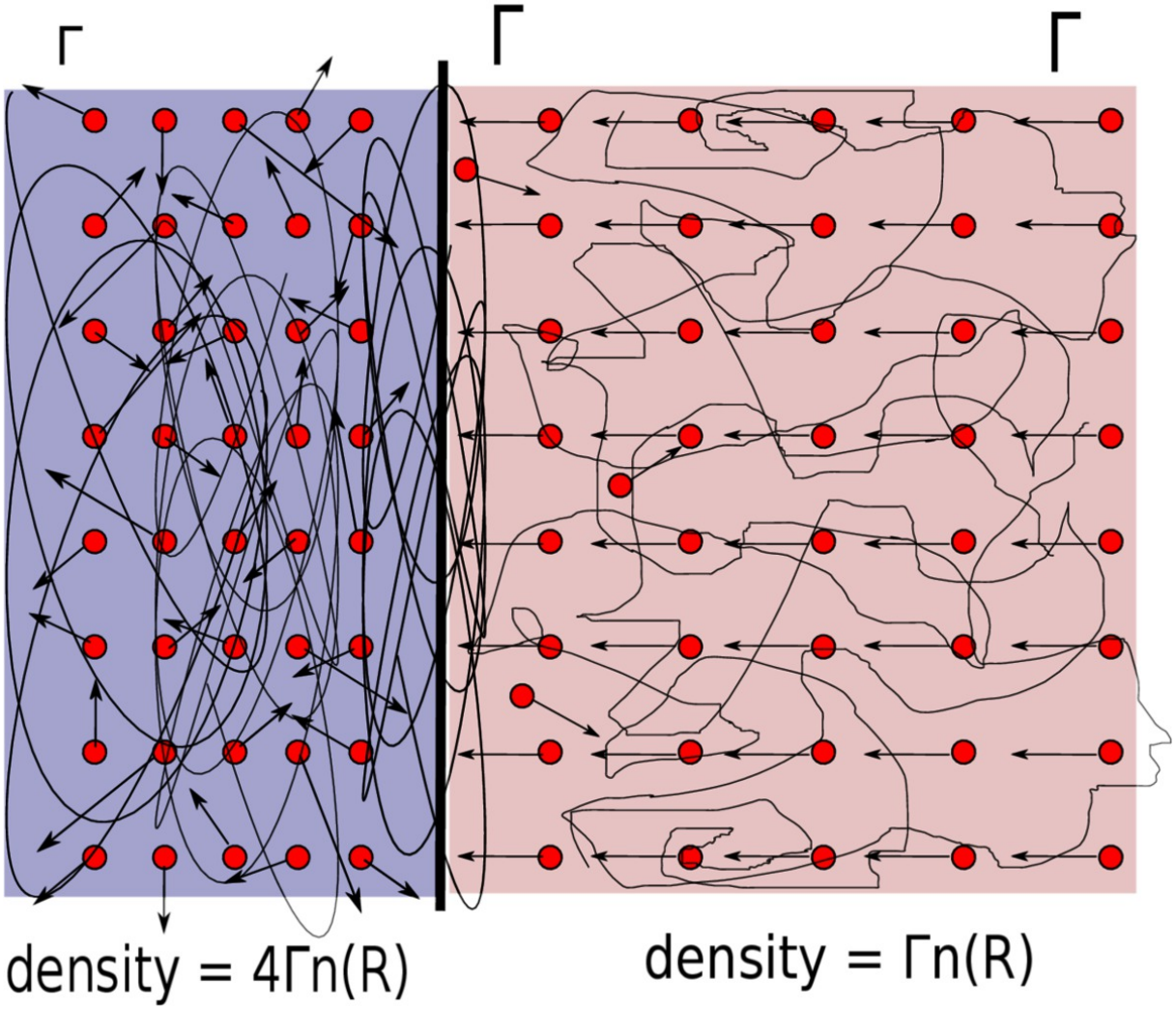


FIGURE 2.7: From the frame of reference of the shock, the upstream particles travel at Γ. The collision randomizes their direction of motion but keeps its magnitude nearly unchanged. The shock also compresses the density by a factor of 4 in the frame of the shocked plasma. From Kumar and Zhang (2015).

We would also like to estimate the evolution of Γ in the frame of the astronomical observer.[3]

The blast wave is moving towards the observer almost at the speed of light, the difference

[3]Here we refer to the time measured by an astronomer on Earth, rather than the time coordinate of a relativistic frame of reference.

being $c - v = c - \sqrt{(c^2 - \frac{c^2}{\Gamma^2})} \approx \frac{c}{2\Gamma^2}$, where the last (Taylor) approximation relies on the ultra-relativistic Lorentz factors expected in the GRB environment.

So $dR \propto \Gamma^2 dt_{obs}$, and for the stellar wind:

$$\begin{aligned} t_{obs} &\propto \int \frac{1}{\Gamma^2} dR \\ &= \int R dR \\ &\propto R^2. \end{aligned} \tag{2.2}$$

Similarly, we find for the ISM: $t_{obs} \propto R^4$.

To summarize, in the case of a stellar wind we found $\Gamma \propto R^{-1/2} \propto t_{obs}^{-1/4}$, and for the ISM $\Gamma \propto R^{-3/2} \propto t_{obs}^{-3/8}$, where $t_{obs}$ corresponds to an astronomer's clock on Earth.

The structure of the blast wave at early times contains a *reverse* shock in addition to the *forward* shock we have already described. In the case of a weak magnetic field of the GRB ejecta, the reverse shock decelerates the ejecta. We show the full structure of the blast wave in Figure 2.8. In the figure, the forward shock is the boundary between regions 1 and 2, and the reverse shock the boundary between regions 3 and 4. For a full derivation of the blast wave dynamics with an arbitrary magnetization, see (Zhang and Kobayashi, 2005). The reverse shock has an identifiable signature in X-ray and radio light curves, which in particular has been found for GRB 130427A[4] (Laskar et al., 2013). Studies show the typical $\Gamma$ of the blast wave at early times is between 100 and 1000 (e.g., Tang et al. (2015)), indeed highly relativistic.

[4]GRB 130427A was a record-setting burst in its fluence, largely due to its proximity (Maselli et al., 2014). It was detected by a large number of instruments, allowing a number of interesting analyses to be conducted.

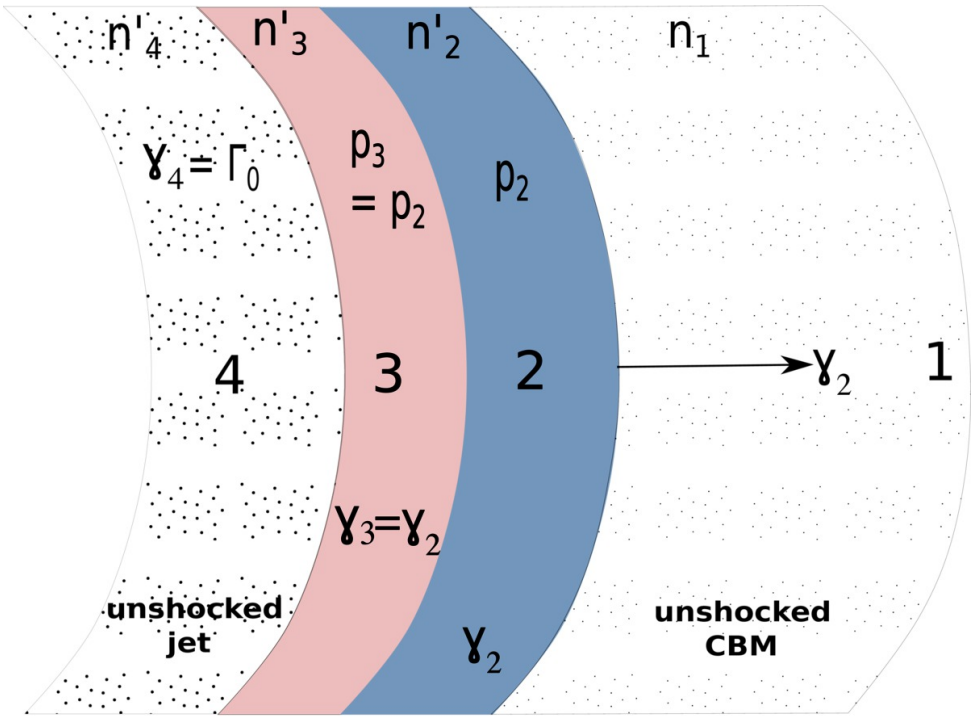


FIGURE 2.8: Structure of the blast wave and jet in an early snapshot (while the reverse shock is still active). **Region 1:** the unshocked CBM yet to be affected by the blast wave. **Region 2:** the shocked CBM affected by the forward shock. **Region 3:** GRB-jet material affected by the reverse shock, with the same Lorentz factor as region 2, but different density. **Region 4:** GRB-jet unaffected by either shock. **Boundary btw. 1&2:** forward shock front. **Boundary btw. 2&3:** surface of density discontinuity. **Boundary btw. 3&4:** reverse shock front. From Kumar and Zhang (2015).

### 2.5.2 Shock-related synchrotron and inverse Compton radiation

The emission coming from the blast wave is believed to be a result of synchrotron and inverse Compton radiation. First, recall that electrons and nuclei in the CBM are thermalized by the forward shock. In addition, electrons in the CBM (and possibly the GRB-ejecta) can be accelerated by the forward and reverse shocks in a first order Fermi process, resulting in a high

energy tail with a power-law distribution (Fermi, 1949; Gieseler and Jones, 2000). Magnetic fields (amplified by the shock) cause the electrons to radiate synchrotron radiation. Inverse Compton (IC) radiation results from upscattering of photons by the electrons in this power-law distribution, or by CBM electrons that were simply thermalized by the shock front. The seed photons for IC radiation can come from the central engine or from the synchrotron radiation of the shocked CBM electrons, which in the latter case is named synchrotron self-Compton (SSC).

In Sari et al. (1998), the synchrotron spectrum of the the electrons is calculated in detail, assuming a high energy electron power law. We will not delve into detail here, primarily because it is unclear whether this high energy component is present in every shock (Sironi and Spitkovsky, 2011), and even when it is, it requires poorly understood parameters. We shift our focus to the thermal population of electrons and its IC emission. As we shall see in the next section, it is a process that can lead to significant VHE emission in the blast wave environment.

## 2.6 Modelling the TeV emission from gamma-ray bursts

### 2.6.1 Overview of the model

VHE emission from gamma-ray bursts has never been detected experimentally in spite of many observations, but upper limits fail to conclusively rule out the possibility of such emission even if comparable in energy to the prompt emission (we will describe the strongest upper limit we are aware of in Chapter 6). The limitations that are likely responsible for the non-detection were outlined in § 2.4.1; we reiterate that those do not correspond to faint intrinsic levels of emission.

In Beloborodov et al. (2014), a model for the very high energy emission from GRB blast waves is described. We believe this model is best suited to assess the VERITAS results which we will present in the coming chapters, for a few reasons. First, the model has been shown to replicate GeV light curves by Fermi-LAT to impressive precision (Hascoët et al., 2015; Vurm et al., 2014). Second, the model does not rely on the uncertain parameters of the high-energy power-law distribution of electrons. Third, the model is able to explain recurring features detected by Fermi-LAT observations in GeV, as we will discuss below.

One of the key insights of the model is the infusion of electron-positron pairs into the CBM by the prompt emission, and its effect on the intensity and spectral properties of both the synchrotron and IC emission. The mechanism for pair creation involves prompt-emission photons that overtake the blast wave, scatter off of the particles of the CBM, and then interact with other prompt photons that were not scattered to produce pairs. While the density of CBM is relatively low, the number of prompt photons is very large and allows for a significant number of pairs to be created for each original electron in the CBM.

Therefore, the large amount of prompt radiation typically associated with a GRB implies a large number of $e^{\pm}$ pairs for every original electron in the CBM. This ratio is termed the pair loading ratio, and denoted by $Z_{\pm}$. To precisely model the number of pairs, one also has to take into account the "avalanche" effect whereby pairs that were already created scatter more photons, leading to a higher rate of pair creation.

Another key aspect is the sharing of kinetic energy between protons and nuclei in the CBM with the surrounding electrons and positrons as they cross the shock front. Simulations show about 30% of the energy is typically given to the leptons as the CBM becomes thermalized (Sironi and Spitkovsky, 2011). This corresponds to a very large boost in the electron and positron thermal

Lorentz factor, comparable to $0.3 \times \frac{m_p}{m_e}$, or several hundred. The ratio is likely even larger, depending on the composition of the CBM and the typical nuclei present. However, when large number of $e^{\pm}$ pairs are present, they also share the energy of the shocked nuclei, which dampens the electron Lorentz factor by about $\frac{1}{Z_{\pm}}$.

Thus the high energy ($\gtrsim 1$ GeV) IC emission will derive from the original electron population as well as the $e^{\pm}$ pairs. As $R$ increases, the prompt radiation density decreases, and the number of pairs declines significantly. This allows a higher Lorentz factor and increases the IC energy. Under typical conditions, peak TeV emission will happen when $Z_{\pm} \approx 1$.

This model goes further and takes into account the pre-acceleration of the CBM by the prompt radiation. Pre-acceleration results in less thermal energy being injected by the shock front, as can be seen by considering the Lorentz factor of the pre-accelerated particles in the shock frame of reference; the thermal Lorentz factor is about $\frac{\Gamma}{\gamma_{pre}}$, where $\gamma_{pre}$ corresponds to the pre-accelerated Lorentz factor of the CBM. During the time of peak TeV emission, the pre-acceleration appears to be a minor consideration in most cases.

Using numerical estimation, the authors are able to use the observational information on the prompt light curve, in addition to the original blast wave energy and CBM density profile, to model the evolution of all parameters of interest.[5] They then predict the GeV and TeV emission expected from the blast wave. In Figure 2.9, we show the example of this analysis for GRB 130427A. The plot shows the evolution of the parameters we discussed against the distance from the center of explosion.

[5]The blast wave energy and CBM density profiles are generally fit to the data. In the case of a VHE detection, they can be fit to Fermi-LAT data (if available) and then tested independently on the VHE data.

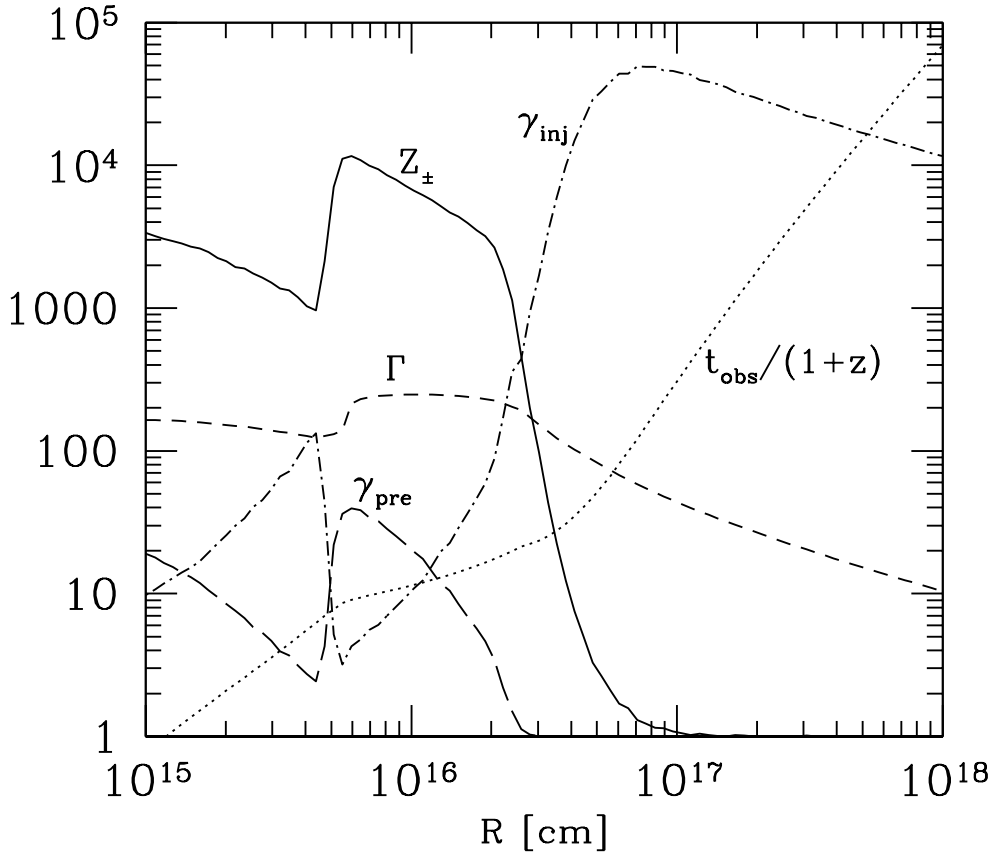


FIGURE 2.9: A plot showing the evolution of parameters discussed in the text with distance from the center of explosion, in the case of GRB 130427A. From Vurm et al. (2014).

There are some parameters in the plot which we did not define in the text so far. $\gamma_{inj}$ stands for the injected Lorentz factor of the CBM electrons and positrons, after considering their share of the kinetic energy of the nuclei. This injected Lorentz factor can be seen to rise most dramatically as $Z_{\pm}$ drops rapidly, indicating the best environment for TeV emission, before the blast

wave further decelerates.[6] The observer time, $t_{obs}$ is also calculated, assuming emission from a typical beamed angle of $\frac{1}{\Gamma}$.

In Figure 2.10, we show the model compares well to the GeV light curve detected by Fermi-LAT. After fitting for both the blast wave energy and wind density of the CBM, optical data is fit with a single additional parameter, the forward shock magnetization–needed for a synchrotron spectrum.

In addition to this fit result and several others (Hascoët et al., 2015), the explanatory power of this model is significant: GeV light curves consistently show a small delay compared to the prompt emission, with the GeV emission coinciding with the prompt phase (Ackermann et al., 2013). The GeV light curve peaks quickly and then decays rather smoothly (unlike the prompt emission). This model explains those features by the change in the pair-loading ratio. A ratio that is too large at very small $R$, coupled with significant pre-acceleration, does not allow the IC spectrum to reach GeV energies at the earliest times. The smooth decline of the light curve can be explained by the arrival times of prompt photons that were IC scattered at different locations, by a relatively smoothly-changing shocked electron-positron population. One can see the rapidly rising, smoothly decaying nature of this model-produced light curve in Figure 2.10.

### 2.6.2 The TeV regime

We will now shift our focus to TeV, in a regime where $Z_{\pm}$ approaches one or so, indicating a low pair loading and sufficient energy per thermal lepton. In addition to its relevance to this

[6] The burst discussed in Figures 2.9 and 2.10, GRB 130427A, has been observed by VERITAS. Observations were late by about 24 hours to the trigger due to a full moon (Aliu et al., 2014), much after this optimal TeV time predicted by this model. No emission was detected.

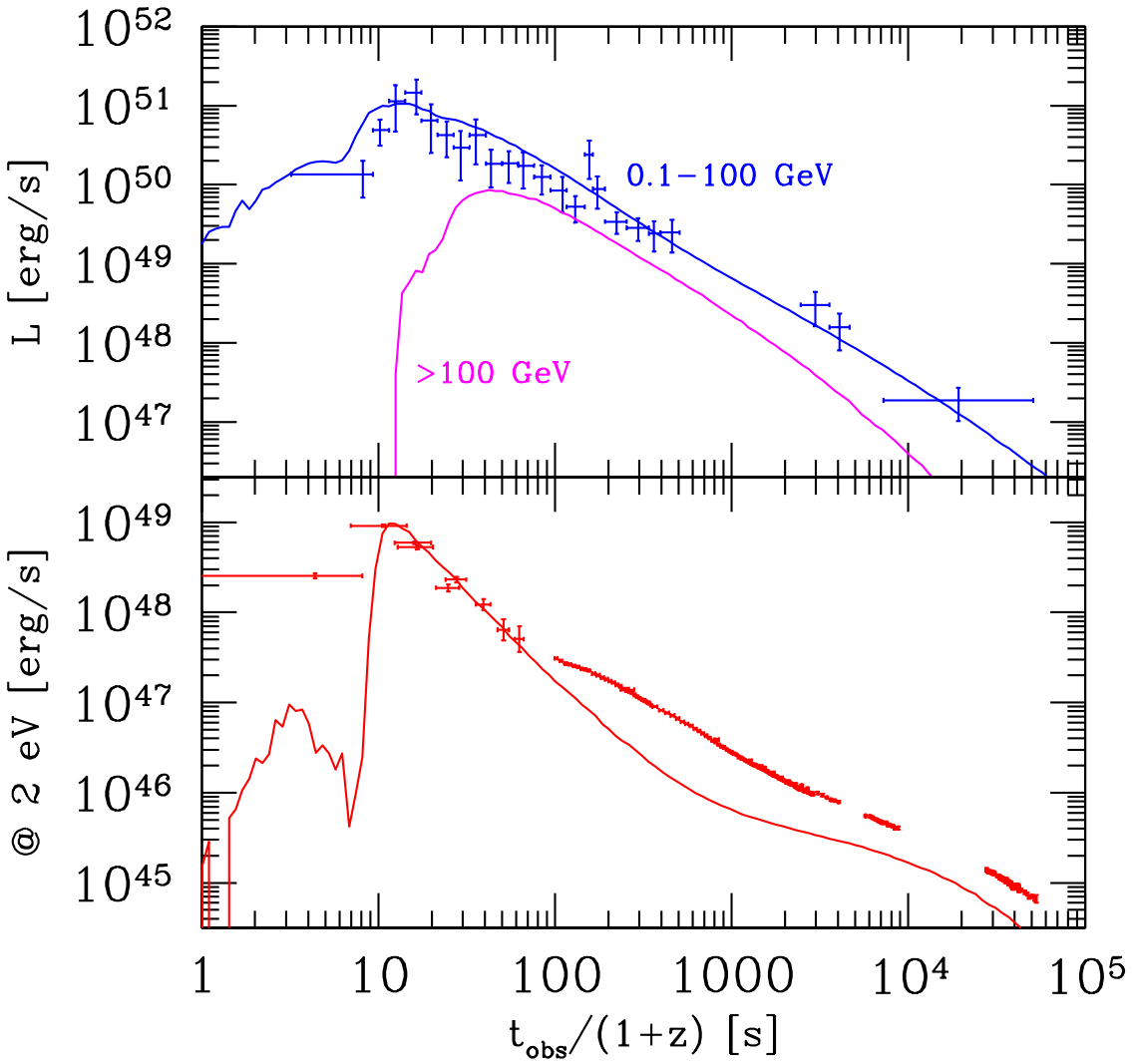


FIGURE 2.10: Model-produced light curves for GRB 130427A, and comparison to optical and gamma-ray data. **Top:** The GeV model is compared to Fermi-LAT data. Comparable TeV energy output is expected with a delay relative to the GeV peak, but no data is available for comparison on the time-scale of the plot. **Bottom**: Optical light curve is compared to data from the optical observatories Gemini-North and Rapid Telescopes for Optical Response (RAPTOR). From Vurm et al. (2014).

work, another reason to consider this environment separately is that the conditions are simpler and do not require much numerical modelling. This regime is described in detail in Vurm and Beloborodov (2016), henceforth referred to as VB2016, and we will follow the same treatment here.

Putting all the factors discussed earlier together, the Lorentz factor of the thermalized leptons in the shocked fluid frame is given by $\gamma_{inj} \approx \frac{\Gamma \mu_e \varepsilon_e m_p}{m_e Z_\pm}$, where $\varepsilon_e$ is the fraction of shared energy ($\approx 0.3$), and $\mu_e$ is the average number of protons in the CBM nuclei.

It can be shown that in the shocked fluid reference frame, electrons need to have a thermal Lorentz factor on the order of 1000 or so to result in TeV emission in the lab frame (Beloborodov et al., 2014). This is not out of the ordinary when $Z_\pm \approx 1$. This in turn implies that the prompt $\sim 1$ MeV radiation upscattering from the electron is in the Klein-Nishina regime of IC scattering (e.g., Weinberg (1995)). We thus are constrained to upscattered energies of VHE photons to more or less $\gamma_{inj} m_e c^2$. We pick up another factor of about $2\Gamma$ in the astronomical observer frame (Earth) due to the ultra-relativistic Doppler factor. So overall we have for observed photon energies:

$$E_{max} \approx \Gamma \gamma_{inj} m_e c^2 \approx \frac{\Gamma^2 c^2 \mu_e \varepsilon_e m_p}{Z_\pm}. \tag{2.3}$$

For the reasonable parameters of $\Gamma = 100$, $Z_\pm = 1$, $\mu_e = 2$, and $\varepsilon_e = 0.3$, we find $E_{max} \approx 5$ TeV–well within the VERITAS energy range.

One parameter we would like to be more precise about is the Lorentz factor ($\Gamma$) at the time when the pair loading ratio approaches one. The radius at which this happens is discussed in Beloborodov (2002), where it is found to be:

$$R_{load} \approx 1.6 \times 10^{16} \sqrt{\frac{E_{GRB}}{10^{53}\ \mathrm{erg}}}\ \mathrm{cm}, \tag{2.4}$$

where $E_{GRB}$ is the energy of the prompt emission. For an exact solution one would need to know the spectral shape of the prompt radiation; the difference this would make is small in the context of this discussion, because TeV emission will still begin but perhaps a bit later or earlier.

For the wind medium, $R_{load}$ is large enough that we can rely on Equation 2.1. We first denote the wind density as $\rho(R) = A/R^2$, where typically for a Wolf-Rayet (WR) star $A \approx 10^{11}$ g/cm. We now compute the Lorentz factor at $R_{load}$:

$$\Gamma_{load} = \frac{E_{kin}}{4\pi c^2 A R_{load}} \tag{2.5}$$

If we use the same parameters as above, in addition to the standard WR density, and $E_{kin} = E_{GRB} = 10^{53}$erg, then: $\Gamma \approx 50$. This still implies the max IC energy is above a TeV, and the majority of the emission thus in the VERITAS energy range (above 100 GeV). If there are enough target photons for IC scattering, efficient IC cooling implies almost all the kinetic energy is emitted in TeV–this condition is satisfied in a reasonable afterglow, as discussed more in detail in VB2016.

In a typical observational scenario, $E_{GRB}$ and $R_{load}$ are known, and the time corresponding to $Z_{\pm} \approx 1$ is more than 100 seconds; therefore an observation in TeV is expected to be on target on time, and to see a significant fraction of the energy $E_{kin}$ in VHE radiation. This will be the case for the VERITAS observation of GRB 150323A, which we will discuss in Chapter 6. If $E_{kin}$ is expected to be large enough to achieve detection, an upper limit is usually given by the

requirement that $E_{max} < 100$ GeV, which will translate into a constraint on $\Gamma_{load}$, and therefore $E_{kin}/A$.

For the ISM, the low CBM density will typically mean that $R_{load}$ is much earlier than the radius of highest luminosity (or energy loss rate by the blast wave), which will be achieved when the thermalized energy given to the CBM is about equal to the initial kinetic energy:

$$R_{ISM} = \left( \frac{3E_{kin}}{4\pi m_p \mu_e n \Gamma^2} \right)^{1/3}, \tag{2.6}$$

where $n$ is the particle density in the ISM, typically about one per cubic centimeter. In this case, $\Gamma$ will almost certainly be large enough to produce TeV emission. In some cases, the X-ray afterglow may not provide sufficient targets for IC emission at this stage, and thus the thermalized electron population will cool adiabatically as it expands. This could mean a small fraction of the kinetic energy will go into VHE emission, and a more careful analysis is warranted.

The TeV emission can suffer from opacity due to pair production which needs to be taken into account. Around the produced TeV gamma-rays there are X-rays originating from the central engine (during the prompt phase), and synchrotron X-rays produced by the thermal lepton population. The former is beamed during the typical radii we associate with TeV emission, and thus provides an "escape" angle, allowing about $\frac{1}{\tau}$ TeV photons to escape, where $\tau$ is a typical optical depth for non-escape angles. A detailed discussion can be found in VB2016.

VB2016 finds that for the ISM the opacity is typically sufficiently low to be negligible, and that for the wind medium the situation is more complex. It is found that most GRBs that are not transparent at $R_{load}$ will become transparent later on while significant TeV emission is still

taking place. However, a very dense CBM, or a very low kinetic energy budget, can prevent TeV transparency altogether.

In conclusion, we find a strong possibility for detectable TeV emission, and discuss the relationship it has to the CBM density and kinetic energy of the ejecta. In the case of an upper limit, a constraint can be derived on those physical parameters and compared to an expected range, either from stellar astrophysics, or Fermi-LAT observations. An ideal scenario for testing our understanding of afterglow physics would be a concurrent detection of GeV and TeV emission by Fermi-LAT and an IACT array.

# Chapter 3

# Detecting and characterizing transient gamma-ray sources: mathematical derivation

## 3.1 Motivation

The standard statistical method for source detection used by IACTs was introduced by Li & Ma in 1983. In their paper the following experiment is assumed (Li and Ma, 1983): an on-source observation is made for time $T_{on}$ and the instrument is later shifted to observe a nearby background region (off-source) for time $T_{off}$. A test statistic is derived using maximum likelihood

theory,[1] given the ratio of observing times $\alpha = \frac{T_{on}}{T_{off}}$ and the number of counts seen during the observations, $N_{on}$ and $N_{off}$.

As IACTs evolved the tools to reconstruct the direction of events, the Li & Ma test statistic was generalized to the "wobble" analysis (Berge et al., 2007), where source (ON) and background (OFF) observations are made at the same time, but reconstructed to different spatial regions. The Ring Background Model (RBM) is one of the standard tools for such analysis and has been successful in part due to its symmetrical nature that tends to cancel out systematic uncertainties in the background rate (Berge et al., 2007).

The Li & Ma likelihood method and its extension to RBM analysis has been the standard approach for analysis of GRB observations by IACT arrays. It uses the fact that the final count tally is Poisson distributed for both the source and background observations regardless of their particular time behaviour during the observation. Time varying sources can thus be inferred using this method, but any prior information on the time behaviour of these sources, as can be provided by other experimental observations or theoretical predictions, cannot be included. In this chapter as well as in Chapter 4, we will show that the inclusion of *a priori* temporal information is an important tool in improving the sensitivity for GRB characterization and detection.

Generalizations of the Li & Ma method have been introduced in the past (for example, Klepser (2012)). They generally address the need to detect extended sources, and may need to rely on instrument response functions (IRFs) such as the point spread function or the energy reconstruction matrix. To the best of our knowledge, no attempt has been made to explore *a priori*

[1] We will assume some familiarity with maximum likelihood estimation, and likelihood ratio tests. The same techniques are used in the Li & Ma paper. See, for example, Pawitan (2013).

knowledge of the source light curve. We believe this can be achieved in a straightforward approach since the time-stamping of events is much more accurate (to $\sim 1\ \mu s$) than the variability of any plausible gamma-ray source.

The purpose of this chapter is to discuss such a method. It is introduced as a natural generalization of the Ring Background Model, and as such it is also resistant to systematic uncertainties and does not require detailed modelling of instrument response functions. Note that because this likelihood method is not binned–or rather, the number of bins approaches infinity, as will be described henceforth–it can capture rapidly varying light curves without the computational complexity and limited resolution of binned methods.[2] It also provides a simplified test statistic for comparison with the Li & Ma method.

The next section begins with a derivation of the Li & Ma test statistic (§ 3.2.1), and then gives a derivation of a simplified form of a time-dependent test statistic (§ 3.2.2). The simplification relies on the assumption that the hadronic background rate is time-independent. In § 3.2.3 we explore methods of dealing with a background rate that is possibly time-dependent. We describe a modification of the Ring Background Model designed for adjusting to varying background rates. We believe this is the most robust approach for GRB detection.

In the next chapter, we will describe results from Monte-Carlo simulations of gamma-ray bursts. We will begin by simplifying the MCs by assuming that the background rate is time-independent. Later, we explore the effect of a time-dependent background on the behaviour

[2]The exploration of an infinite binning of the likelihood method will prove to be interesting mathematically. While one might expect the computational complexity of such a method to go up infinitely, it will in fact yield an elegant result that through some mathematical manipulation will simplify the computational complexity compared even to a simple binned method.

of the test statistic under the null hypothesis. The results will show a strong improvement in sensitivity achieved in a relatively simple way.

## 3.2 Mathematical derivation

### 3.2.1 The Li & Ma likelihood ratio

We will briefly derive the Li & Ma test statistic using average background and signal rates as free parameters instead of counts (as used in the original paper). A more detailed discussion can be found in the original paper (Li and Ma, 1983). Our choice will serve as a smoother transition to the time dependent test statistic.

In the likelihood model, the OFF counts are only due to an unknown background rate whereas the ON counts are explained by an unknown signal rate in addition to the same background rate.

Defining the time-averaged background and signal rates, $\overline{b}$ and $\overline{s}$, in relation to the expected number of counts: $\overline{b}T_{off} =< N_{off} >$, $(\overline{s}+\overline{b})T_{on} =< N_{on} >$, the likelihood is given by:

$$\begin{aligned}\mathscr{L} &= P\left(N_{on}| < N_{on} >\right) P\left(N_{off}| < N_{off} >\right) \\ &= \frac{e^{-(\overline{s}+\overline{b})T_{on}} \left((\overline{s}+\overline{b})T_{on}\right)^{N_{on}}}{N_{on}!} \frac{e^{-\overline{b}T_{off}} \left(\overline{b}T_{off}\right)^{N_{off}}}{N_{off}!},\end{aligned} \tag{3.1}$$

where $P(N| < N >)$ stands for the probability of observing $N$ counts in a Poisson distribution of expected value $< N >$.

To derive the null hypothesis likelihood, we simply set the signal rate to 0. In this case the average background rate is $\overline{b_0}$ which completely accounts for all counts observed:

$\overline{b_0}T_{off} =< N_{off} >; \quad \overline{b_0}T_{on} =< N_{on} >.$

The null hypothesis likelihood is given by:

$$\mathscr{L}_0 = \frac{e^{-\overline{b_0}T_{on}}\left(\overline{b_0}T_{on}\right)^{N_{on}}}{N_{on}!}\frac{e^{-\overline{b_0}T_{off}}\left(\overline{b_0}T_{off}\right)^{N_{off}}}{N_{off}!}. \tag{3.2}$$

We find the maximum likelihood values for the rates by maximizing the likelihood of both the null and signal models: $\overline{b_0} = \frac{N_{on}+N_{off}}{T_{on}+T_{off}}; \quad \overline{b} = \frac{N_{off}}{T_{off}}; \quad \overline{s} = \frac{N_{on}}{T_{on}} - \frac{N_{off}}{T_{off}}.$

The likelihood ratio then simplifies into:

$$\frac{\mathscr{L}_0}{\mathscr{L}} = \left(\frac{\overline{b_0}}{\overline{b}+\overline{s}}\right)^{N_{on}}\left(\frac{\overline{b_0}}{\overline{b}}\right)^{N_{off}}. \tag{3.3}$$

This expression can be compared to equation 14 in Li and Ma (1983). Wilks' theorem (Wilks, 1938) allows us to describe the behaviour of the null likelihood ratio in the regime of high counting statistics. If the null hypothesis is correct, $\sqrt{-2log\frac{\mathscr{L}_0}{\mathscr{L}}}$ is distributed as a Gaussian variable with a standard deviation of 1.

### 3.2.2 Time-dependent signal, time-independent background

To include arrival-time information, as may be advisable for known time-dependent signal, we divide $T_{on}$ into an arbitrarily large number of equal bins N of time $\Delta t$, such that $N\Delta t = T_{on}$. We will require the likelihood model to assign a probability for the number of counts within each bin independently. This will cause the likelihood to approach 0 as $N \to \infty$ because it will factor in the chance that the arrival times fall within specific bins, the number of which approaches infinity. This behaviour will cancel out in the likelihood ratio test, and the resulting test-statistic will converge nicely.

In the limit of large N, each time bin will include either a single event, or no events at all. Each of the time bins is independently Poisson distributed with an expectation value approaching 0 as N increases.

Let $b$ denote the time-independent background rate, and $s(t)$ denote the time-dependent signal rate. The background rate $b$ is treated as an unknown to be optimized by maximum likelihood, and there may be similar unknowns within $s(t)$, such as the amplitude or, a "shape parameter", etc. For use of Wilks' theorem we must require the signal and null likelihood models to be nested, and thus $s(t)$ must have at least one such unknown, most simply the amplitude. If use of Wilks's theorem is not possible, computer modelling can replace it, and the condition above can be relaxed.

We denote the arrival times of signal (ON) counts as $\{t_{on}\} = (t_1, t_2 ... t_{n_{on}})$. The likelihood is a product of the Poisson probabilities for the count tally over all N time bins:

$$\mathscr{L} = \left( \prod_{t_i=(\Delta t, 2\Delta t, \ldots N\Delta t)} \frac{[\Delta t(b+s(t_i))]^{\{0,1\}}}{\{0,1\}!} e^{-\Delta t(b+s(t_i))} \right) \times \frac{(bT_{off})^{N_{off}}}{N_{off}!} e^{-bT_{off}}, \tag{3.4}$$

where $\{0,1\}$ are chosen depending on whether there are 0 or 1 events in the $t_i$ bin.

$$\lim_{N\to\infty} \mathscr{L} = \Delta t^{N_{on}} \left( \prod_{t_i \in \{t_{on}\}} (b+s(t_i)) \right) \frac{(bT_{off})^{N_{off}}}{N_{off}!} e^{-b(T_{on}+T_{off}) - \int_0^{T_{on}} dt s(t)}. \tag{3.5}$$

For the null hypothesis, we set $s(t) = 0$, and denote the background rate as $b_0$, which will obey essentially the same likelihood ratio as the Li & Ma null hypothesis, with only a change of constants.

$$\mathscr{L}_0 = \Delta t^{N_{on}} b_0^{N_{on}} \frac{(b_0 T_{off})^{N_{off}}}{N_{off}!} e^{-b_0(T_{on}+T_{off})}. \tag{3.6}$$

Thus $\mathscr{L}_0$ is also maximized by: $b_0 = \frac{N_{on}+N_{off}}{T_{on}+T_{off}}$, giving

$$\mathscr{L}_0 = \Delta t^{N_{on}} b_0^{N_{on}} \frac{(b_0 T_{off})^{N_{off}}}{N_{off}!} e^{-(N_{on}+N_{off})}. \tag{3.7}$$

The last equality follows from plugging in the exact form of $b_0$ into the exponential. The likelihood ratio is given by

$$\frac{\mathscr{L}_0}{\mathscr{L}} = \frac{b_0^{N_{on}+N_{off}}}{\left(\prod_{t_i\in\{t_{on}\}}(b+s(t_i))\right) b^{N_{off}}} e^{b(T_{on}+T_{off})+\int_0^{T_{on}} dt\, s(t)-(N_{on}+N_{off})}. \tag{3.8}$$

This ratio can be further simplified by exploring the connection between $s(t)$ and $b$. To do so, we must find the maximum of $\mathscr{L}$ or equivalently of $\log\mathscr{L}$. For the purpose of GRB detection we will leave only one free parameter, the amplitude, in the signal time profile, $s(t) \triangleq \theta f(t)$. Where $f(t)$ is a known time profile of the observed burst, typically $1/t$ (Ackermann et al., 2013). This choice reflects the certainty of the flux decaying rapidly (usually as a power-law), and the uncertainty about the amplitude of VHE emission.

We require both partial derivatives of $\log\mathscr{L}$ to vanish at the maximum of the likelihood function:

$$\frac{\partial\log\mathscr{L}}{\partial b} = \frac{N_{off}}{b} + \sum_{t_i\in\{t_{on}\}} \frac{1}{b+\theta f(t_i)} - (T_{on}+T_{off}) = 0, \tag{3.9}$$

$$\frac{\partial\log\mathscr{L}}{\partial \theta} = \sum_{t_i\in\{t_{on}\}} \frac{f(t_i)}{b+\theta f(t_i)} - \int_0^{T_{on}} dt f(t) = 0. \tag{3.10}$$

An important identity is derived by noting that at the maximum of the likelihood function we can assert that $b\frac{\partial \log \mathscr{L}}{\partial b} + \theta \frac{\partial \log \mathscr{L}}{\partial \theta} = 0$.

$$b(T_{on} + T_{off}) + \int_0^{T_{on}} dt\, s(t) = N_{on} + N_{off}. \tag{3.11}$$

The above relation leads to the cancellation of the exponential in the test statistic. It also allows a substitution of $b = \frac{N_{on}+N_{off}-\theta \int_0^{T_{on}} dt f(t)}{T_{on}+T_{off}}$ into Equation 3.10, which results in a polynomial equation of order $N_{on}$ for $\theta$. This problem can be solved using a computer grid search, or any other suitable optimization algorithm to find a maximum likelihood $\theta$.[3] Due to the condition above, any grid search will only need to search over values of the amplitude, $\theta$.

We can now write a simplified form for the test statistic:

$$\frac{\mathscr{L}_0}{\mathscr{L}} = \left( \prod_{t_i \in \{t_{on}\}} \frac{b_0}{b + s(t_i)} \right) \left( \frac{b_0}{b} \right)^{N_{off}}. \tag{3.12}$$

In the case of a time-independent signal rate, this ratio is equivalent to the Li & Ma likelihood ratio, when written in terms of average rates. For variable light curves, ON counts with arrival times that match the expected profile of $f(t)$ receive an essentially higher "weight", according to how bright the source was expected to be at the time.

[3] We have failed to find an analytical solution for $\theta$, but cannot rule out that one may exist. A useful exercise may be to write down the analytical solutions for $N_{on} \leq 2$ and attempt to guess a general form.

### 3.2.3 Time-dependent background

In IACT instruments, a slowly-varying background rate can sometimes be modelled by an *a priori* time behaviour. For example, this can be done by using a known dependence of the background rate on the observation zenith angle. One can also use an independent part of the field of view to study the background variation during an observation. This is the approach we choose here. One should note that when the background variation is weak, which is often the case for IACT observations, the method described in the previous subsection may be sufficient; its tolerance can be studied by simulation, or by computing a source significance for multiple points in the field of view during an observation.

Without loss of generality, consider the case of a Ring Background Model (Berge et al., 2007) type of analysis. $T_{on}$ and $T_{off}$ now refer to different areas of the field of view, and the weighted acceptance represents their ratio. This ratio is termed $\alpha$.

In this context, we will stop referring to the ON and OFF observation times as being different and simply denote them by $T_{obs}$, evolving into the language of the ring background model. Our model will use the area outside of the ring as the background estimation region (see Figure 3.1). In addition, we will define $\beta$ as the ratio between the OFF acceptance and the acceptance of the *a priori* estimation region.

It will be assumed that the acceptance is close to separable in time and radius: $A(r,t) \approx R(r)T(t)$. Since $\beta$ is calculated separately for every run, the approximation needs to be valid only for those shorter time scales. Most of the acceptance changes during a single run are related to changes in the zenith angle, and in turn in atmospheric absorption and projection angles of the shower radiation. Those effects are mostly uniform across the field of view, especially during

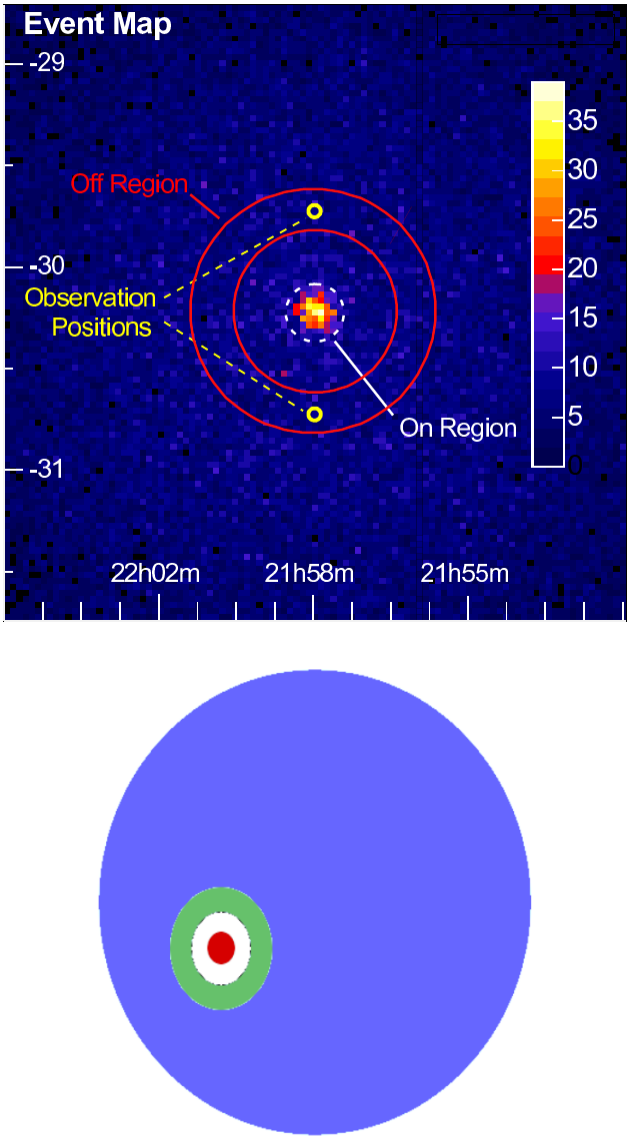


FIGURE 3.1: **Top:** The Ring Background Model (RBM) uses a ring around the source as the background (OFF) region (Figure 4 from Berge et al. (2007)). **Bottom:** Our adaptation of the RBM method uses the area outside of the ring for background variability estimations. The diameter of the FOV is typically about 3.5°.

the limited changes in zenith angle during a single run. If one isn't confident in this assumption a reflected region analysis may be used in place of the ring background.

Our model for the OFF rate is now given by $b\beta B(t)$. $B(t)$ denotes the rate in the *a priori* estimation region, and $b$ is an unconstrained likelihood normalization constant that is defined for two purposes: First, to correct any underestimations or overestimations in $\beta$, and more importantly, to give an indication when those are incorrect. If the acceptance is indeed separable, one would expect b to be close to 1 within statistical fluctuations.

Similarly, the background component of the ON rate is given by $b\alpha\beta B(t)$.

For the signal case, under the assumption that variations in the background rate correspond to variations in the effective area of the instrument, we choose the following model for the rate: $[b\alpha\beta B(t)]\theta f(t)$ (recall that $f(t)$ is given in terms of incoming flux and thus not by itself instrument sensitive.)

By substituting these rates in place of the constant background rates, we can obtain the likelihoods:

$$\begin{aligned}\mathscr{L}_j = \Delta t^{N_{on}+N_{off}} &\left(\prod_{t_i\in\{t_{on}\}} b\alpha\beta B(t_i)(1+\theta f(t_i))\right) \\ &\times \left(\prod_{t_i\in\{t_{off}\}} b\beta B(t_i)\right) e^{-\int_0^{T_{obs}} dt(b\beta B(t)(1+\alpha+\alpha\theta f(t)))},\end{aligned} \tag{3.13}$$

$$\begin{aligned}\mathscr{L}_{0,j} = \Delta t^{N_{on}+N_{off}} &\left(\prod_{t_i\in\{t_{on}\}} b_0\alpha\beta B(t_i)\right) \\ &\times \left(\prod_{t_i\in\{t_{off}\}} b_0\beta B(t_i)\right) e^{-\int_0^{T_{obs}} dt(b_0\beta B(t)(1+\alpha))}.\end{aligned} \tag{3.14}$$

Where j stands for the run index. For more than one run, the likelihood is simply the product over all runs. Recall $\alpha,\beta$, may depend on the run index.

In order to simplify the maximization, we define a new parameter $\theta' \triangleq \theta b$. Clearly, this does not change the likelihood result as $(\theta',b)$ and $(\theta,b)$ span the same space.

The solution follows along the same lines as § 3.2.2. After taking the logarithm and summing over all runs, we arrive at the maximization conditions for the signal hypothesis:

$$0 = \frac{\partial \log \mathscr{L}}{\partial b} = \sum_{All\ Runs}\left(\frac{N_{off}}{b} + \sum_{t_i\in\{t_{on}\}} \frac{1}{b+\theta' f(t_i)} - \int_0^{T_{obs}} dt\,(\beta B(t)(1+\alpha))\right) \tag{3.15}$$

$$0 = \frac{\partial \log \mathscr{L}}{\partial \theta'} = \sum_{All\ Runs}\left(\sum_{t_i\in\{t_{on}\}} \frac{f(t_i)}{b+\theta' f(t_i)} - \int_0^{T_{obs}} dt\,\alpha\beta B(t) f(t)\right). \tag{3.16}$$

A simple notation was used to abstractly note the summation over runs, without explicitly indicating the quantities that depend on the run index.

As in (§ 3.2.2), we extract a condition at the maximum of likelihood function by asserting that $b\frac{\partial \log \mathscr{L}}{\partial b} + \theta \frac{\partial \log \mathscr{L}}{\partial \theta} = 0$.

$$\sum_{All\ Runs} \left(N_{on} + N_{off}\right) = b \sum_{All\ Runs} \left( \int_0^{T_{obs}} dt \left(\beta B(t)(1+\alpha)\right) \right) + \theta' \sum_{All\ Runs} \left( \int_0^{T_{obs}} dt \left(\alpha\beta B(t) f(t)\right) \right). \tag{3.17}$$

This condition is used to turn the 2D computer maximization search into a 1D search.

For the null hypothesis we find

$$0 = \frac{\partial \log \mathscr{L}}{\partial b_0} = \sum_{All\ Runs} \left( \frac{N_{on} + N_{off}}{b_0} - \int_0^{T_{obs}} dt \left(\beta B(t)(1+\alpha)\right) \right). \tag{3.18}$$

Thus,

$$b_0 = \frac{\sum_{All\ Runs} \left(N_{on} + N_{off}\right)}{\sum_{All\ Runs} \left( \int_0^{T_{obs}} dt \beta B(t)(1+\alpha) \right)}. \tag{3.19}$$

One can also note from Equations (3.17) and (3.19), that the exponentials in the likelihood ratio will cancel. Including some other common terms that cancel, we arrive at essentially the same likelihood ratio as in (§ 3.2.2):

$$\frac{\mathscr{L}_0}{\mathscr{L}} = \prod_{All\ Runs} \left( \frac{b_0^{N_{on}}}{\prod_{t_i \in \{t_{on}\}} (b + \theta' f(t_i))} \right) \left( \frac{b_0}{b} \right)^{N_{off}}. \tag{3.20}$$

It is thus instructive to consider the test statistic derived in (§ 3.2.2) in a simplified Monte-Carlo simulation, as will be discussed in the next chapter.

# Chapter 4

# Detecting and characterizing transient gamma-ray sources: implementation and testing in the VERITAS software

## 4.1 The VEGAS analysis package

The challenges of implementing the technique outlined in the previous chapter in the VEGAS code package are numerous. The standard RBM analysis (with the Li & Ma likelihood ratio as its basis) does not require one to keep track of event timing, or even other event statistics for those events that fall outside of the ring (OFF region). This has ended in the the need to restructure the code in a few major VEGAS classes as well as to add a few new ones. We will

give a very brief and essential discussion (omitting much detail) for each new class added to the VEGAS package:

- *VATimedSkyMap:* a sky map that remembers the time of each event. Inherits most of its properties from the previously used *VASkyMap*.

- *VATimedLikelihood:* a significance calculation and parameter estimation class. Can calculate significance with an *a priori* light curve shape as described in the previous sections, as well as the maximum likelihood amplitude of emission and background rate. Does not depend on any VEGAS classes or infrastructure in order to be usable by other experiments or packages if needed. The class in its current state is knowledgeable of power-law and exponential light curves, and can import a light curve from a text file as well.[1] It is easy to add new functional forms due to the function pointer structure that is implemented. This class is designed for maximal efficiency by separating the calculations that rely on the fit parameter ($\theta$) from other cumbersome calculations.

- *VATimeDependentRingBackgroundAnl:* replaces *VARingBackgroundAnl* and puts everything together. The changes required were too large and numerous for inheritance to be desirable. It was thus copied and modified from *VARingBackgroundAnl* and does many things differently. Perhaps the most important (non obvious) difference involves the usage of multiple lookup tables to curb inefficiencies in the original class that could not be maintained due to runtime constraints (more discussion on this below).

The addition of so much new code means it is important to test this technique from both the statistical point of view and the systematic one. We will do both later by looking at Monte Carlo

[1] Thanks to our Nevis summer student Garrett Mathews for his help with the import-from-text implementation.

simulations as well as data. We will look at both in the absence of a signal and in the presence of a signal. In the absence of a signal our expectations will be guided by Wilks' theorem.

Early attempts at running the code were unsuccessful due to the time consuming nature of the calculations. A single VERITAS run would typically take about one day to run on a fairly standard processor (without ability to use multiple cores for a single analysis). In addition the runtime is strongly dependent on the zenith angle of observation due to the way our skymap[2] is binned by default, a feature we did not want to interfere with unless needed. This meant the prospects for an LZA observation analysis–often needed for GRB observations–were difficult and less likely to be used.

In addition to manual optimization of code, we used a tool package developed by Google for performance analysis, aptly named *gperftools*. We were successful in linking this tool to VEGAS. In the final phase of testing, we used *gperftools* and obtained the result shown in Figure 4.1. On the bottom of the figure, it is evident that the majority of the computing time spent being related to trigonometric evaluations. We associate this with calculations of distances between bins in the skymap. The standard RBM code which was in place before our changes was able to handle those calculations by ignoring all bins in the skymap that have no chance of falling within the ring. It was thus structured in an inefficient way.

We have thus added a few lookup tables in order to curb the runtime:

- A table that stores the distance for every bin in the skymap from the center of the map. This table is repeated for every run, due to the wobble technique which forces us to change our position from run to run.

[2]The skymap is a map of the entire field of view of the observation, where excess counts, significance, or any other position-dependent quantity can be plotted.

- A table containing bins that fall within exclusion regions. Those regions are set by the user, usually by choosing a position in the sky, such as a known source position, or a bright star. The user also chooses a radius of exclusion. Bright stars, for example, would require a larger radius.

- The distances between all pairs of bins in the skymap. This was the most memory intensive, and at times required more than a standard laptop could bear. We later simplified this table to include RA symmetry, which made the memory required manageable for almost any laptop. A flag was created to give the user an ability to disable this table if memory demands were too high. This can happen if a user attempts to perform multiple analyses on a single laptop, all at the same time.

Using lookup tables above, in addition to other changes in code efficiency manually and by of *gperftools*, we were able to reduce the runtime of a typical GRB observation to less than an hour.

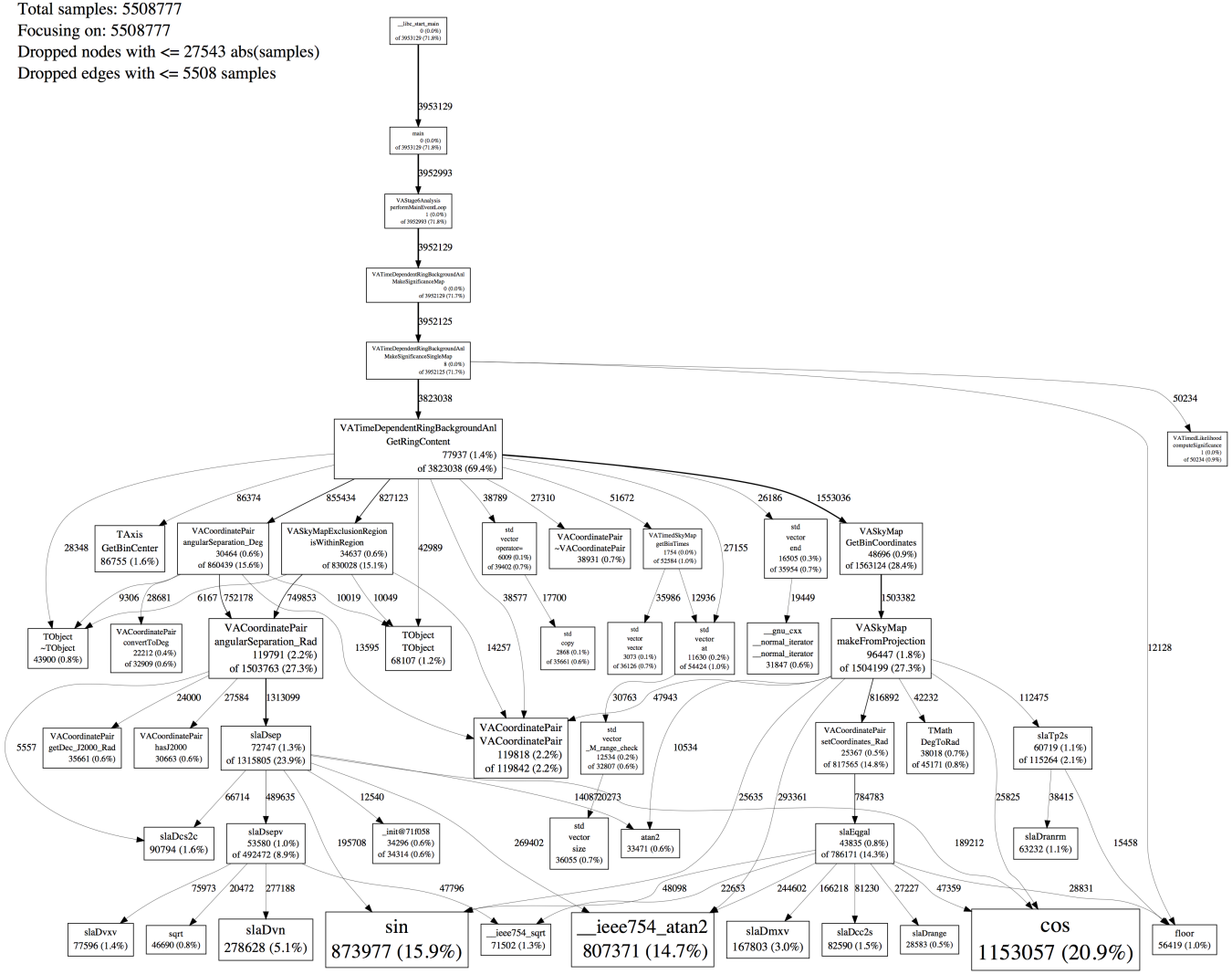


FIGURE 4.1: *gperftools* discovered that the majority of the runtime was associated with trigonometric function evaluation. These trigonometric functions are used to calculate distances between bins in the skymap. We eliminated this problem through heavy usage of lookup tables.

## 4.2 Monte Carlo sensitivity estimations: time-independent background rate

The time dependent test statistic was designed primarily for GRB analysis with IACT arrays. Keeping that in mind, a simple Monte Carlo simulation was written in Python to assess the improvement in sensitivity expected for a typical GRB analysis.

We first consider a time-independent background scenario as described in (§ 3.2.2) for the simplicity of the model, and the expectation that the improvement in sensitivity should be similar for other background models (e.g. § 3.2.3).

A GRB signal was simulated on top of a time-independent background. The light curve was assumed to decay as $1/t$ (Ackermann et al., 2013), and the observation onset (in relation to $t = 0$) and amplitude of this GRB signal were given a changeable value, of which some particular values were studied. Each MC instance generated a random list of ON and OFF arrival times which were fed into an optimization routine following (§ 3.2.2) and the resulting significance was obtained. A significance value was also obtained using equation 17 of Li & Ma (Li and Ma, 1983). Thirty thousand of these MC runs were generated and histograms of the significance were produced. A selection of such histograms can be seen in Figure 4.2 (using parameters more or less matching current generation IACT arrays – VERITAS, H.E.S.S., MAGIC).

It should be noted that for a rapidly decaying signal, the Li & Ma test statistic reaches a maximum significance after some time and then slowly decays, while the time-dependent likelihood plateaus after a longer duration. Thus a more illustrative plot must involve the observing duration. This is shown in Figure 4.3. While one can attempt to optimize a time-window for the Li

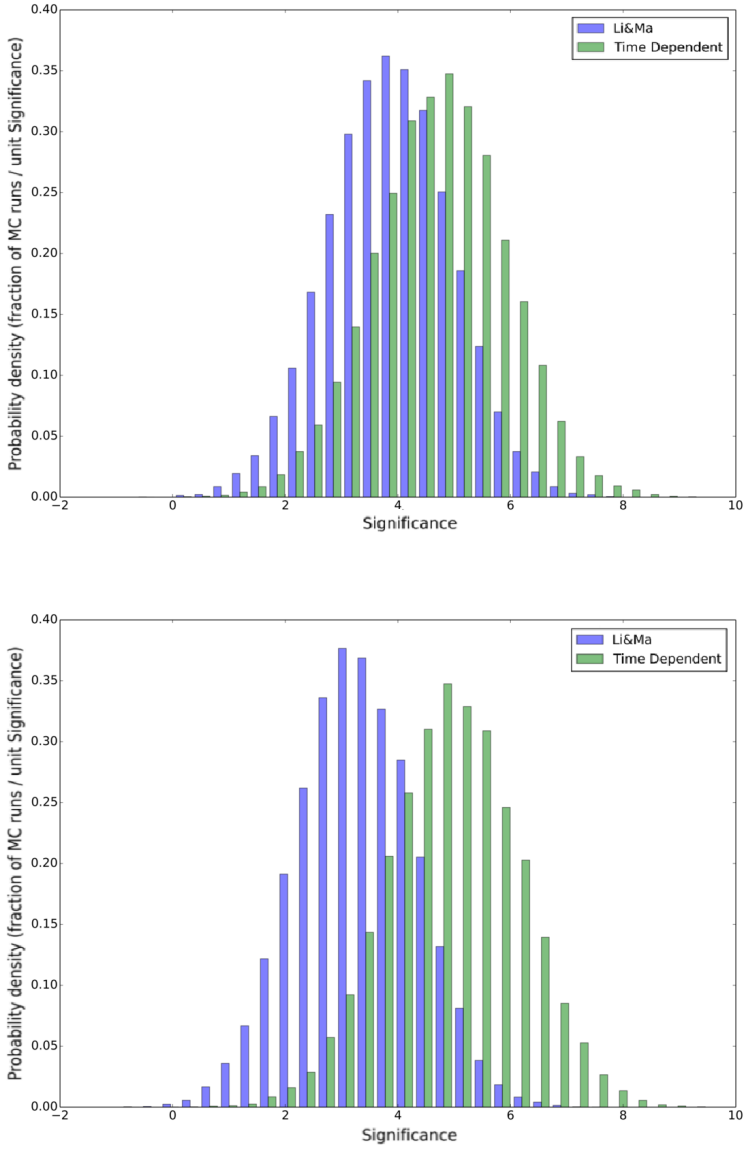


FIGURE 4.2: A comparison between the significance obtained by the time-dependent method and Li & Ma, for a simulated gamma-ray burst. The background rates were more or less adjusted to those typical for a current generation IACT array. The intensity of the burst was chosen to be close to the detection threshold. **Top:** The signal intensity of the GRB was given a power-law decay index of -1 ($f(t) = 1/t$), and the observing delay chosen as 2 minutes, with a total observing duration of 30 minutes. **Bottom:** The total observing duration was extended to 90 minutes.

& Ma likelihood test, it will depend on the unknown amplitude of emission, and thus can only be approximated prior to analysis.

Thus our results show a gain of roughly 25% in significance, if one generously assumes that the Li & Ma time integration can be decided *a priori*. The results shown will vary when one adjusts the delay time of the GRB observations as well as the assumed time decay. A shorter time delay, as well as a faster time decay will translate into greater gains for this new test statistic compared to the Li & Ma test statistic.

### 4.2.1 Can the Li & Ma integration time be decided *a priori*?

We've previously made the claim that the Li & Ma likelihood test integration time cannot be decided without knowing the amplitude of VHE emission *a priori*. While this may appear obvious to some, a plot demonstrating the magnitude of the effect for a typical GRB light curve may prove useful. In Figure 4.4, we plot the time-dependence for the significance for a "weak" burst observation as well as a "strong" one, to show that the maximum significance is obtained after a longer duration for a stronger burst. This plot also demonstrates an additional advantage of the time-dependent likelihood method is that more integration time will likely always be better, without the need to know the amplitude of VHE emission *a priori*.

## 4.3 Tests on observational data

To ensure the reliability of the VEGAS code and basic compatibility with the expectations found from Monte Carlo simulations, we used a variety of data observations. For example, dark matter

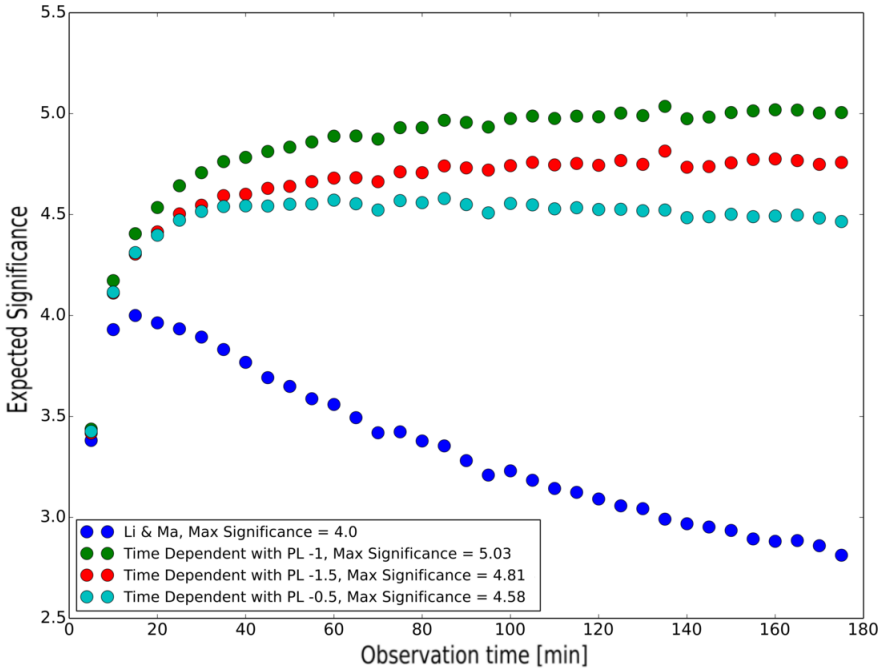


FIGURE 4.3: A plot studying the change in the significance value with observing duration. Each point represents the mean of a histogram as in Figure 4.2 with a few thousand simulated observations. The power-law index for the source time decay was chosen as -1.0 ($f(t) = 1/t$), and was reconstructed with the *a priori* indices of -0.5, -1.0, and -1.5 to assess the impact of the uncertainty of this value in an experimental setting. The Li & Ma significance starts dropping in value after about 30 minutes, while the time-dependent model continues to improve and, only later, to plateau.

searches provide us with runs where a very strict upper limit was reached in a failed attempt to discover VHE dark matter signatures. One such example is the Draco dwarf spheroidal galaxy Acciari et al. (2010). The many dark matter runs can thus be used as a first-order approximation of a VHE dark field of view. We have used these runs to test the implemented VEGAS method on a dark field, and have also injected a simulated time-dependent signal into the ON region to test the performance for source detection. In this section, we will discuss such tests and others.

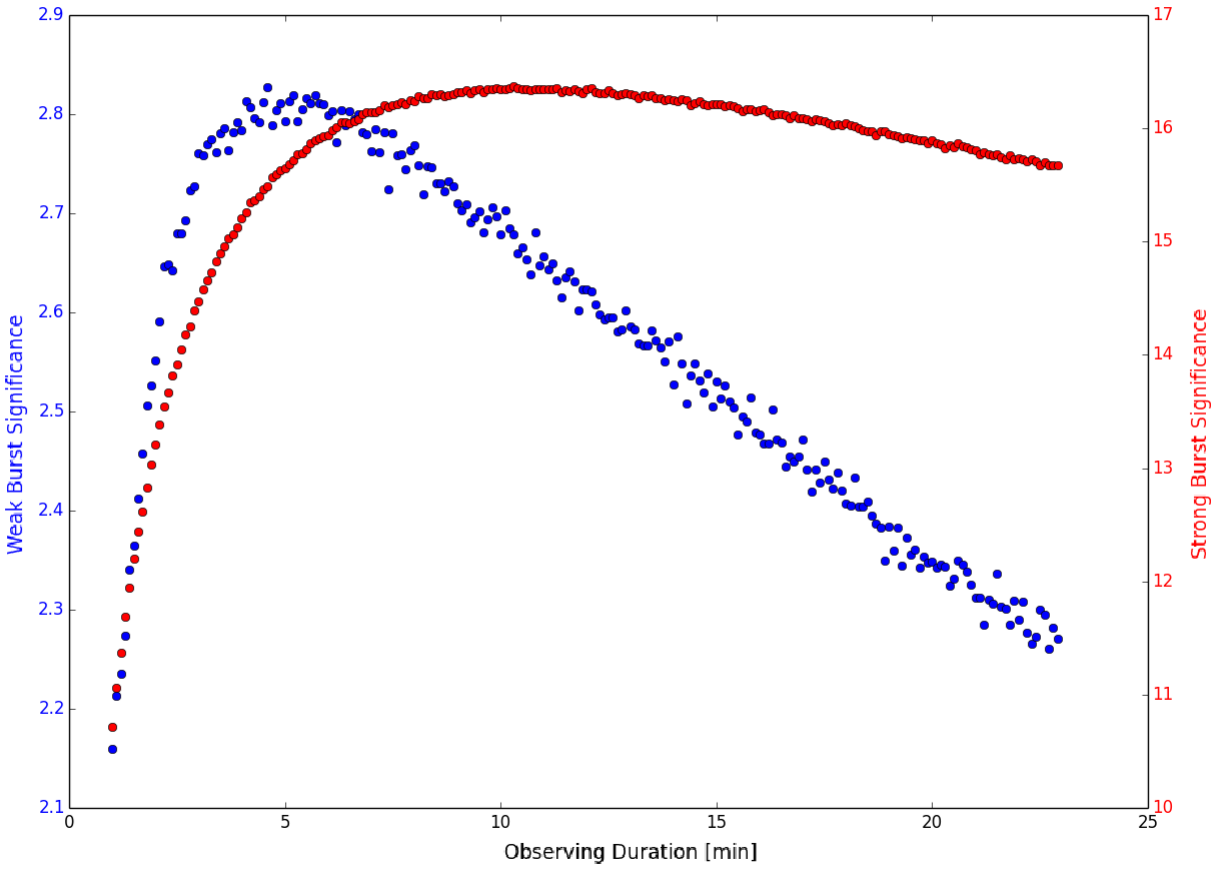


FIGURE 4.4: The ideal integration time of a burst with the Li & Ma method depends on its unknown amplitude. We simulate burst observations for a weak and a strong burst to demonstrate the magnitude of the effect. The bursts are simulated with a power-law index of $-1$, and an observing delay time of about 1.5 minutes. It appears that it should be possible to choose an integration time, without sacrificing more than 5-10% in sensitivity, even for a wide range of possible VHE emission amplitudes.

### 4.3.1 BL Lac flare

On June 28th, 2011, VERITAS detected a strong flare from BL Lacertae. The observation lasted 34.6 minutes, and the average flux was found to be around 125% of the Crab Nebula

flux (Arlen et al., 2013). The rapid nature of the flare made it a prime candidate for testing of the time-dependent likelihood on a detected signal. The flux appeared to be exponentially decaying, and when fit with such a function, was found to have a decay-time of $13 \pm 4$ minutes.

We modelled this time-decaying signal by Monte Carlo simulation, and compared those results (improvement in sensitivity) to data. We first modelled an exponentially decaying signal using the simulations described in the previous subsection. We produced a plot predicting the evolution of the expected significance over time (compare to Figure 4.3), as well as a significance distribution corresponding to a statistical ensemble of such an observation (compare to Figure 4.2). These results can be seen in Figure 4.5. We predicted an improvement from a significance of about 22 sigma, to one that is nearly at 25 sigma.

An analysis of the BL Lac data confirms this result. We've followed the same cuts and analysis routines described in Arlen et al. (2013), with the exception that we've replaced the Li & Ma test statistic with the time-dependent one. We've also modified the decay-time of the signal to include other possibilities, to test for the sensitivity to this parameter. We tested decay time of 5, 9, 13, 17, and 21 minutes (Figure 4.6). We've also tested for an infinite decay-time, corresponding to a flat light curve, which should replicate the Li & Ma significance. The results we found confirmed our expectations, with roughly a 10% improvement in significance for a 13 minute decay time, which smoothly declines into the Li & Ma significance as the time-decay is varied. The test at infinite decay time produced a result equal to Li & Ma to the 4th significant digit–a good test on possible systematic or code related effects. The slight difference between the two may be related to a slightly different way in which an acceptance curve is produced for the time-dependent likelihood.

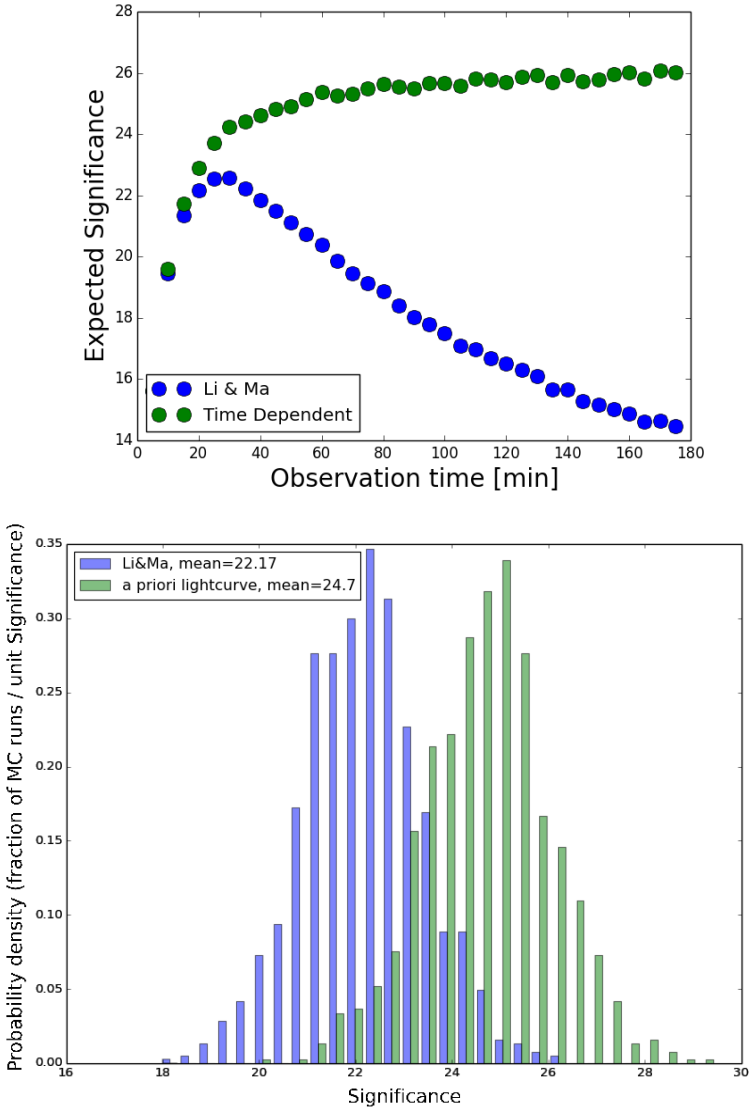


FIGURE 4.5: Using Monte Carlo simulations to predict the improvement in significance for the BL Lac flare. **Top:** Monte Carlo time evolution of significance for a source decaying exponentially with a decay-time of 13 minutes. A pattern similar to the one seen in Figure 4.3 emerges: the Li & Ma significance declines after about 30 minutes while the time-dependent significance continues to improve and only later plateaus. By a fortunate coincidence, the VERITAS observing time for this flare, around 35 minutes, is close to the optimal Li & Ma integration time. **Bottom:** Focusing on the observing time of this particular flare, we model the ensemble of possible observations. An improvement of about 10%, or 2 sigma is expected, with possible variations due to background and signal fluctuations (a precise calculation predicts an *expected* improvement of 11.4%).

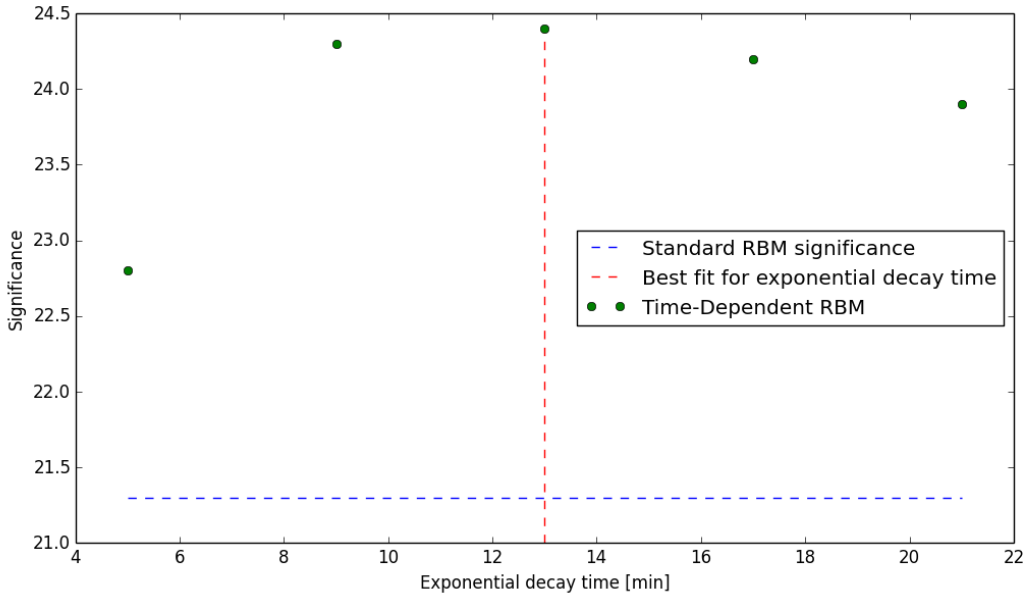


FIGURE 4.6: The significance achieved for the BL Lac flare with the time-dependent likelihood for different *a priori* decay-times.

### 4.3.2 Injecting a simulated signal into data runs

One of the first and obvious tests one can conduct is to inject a simulated time-dependent signal into a data run and then analyze it. We've developed the infrastructure to do this in Python using PyROOT.[3] Our PyROOT script is responsible for going into the data file produced by the fifth stage of VEGAS, and to add counts with a desired temporal probability distribution. One later runs a VEGAS sixth-stage analysis on the modified fifth-stage file. We've applied this PyROOT script to a group of 3 consecutively-observed Draco runs (thus with two wobble changes in between). Due a small excess of counts in the ON region (likely due to a statistical

[3]PyROOT is an implementation of the ROOT libraries in the Python programming language, which allows one to combine the many libraries available in Python with ROOT's ability to interact with VEGAS files. As one example of the usability of this interaction, we have used Python tools to randomly sample from various probability distributions, as described later in the text.

fluctuation), we've adjusted the script to delete all existing ON counts and then add a temporally uniformly-distributed background such that there are no excess counts.[4] Later, the script injects a simulated signal with a specified time behavior.

The light curve we chose for the simulated signal is $1/t^{1.5}$, with an origin time corresponding to 5 minutes prior to the first Draco run. In Figure 4.7, we show a distribution of significances observed by repetitively running the same PyROOT script on the fifth stage VEGAS file and consequently running the sixth stage in each repetition. The distribution in Figure 4.7 can be compared to Figures 4.2 and 4.5 (bottom), but with less observations simulated due to computational constraints. The means of the distributions are in line with what is found by the simpler simulations in Figures 4.2 and 4.5, with an improvement in the mean significance of 36%.[5]

### 4.3.3 Testing for nice behaviour of the null distribution

We chose three 30-minute runs from a Draco observation and searched for a GRB signal with a time delay of 5 minutes and that decays as $1/t^{1.5}$. This test was conducted in the absence of an injected signal, and the expectation is that the distribution of significance will approximately be Gaussian with unit standard deviation, following Wilks' theorem.

Since the coupling of runs at different wobble positions introduces some technical difficulties, we began by testing only the first Draco run out of the three. This way, possible features of the code that "stitches" together different wobble runs can be tested and found independently.

[4] Note that simply removing even a single excess count would bias the time-dependent distribution of the background.

[5] For the same 20 simulated observations, we've also attempted to look for a burst with a power-law index of -1 and -2; they've shown an improvement of 33% and 34% in significance, respectively.

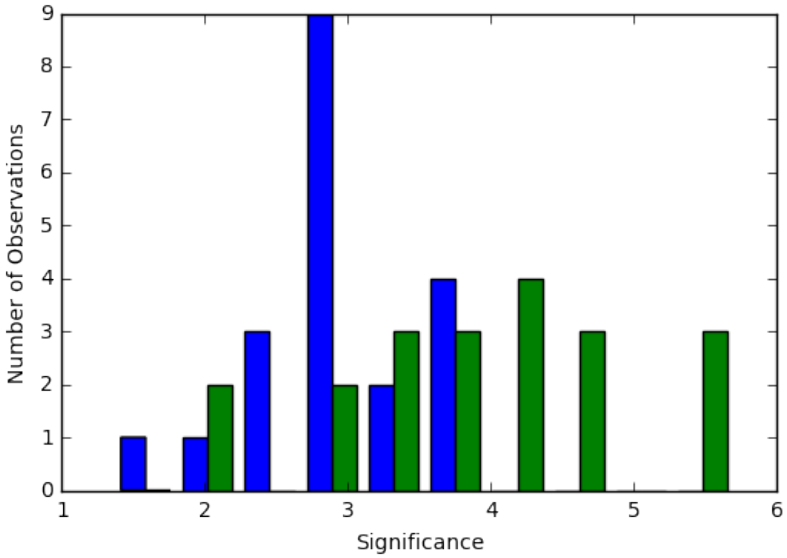


FIGURE 4.7: A simulated time-dependent signal was injected into three consecutive runs aimed at the Draco dwarf galaxy (as described in text). An analysis with the Li & Ma method as well as the time-dependent method has shown an improvement in the mean significance of about 36%. This is in line with simpler and independent Monte-Carlo simulations produced in Python, and serves as evidence for the successful implementation of our method in VEGAS with minimal or no systematic effects. The Li & Ma significance histogram is plotted in blue, and the time-dependent in green.

The skymap of point significances across the field of view, and their distribution, can be found in Figure 4.8. While the significance distribution appears close to Gaussian and has an RMS of 0.97, there is some clear non-Gaussian behavior at the tails. This behaviour is characterized by an apparent deficit in both tails (compared to a Gaussian), but mostly on the negative significance end.[6] In § 4.4 we will be able to explain this behaviour at the tails using simulation: It is a result of low-counting statistics, whereas Wilks' theorem is applicable in the limit of a large sample size. Using Monte-Carlo simulations, we will show this approach to Gaussianity by gradually increasing the background rates.

[6]Some clarification may be needed for what is the meaning of a negative significance: Recall, the likelihood ratio test can only ascribe a positive significance to an observation; a negative sign is customarily attached to the significance in cases where the best-fit amplitude is negative (a gamma-ray "sink").

In both data and simulation, we found this behaviour to consistently show a deficit of significance at the tails, when compared to a Gaussian. This corresponds to low "false alarm" rate, and may therefore increase the sensitivity of the time-dependent technique, compared to the case where one assumes perfect Gaussian behaviour. However, we have no proof that this behaviour is the case in general. We recommend that experiments in a low background regime rely on Monte-Carlo simulations rather than Wilks' theorem to assign significance to an observation (although the corrections we observed to source detection are relatively minor).

We went on to test the code we added to VEGAS in its ability to "stitch" together different wobble runs. We used all three Draco runs, and while the first few tests indicated some unexpected features, we were able to correct them. One example of a problem which was fixed at this stage relates to the way *VATimeDependentRingBackgroundAnl* handles parts of the skymap which were in the field of view only during specific runs. For some bin/run combinations, the ON exposure (or "time") is 0 and the OFF exposure may be finite but small; this was not anticipated in the code originally and had to be handled with care (by disabling runs with too little exposure for every bin). We plot the distribution obtained for three consecutive Draco runs in Figure 4.9, after our corrections to VEGAS code. It has an RMS of 1.004, and (unsurprisingly) appears to have the same deficit at negative significance that was found for a single Draco run.

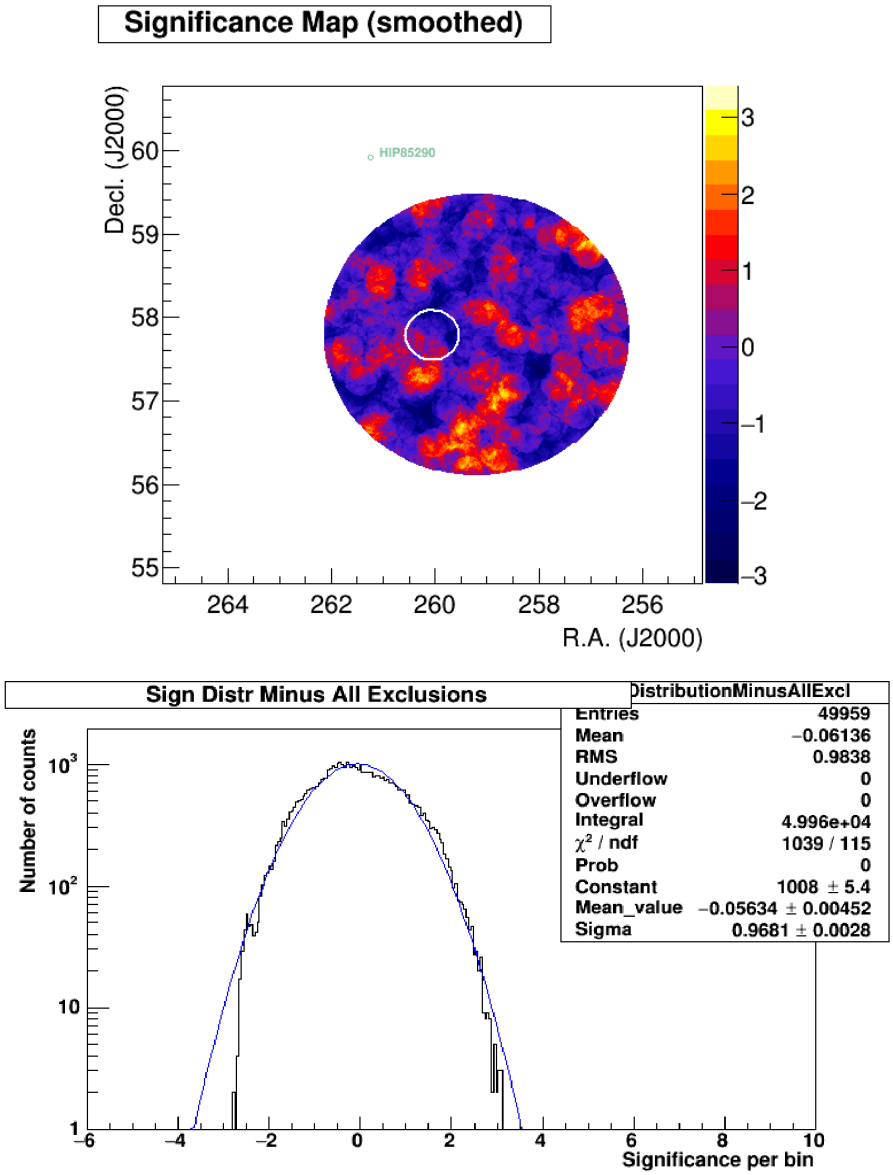


FIGURE 4.8: We attempt to search for a (non-existent) GRB signal in a Draco run. The parameters for the time-dependent search are a delay time of 5 minutes and a power-law decay index of -1.5. **Top:** A skymap with the significance calculated for every point in the FOV (with a standard radius for each point, corresponding approximately to the VERITAS point spread function). The white circle denotes the area around the Draco Dwarf galaxy. **Bottom:** In black, the distribution of significances for all points in the field of view that are not excluded from the analysis, such as areas in the vicinity of bright stars. In blue, a Gaussian distribution with the best-fit width and mean is plotted. The black distribution is nicely Gaussian around the center with an RMS close to 1, but the Gaussian form breaks down near the tails.

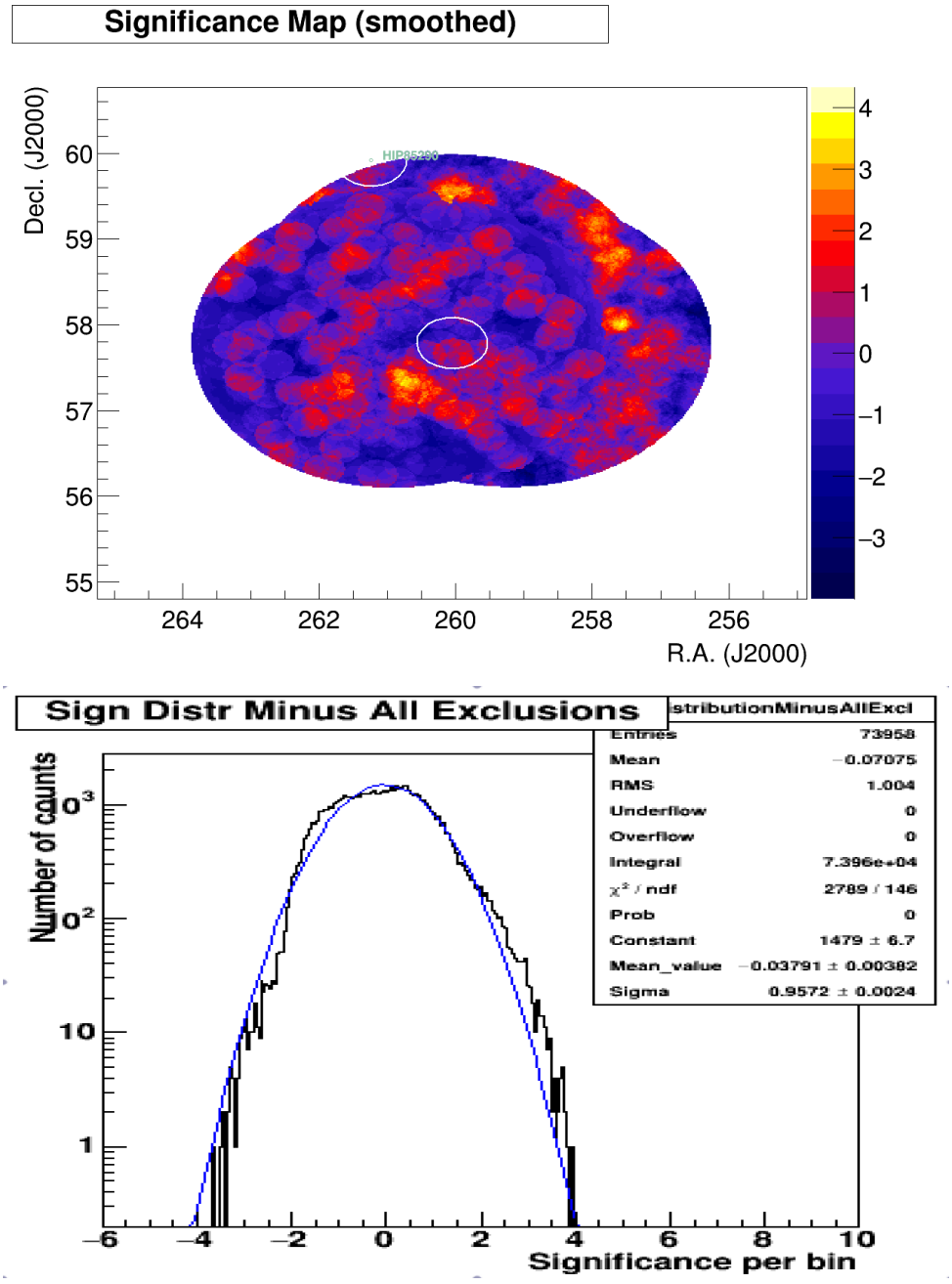


FIGURE 4.9: The significance map and distribution plotted for multiple Draco runs, as a test for the ability of the code to properly "stitch" different wobble runs together.

## 4.4 Converging into Wilks' theorem: approach of the test statistic to Gaussian behaviour

As we noted in Subsection 4.3.3, analysis of Draco runs has indicated non-Gaussian behaviour of the null distribution around the tails. Here we will show results that confirm this behavior in simulation. We will also show that in the correct asymptotic limit, the null distribution approaches that of Wilks' theorem.

Wilks' theorem is correct in the limit of a large sample, which in our case corresponds to a large background rate.[7] In Figure 4.10, we increase the background rate in our simulation gradually, from 10% of the typical VERITAS soft-cut rate, to 1000%. Realistically, the former scenario may roughly correspond to VERITAS hard-cut rates, and the latter to future CTA[8] rates.

What we find is a striking similarity to the experimental distribution in Draco (center plot in Figure 4.10), and a smooth transition into Gaussian behavior. Thus, it appears that current generation IACTs do not have sufficient counting statistics to fully approximate Wilks' theorem, but CTA might. We note again what appears to be a lack of events in the tails, which corresponds to a low "false alarm" rate; if carefully simulated and used, it will in fact boost the sensitivity gains of the time-dependent method.

[7] While a large sample is usually taken to mean multiple observations, it is not too difficult to show that this is mathematically equivalent to a higher background rate in a single observation.

[8] The Cherenkov Telescope Array (CTA) is the next generation IACT array, with about 10 times as many telescopes and 10 times the sensitivity of current-generation arrays (Actis et al., 2011). The number of telescopes roughly corresponds to the amount of background for a given set of cuts.

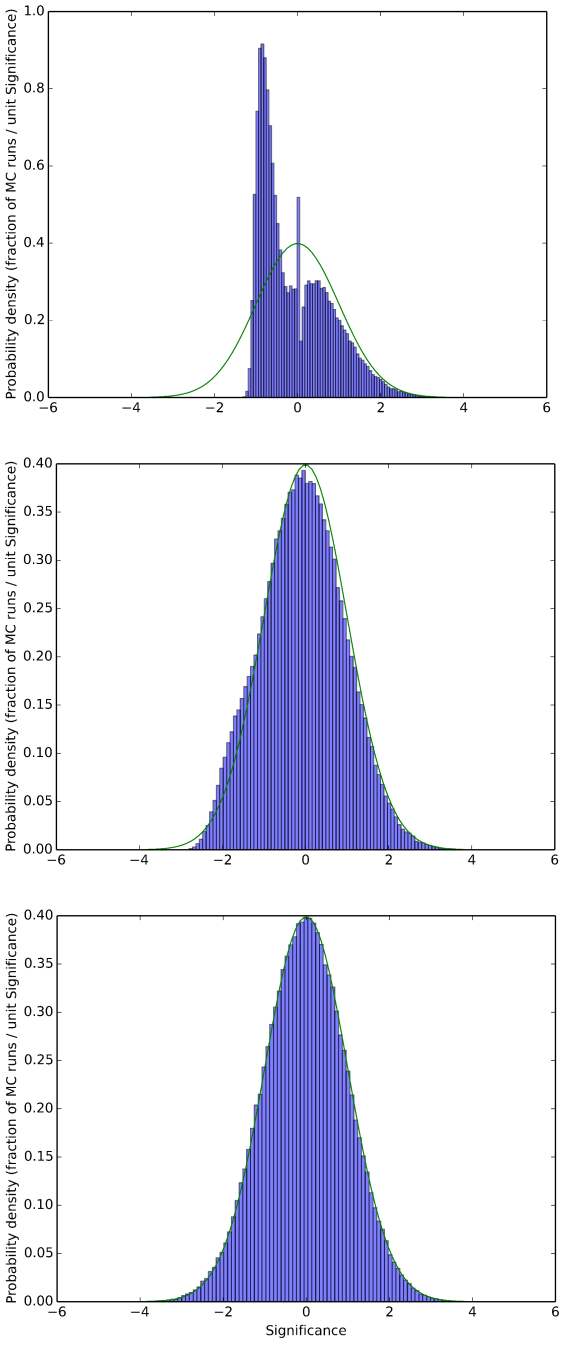


FIGURE 4.10: Approach of the null hypothesis distribution to Gaussian in Monte Carlo simulation. **Top:** Background rate = 0.1min$^{-1}$. **Center:** Background rate = 1min$^{-1}$. **Bottom:** Background rate = 10min$^{-1}$.

## 4.5 Monte Carlo simulation with a time-varying background rate

In order to further be able to test and tweak the C++ code written for VEGAS (in particular the *VATimedLikelihood* class), we decided to link it to our Monte Carlo code using the *Boost.Python* library. This enables us to:

- Test the C++ code for errors and debug them using simulated data in Python.
- Adjust the values of free parameters in the code by testing on realistic simulations (one such example will be discussed in Figure 4.14).
- Test the validity and tolerance of the method described in § 3.2.3.
- Establish a significance value for an observation when Wilks' theorem fails, as in the case of low statistics. This is done by numerically estimating the probability distribution of the test statistic under the null hypothesis.

After successfully linking *VATimedLikelihood* to our Python code, we began to test the method described in § 3.2.3 under the null hypothesis, with simulations of pure background which varies in time. Wilks' theorem implies that $\sqrt{-2log\frac{\mathscr{L}_0}{\mathscr{L}}}$ is distributed as a unit Gaussian. However, there are reasons to expect some deviation from that behavior:

- Wilks' theorem is only valid in the limit of high counting statistics.
- Uncertainty in the background variability estimation, or $B(t)$, which is both statistical and possibly systematic. In *VATimedLikelihood*, $B(t)$ is computed (by default) as a running

average of 1000 *a priori* counts. This implies a $\sim 3\%$ statistical error. Increasing the width of the running average will reduce this error, but will be unable to capture short time scale variations in the background rate (1000 counts in the VERITAS FOV are typically produced in about 5 minutes, if the softest set of cuts are used).

- Note that the statistical and systematic uncertainty of the $\alpha$ parameter is another problem not captured by our modelling, which is true even for the standard Ring Background Model (Spengler, 2015). However, we expect the background statistical error to be dominant over the systematic one, which would mostly emerge from inaccuracies in the acceptance separability assumption: $A(r,t) \approx R(r)T(t)$.

### 4.5.1 The null distribution under a time-varying background

Our Python Monte-Carlo simulation assumes that the separability assumption is correct, and simulates an *a priori* background region, an OFF region, and an ON region, with predetermined values of $\alpha$ and $\beta$. By simulating a region, we are referring to a Monte-Carlo generation of correctly-distributed arrival times for background counts. The behaviour of the background can be set to any time-varying function. In contrast to the previous subsection, no GRB signal is simulated, since we are interested in testing the behaviour of the TS under the null hypothesis.

The arrival times are fed into an likelihood estimation routine based on § 3.2.3 with an adjustable parameter for the number of counts averaged to determine background variability (a larger window lowers the statistical error but might be insensitive to quick variations in the background rate). This in fact is the Boost.Python version of *VATimedLikelihood*. Thus, our

Python simulations with a time-varying background are fed into the same C++ code that is used to estimate significance in VERITAS observations.

We modeled the background variation as a cosine function with an adjustable period: $b(t) = 2 + 0.6cos(2\pi t/P)$, with units in counts per minute. We also shifted the same function by a phase of $\frac{\pi}{2}$. We attempted to infer the significance of a possible gamma-ray burst that began 2 minutes prior to the onset of the run ($t = 0$), and that decayed as a power-law with an index of -1 ($1/t$). The first test conducted computed the RMS of the null significance distribution as a function of the period of the cosine function (Figure 4.11). Note that by adjusting the period (P) as well as the phase, one can simulate a monotonically rising or falling background rate during the observation.

For the purposes of detecting GRBs, we are more interested in the odds of obtaining a false high significance than the entire shape of the significance distribution. The most reasonable variability from the plot above (100min) was studied, and the odds of obtaining a high significance was plotted (Figure 4.12).

We conclude that any possible "widening" of the null significance distribution, whether it is an actual widening or a non-Gaussian tail, is minor in comparison to the gain in significance we predict for a gamma-ray burst.

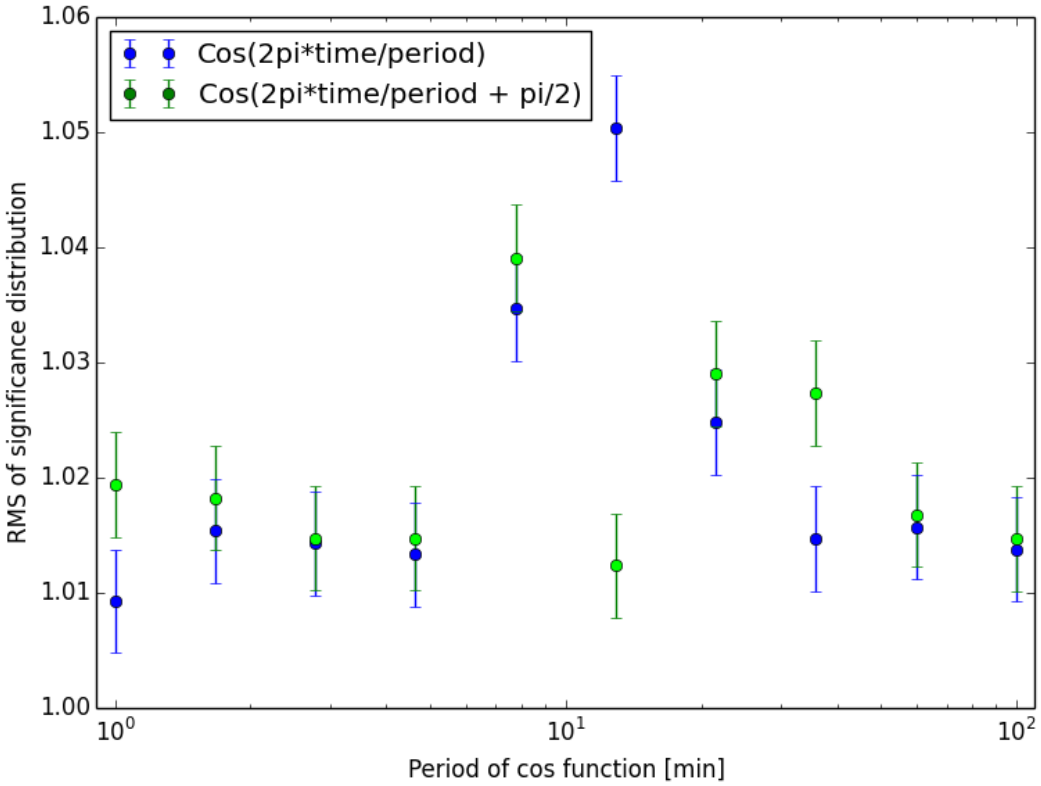


FIGURE 4.11: A cosine dependent background rate is simulated with different periods, and two different phases. We plot the RMS of the null distribution against the period of the cosine function. Note that the smaller time-scales are unrealistically small, outside of possibly very cloudy weather. The larger time-scales are slow enough to be realistic in good weather conditions, but may be fast enough to cause some problems with the test-statistic distribution.

### 4.5.2 Optimizing the time-bin size used for a priori background estimation

As described in the previous chapter, the time-dependent approach relies on the *a priori* background region to estimate the time-variation of the background. In *VATimedLikelihood*, this is done using a running time-average of 1000 counts, which corresponds to about 5 minutes under

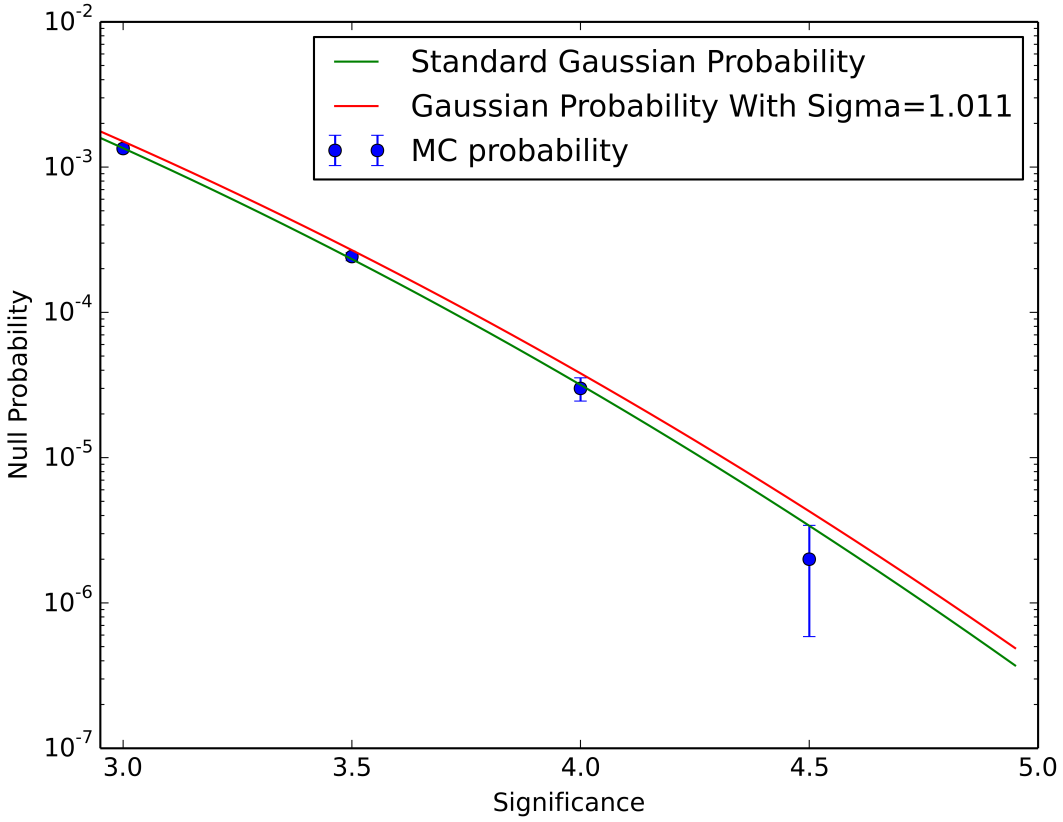


FIGURE 4.12: Studying a particular example from Figure 4.11, with a period of 100 minutes, we plotted the tail of the significance distribution with a million simulated observations. Against this are plotted standard unit-Gaussian probabilities, and a slightly widened Gaussian with the RMS obtained for the entire simulated distribution. The background rate used here is comparable to a current-generation IACT rate with soft cuts, or about 2 counts per minute.

the best circumstances (soft cuts and a small zenith angle). This implies a statistical error of about 3% and that the ability to catch a background varying on the scale of less than 5 minutes is minimal. The value of 1000 counts for the width of the running average is only a default and changeable for any user running a VERITAS analysis. Here we will use Monte Carlo simulations in Python to attempt to test and optimize the effect the size of the time bin may have. This is largely meant as a demonstration of the capacity of our Monte Carlo code, and will

need to be repeated by a user who is interested in replicating this for their particular source and experiment.

We begin with a test that includes the very rapidly changing background function $[1+0.5\sin(2\pi t/15\text{min})]\,\frac{1}{\text{min}}$, which is unrealistic in good weather conditions but may be justifiable in cloudy conditions.[9] However, the test is designed to test the limit of the mathematical approach we described, and may–as an added benefit–be useful for some other type of instrument. Because we associate 1000 counts in the FOV with about 5 minutes of observing, this short time scale represents the most interesting test scenario.

In Figure 4.13 we see that even in such rapidly changing conditions the time-dependent ring background model (another way of referring to § 3.2.3) has an RMS that only widens by $4-5\%$ compared to Li & Ma. In comparison, the time-dependent (TD) likelihood which assumes a constant background rate (§ 3.2.2), has an RMS that widens by 9.5%. One can naturally expect that TDRBM will outperform the TD likelihood in this test by a more significant amount when the period becomes larger than 15 minutes, but at the same time the amplitude of background variation remains high.

We now change the period of the background to 50 minutes, which is still exceedingly large and fast, as it implies 50% background rates swings in approximately 12 minutes. In Figure 4.14, we plot the RMS of the null significance distribution against the size of the *a priori* running average. While a larger number of simulations may be needed to establish a definite result, we find the lowest RMS (1.03) for a width of about 300 counts; it is a reasonable compromise between statistical error and fast response time. This demonstrates how a careful user may want

[9] Note that cloudy conditions usually represent a *spatial* problem in the background rates as well as a temporal one. In those cases, it is essentially hopeless to expect a well behaved significance distribution using any method outside of an ad hoc artificially large background assumption or something of that sort.

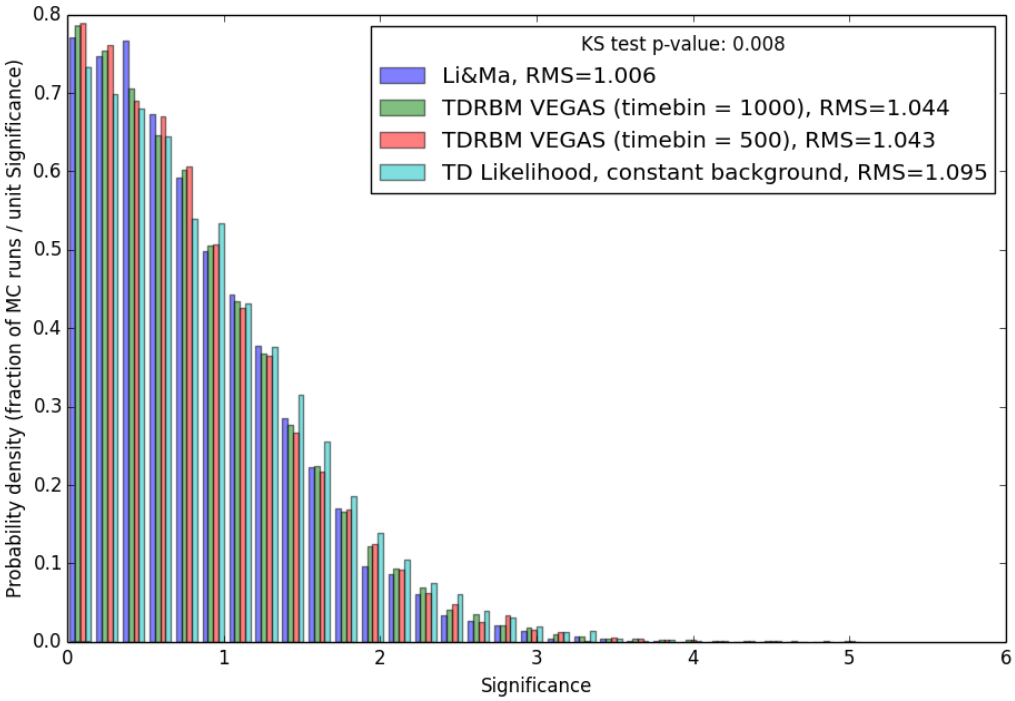


FIGURE 4.13: Testing the significance distributions of different likelihood methods under a rapidly varying background rate described by $[1+0.5\sin(2\pi t/15\text{min})]\,\frac{1}{\text{min}}$. Note that in this case we map all significances to a positive number, which will not affect the RMS. We use the time-dependent background approach (TDRBM) with two widths for the *a priori* moving average of 500 and 1000. We also test the time-dependent approach that assumes a constant bacgkround rate (TD Likelihood), and the Li & Ma method. While as expected, both time-dependent methods show widening of the distribution, TDRBM performs significantly better than the time-dependent method with the assumption of a constant background rate.

to approach optimizing the size of the time-bin, but more studies are needed to know which size is ideal under different circumstances. For now, our tests do not show an urgent need to depart from the default value of 1000.

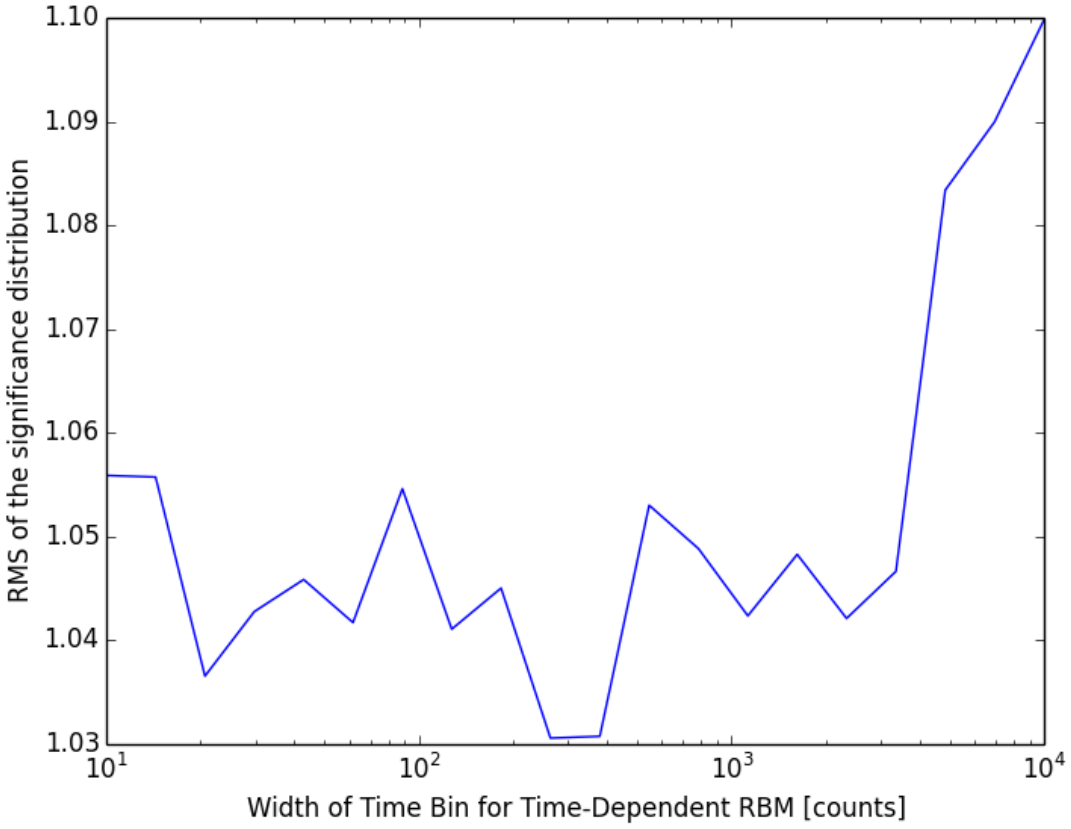


FIGURE 4.14: A background rate of $[1+0.5\sin(2\pi t/50\text{min})]\,\frac{1}{\text{min}}$ is simulated. We then tweak the size of the of the time-bin used for the *a priori* running average, and plot it against the RMS of the null significance distribution. The optimal size of the time-bin we find is 300 counts, with a corresponding RMS of 1.03 (although the statistics are not high enough to make a conclusive statement on the optimal size of the time-bin).

## 4.6 Summary

We derived a new time-dependent test statistic for the purpose of detecting sources with highly variable light curves. The derivation yielded a elegant result that can be readily compared with the standard Li & Ma test statistic. This can provide useful insight into when it becomes important to apply this technique. Furthermore, since the number of time bins approaches infinity,

highly variable sources can be tested without a high computational burden, as long as the time-stamping of events is accurate enough. After testing our technique on simulations of gamma-ray bursts, we conclude that it is effective and robust, increasing the sensitivity to detection appreciably.

# Chapter 5

# Angular reconstruction for large zenith-angle observations

## 5.1 Introduction

Reconstructing the incoming angle of the primary is one of the most crucial aspects of Cherenkov array shower reconstruction. Consider that a mere 10% improvement in angular resolution, assuming locally uniform background rates, corresponds to a reduction of $\sim 20\%$ in background levels (due to an ability to search for a source in a smaller test region). This, in turn, corresponds to roughly 10% improvement in the expected significance for a given source observation, and approximately 20% reduction in the observing time required to reach a standard significance associated with detection.[1] The latter is true in the limit of well-understood and modelled background, and is also a good approximation in the case of a more realistic test-statistic as devised

[1] This threshold is typically defined as the equivalent of 5 Gaussian standard deviations

by Li & Ma (Li and Ma, 1983).

Other advantages to better angular resolution:

- Separating distinct nearby sources.
- Getting a purer signal/background ratio, allowing us to study characteristics of a source more accurately.
- Better source localization.

In this chapter, we will explore the two standard methods for angular reconstruction of Cherenkov showers: the geometrical method, and the Disp method. We will then discuss our work to improve the Disp method and our implementation of a new weighting method, attempting to take advantage of both methods at the same time.

## 5.2 The geometrical method

Consider the following facts:

1. When imaging an EAS, one generally expects to find an elongated axis, corresponding approximately to the original direction of motion of the primary particle.[2] We will term

[2] If the shower is imaged directly from below, it will appear roughly circular due to symmetry. While showers will rarely be imaged from "exactly" below, a shower with near-zero impact distance will be close to circular and will present a very large error in major-axis reconstruction. Any algorithm developed has to deal with this fact in a reasonable way.

this the major axis, and the perpendicular direction as the minor axis. The minor axis is sizable due to secondary shower particles traveling less-than-parallel to the primary particle's direction of motion. Practically, the major axis may be found by minimizing the sum of the squares of the signal distances, as was originally done by Hillas in 1985 (Hillas, 1985). See Figure 5.1 (center) for a cartoon depicting a major axis of an EAS image.

2. If this primary particle is a photon, and if the direction of motion is continued along an extension of this major axis, it will inevitably point towards the emitting astrophysical source, regardless of the orientation and location of the imaging apparatus. In other words, the source position lies either on the major axis or along its extension.[3]

3. A second or third imaging apparatus may conduct the same exercise. Typically, this image is taken from a different location on the ground, but the telescope is oriented in the same imaging direction (i.e. zenith and azimuth angles). In this case the major axis will have a distinctly different orientation due to a parallax effect, however, the source, being an astrophysical ("infinite") distance away, will not suffer from parallax and will be located at the same point on the imaging plane.

4. One can overlay the images produced by multiple imaging instruments–which are all pointing in the same direction but physically distant on the ground–and expect all major axes to intersect at the source location.

This is the basis for the geometrical method of angular reconstruction, henceforth known as Geo. An example can be seen in Figure 5.1. In practice, when more than two images of a

[3] If the primary particle is charged, it will have been bent in magnetic fields on its way to Earth and thus lost its information of origin.

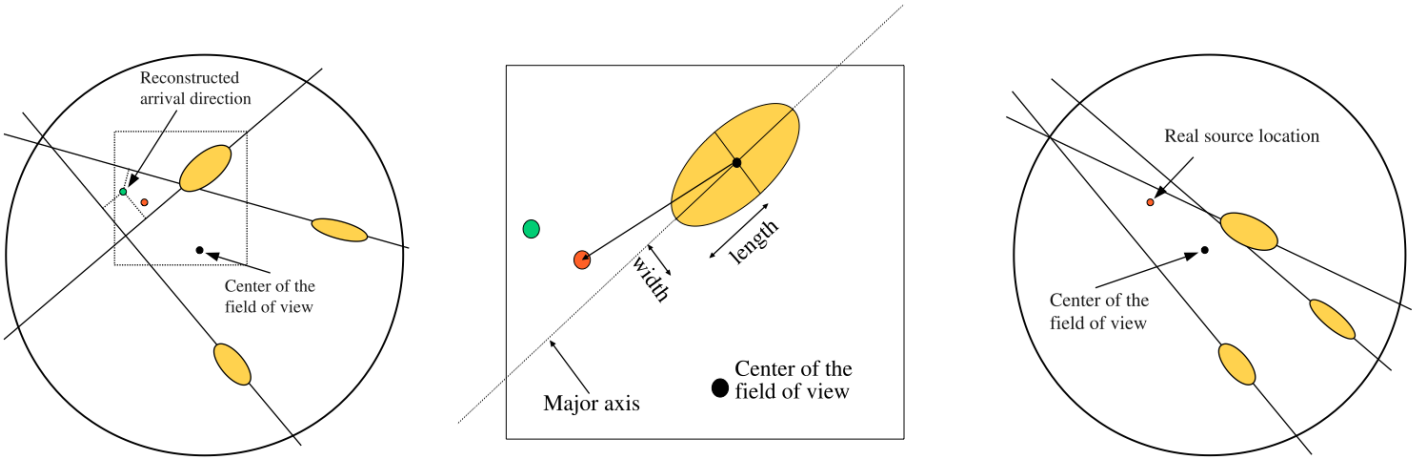


FIGURE 5.1: Demonstration of Hillas parameterization and the geometrical method, from Sentürk (2011). The red dot represents the position of the source. **Center:** a cartoon of a parameterized EAS image. A major axis is found by minimization of weighted squares as done in Hillas (1985). Then, the first moment defines the center of the image. The second moment in the major axis direction is termed Length, and in the minor axis direction, Width. **Left:** multiple stereoscopic images are combined, and the geometrical method is applied to reconstruct the source position. Pairs of telescopes disagree on the position of the source, and a weighted average is used to determine the green dot as the reconstructed position. **Right:** another attempt at geometrical reconstruction. This time, the major axes are nearly parallel and the resulting positional error becomes unacceptable.

Cherenkov shower are overlaid, they will rarely (never) intersect at a single point. This fundamentally has to do with imaging noise and EAS statistics:

- Camera noise and photon statistics, involved in imaging the shower.
- Statistics involved in shower development, which may in some instances, point the major axis away from the primary particle's direction of motion. To understand this, we can consider an electron-positron pair produced by a primary photon, coming from above the atmosphere; the electron has some momentum towards the right and the positron towards the left. Suppose the electron on the right happens to travel substantially further than the positron on the left, before producing a photon, which then also travels less than expected before pair-producing once-again (whereas the photon on the left immediately pair-produces). This will have the effect of "tilting" the appearance of a shower and misdirecting the major axis. Using Monte Carlo simulations, we have been able to find the typical error in the major axis direction to be on the order of 5 degrees, but the exact amount of error depends on cuts used for shower selection. For example, picking only the brightest EAS images will produce a better result, while sacrificing effective area.[4]

The final position is then found by some kind of weighted averaging of intersection points between pairs of telescope images. If the imaging instrument observes the shower from close to overhead, it is more sensitive to any noise because the image is nearly circular. In a reasonable weighting scheme, intersection points involving such nearly circular images will be weighted less favorably in the reconstruction process. In the next subsection, we will discuss the Disp

[4]This is in fact a central issue related to angular reconstruction. Any real improvement in angular reconstruction should be able to do so without sacrificing effective area.

method, another approach to angular reconstruction–which in fact performs well under such circumstances.

## 5.3 The Disp method

There are instances when the geometrical method becomes susceptible to error and is better replaced by an alternative method (more on those particular instances in the next subsection). Luckily, one such method exists: the Disp method was originally used by the Whipple 10M telescope for direction reconstruction using a single telescope, where the geometrical method cannot be used (Lessard et al., 2001). To see how the Disp method is realized consider that:

- When imaging an EAS that is overhead, one can expect the image to appear nearly circular, due to symmetry in shower development.
- As one moves further away from the overhead direction, the image becomes elongated along the direction of motion of the primary. The ratio of the elongated dimension to the non-elongated one will continue to increase as one moves away from overhead.
- If the telescope location is fixed, but the primary particle is made more energetic, the true length of the shower is likely longer, and thus will appear to be longer on the imaging plane.

Thus we arrive at the conclusion that elongated showers are typically more energetic or suffer a larger parallax angle compared to overhead. This parallax angle is defined as the angle between the image centroid and the source position on the camera image. We define the Disp angle as

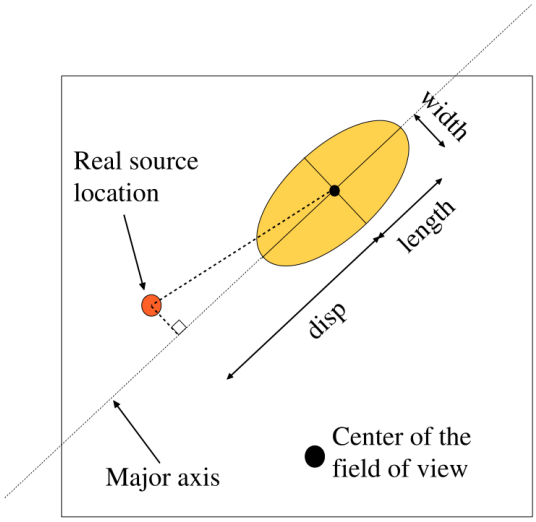


FIGURE 5.2: Demonstration of Hillas parameterization with the Disp parameter, from Sentürk (2013). The real source position is marked with a red dot. The major axis and other parameters are then found as discussed in Figure 5.1. Due to various errors, the true source position lies slightly away from the major axis. Disp is defined as the projection of the distance between the source the center of the image along the major axis.

the projection of this parallax angle along the major axis of the shower image (see Figure 5.2). Since not all showers originate from particles of identical energy, a simple table converting the elongation ratio to the Disp angle cannot work. What is typically added in the most basic Disp version is the brightness of the image, to serve as a proxy for the shower energy. This brightness is usually calculated as the sum of all PMT counts in the image.

Figure 5.2 shows a depiction of what we just discussed, formally known as a Hillas parameterization. An elongated shower is characterized by the first moment along the major axis, defined as *Length*, and along the minor axis, defined as *Width*. The parallax angle is known as *Disp*. The sum of all counts within the image is defined as the *Size*.

In VEGAS, the original implementation of the Disp method involved only those three quantities,

and a table converting them into a Disp angle (Sentürk, 2011). This *Disp table* was created by averaging images from a Monte Carlo simulation of EAS showers imaged by VERITAS. If multiple telescope images are available, some kind of weighted averaging is then done to find a final source position. The weight assigned to each image can depend on how reliable it is deemed to be based on many possible factors.

Later in this chapter, we will describe an analysis done by the author of this work to improve on the original Disp method and study possible variations on the approach and how they affect the angular resolution.

### 5.3.1 Head/tail ambiguity

One weakness the Disp method exhibits is that it typically makes no distinction between both directions of the major axis. That is, the Disp approach gives the absolute angle of parallax, but not its "sign", which would choose which direction to follow along the major axis to get to the source. The reason the sign presents more of a challenge is that the geometry of the EAS often creates an image that is nearly symmetric between the top and the bottom of the shower (the top of the shower, while narrower, is brighter and thus can have a similar apparent size to the bottom of the shower). The symmetry between "head" and "tail" is not a precise one, and can sometimes be decided by a separate table, which may use parameters outside of the ones we discussed to make the distinction.

There are two approaches to typically deal with the head/tail ambiguity:

- One can create a classifier that uses some other shower parameters to attempt to distinguish the "head" and "tail" as a separate process from the Disp estimation. This should

be feasible at least partially because we do not expect exact symmetry in the imaging of the top and bottom of the EAS, nor do we expect arrival times of photons in the image to have such symmetry (timing information often plays a major role in head/tail classifiers).

- For stereoscopic observations with N telescopes, one can consider all head/tail combinations (of which there are $2^N$) and choose the one that leads to the smallest spread between the telescope-by-telescope position reconstructions. This is the approach used in VEGAS.

## 5.4 Combining Geo and Disp

In a memo written by M. Beilicke in 2010 (Beilicke, 2010), it was found that the angular resolution obtained by Geo deteriorates rapidly as the zenith angle of observation increases. We explain this as the result of one primary factor: the abundance of nearly parallel EAS images taken by the different telescopes. To see why this happens, we consider the size of the Cherenkov light cone. As discussed earlier, a telescope must be within the light cone to have a chance of imaging the EAS. As the zenith angle of observations increases, the showers observed have a correspondingly sharp angle to the ground, producing a large Cherenkov light pool. This means that many of the observed showers will have been detected substantially further away–in terms of core distance, or distance from the natural landing position of the primary–from a fairly compact array of 4-telescopes, such as VERITAS (with inter-telescope distances of $\sim$ 100m). Those distant showers differ much less in parallax between image to image, when compared to those showers that would naturally "land" much closer to the center of the array.

The Geo method thus suffers from redundancy; since it relies on parallax between multiple telescope images, it fails in the limit of multiple nearly identical images. The Disp method,

however, relies on parallax between the shower center and the source position in the sky (i.e. compared to overhead). Thus, it does not suffer comparable deterioration.

Beilicke plotted the 68% containment radius of reconstructed event angular error (a measure for the angular resolution) as a function of the cosine of the zenith angle of observation. He did this for both Disp and Geo, both of which were applied to Monte Carlo simulation data. What he found can be seen in Figure 5.3. As mentioned, this plot shows a rapid deterioration of the Geo angular resolution with increasing zenith angle.

Beilicke used the dependence he found on the zenith angle to define a new angular reconstruction technique, which he terms *geo/disp*. It is defined as a weighted sum of Disp and Geo, where mathematically $'geo/disp' = w \times Disp + (1-w) \times Geo$. On the camera plane, a straightforward definition of this weighted sum is applied: one draws a connecting line between the Disp position and the Geo position and selects the source position as the point on that line such that the distance from the Disp position is $\frac{1-w}{w}$ times the distance from the Geo position. This is equivalent to interpreting the mathematical definition above as a vector sum in the camera plane. The weight in question varies as a function of the zenith angle of observation, $w = w(\theta_z)$.

To find an optimal weight for every zenith angle, Beilicke studied Monte Carlo simulation data at various zenith angles, optimizing the value of $w$ for each separately by computational trial and error (by minimizing the 68% containment radius). The values that he found were then fit into analytical form:

$$w = \begin{cases} 1 & cos(\theta_z) < 0.4 \\ e^{-12.5 \times (cos(\theta_z) - 0.4)^2} & \text{otherwise} \end{cases} \tag{5.1}$$

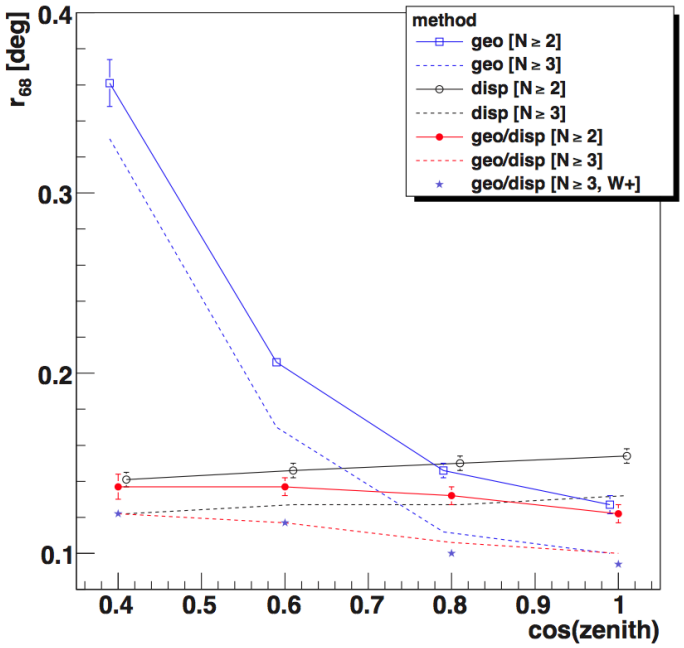


FIGURE 5.3: Angular resolution of Disp, Geo, and a new weighted method (geo/disp), taken from Beilicke (2010). The angular resolutions of all methods are plotted as a function of the cosine of the zenith angle of observation. The angular resolution is calculated with Monte Carlo simulations, by computing the 68% containment radius of randomly generated events. A cut on the number of telescopes with useful images is also made, something which is not discussed here and does not seem to affect the conclusion. This cut is made either for at least 2 or at least 3 and is denoted by N in the legend. Denoted by W+, there is also an attempt to modify the weighting scheme for the images, without much consequence. We shall focus on the main conclusion of this plot, which finds a severe deterioration of angular resolution in large zenith angles for Geo, and no comparable effect for Disp. The new weighted method outperforms both Disp and Geo at all zenith angles, as expected. Somewhat more surprisingly, the new weighted method provides appreciable improvement in intermediate angles as well.

At small and large zenith angles, Geo and Disp dominate the weighting scheme, respectively.

This weighting scheme will later be known as Method6 in VEGAS, which is the term we will use from now on. Method6 has been shown to be successful by Beilicke in his memo, and while this should be evident by our previous discussion for small and large zenith angles, it also turned

out to provide appreciable improvement over both techniques in intermediary zenith angles. In her thesis, G. Senturk has continued this work and found similar results (Sentürk, 2013).

## 5.5 An improved weighting scheme: weight tables

### 5.5.1 Introduction and derivation

The improvement Beilicke found for intermediate zenith angles has led us to consider a new approach for angular reconstruction. We will depart from Beilicke's analysis in two fundamental ways:

1. While Beilicke relied on the zenith angle alone to determine the weight $w$, we will not similarly restrict our analysis. We've argued that the zenith angle is only correlated to the angular deterioration in Geo, which is truly caused by showers that land far from the array, causing images taken by the different telescopes to appear nearly identical. Thus one can have the weight depend directly on a quantity that relates to the impact distance of the EAS (or how close to parallel the major axes are). As an example, we define $stdPsi$ as the RMS of all major axis angles between couples of telescope images (where only bright and legible images are selected). A cartoon demonstration of calculating $stdPsi$, as well as a histogram of this quantity can be seen in Figure 5.4. We will see that the energy of the primary also plays a major role, and can potentially be included in a weighting scheme. This opens up the possibility of a weight factor that depends on multiple parameters.

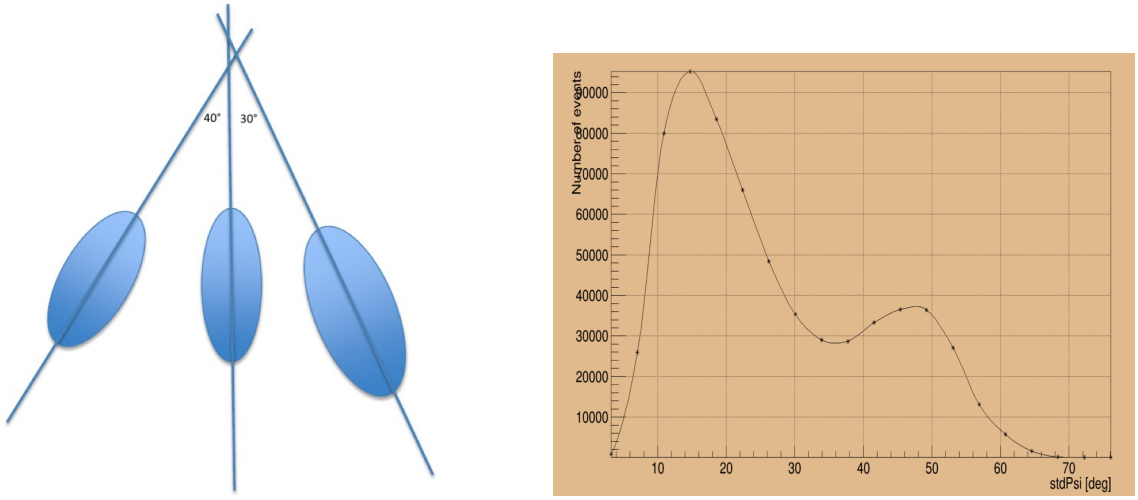


FIGURE 5.4: The *stdPsi* parameter: cartoon and histogram. **Left:** a cartoon demonstration of an event and the angles between pairs of axes, those being: 30°, 40°, 70°. We calculate this event to have $stdPsi = \sqrt{30^2+40^2+70^2} \approx 49.7°$. **Right:** A histogram of *stdPsi* for Monte Carlo events produced at a zenith angle of 45°.

2. We will use a more rigorous mathematical approach to finding an optimal weighting scheme, as explained below.

Consider two random variables representing the angular errors of Disp and Geo: $D$ and $G$. In practice, there will be 2-dimensional vectors on the camera plane corresponding to two separate axes, $x$ and $y$, and the error associated with each. One can repeat our analysis for each axis individually, so for now we can assume we are referring to the $x$ axis angular error without loss of generality. We will attempt to find a weight ($w$) that will minimize the error of a weighted sum of both Disp and Geo: $w \times Disp + (1-w) \times Geo$. To discover the optimal weight one needs to apply, we begin by assuming that both $D$ and $G$ are unbiased: that the expected value of the error vanishes, or is at least very small compared to the RMS. We will require this quality to hold for reasonably defined subsets of all events. For example, one may choose to define $D$ only over those showers that have a small Length, and abnormally large Width, and still expect

our assumption to hold. The fundamental reason we expect this to be true is based on different reasons for Disp and Geo:

- Disp is by definition derived from a Monte Carlo sample of EAS, distributed in a manner true to the physical distribution of such showers. As the sample of showers increases, the error in the Disp method will be attributed to shower statistics and camera noise, both of which are incorporated into the MC sample. We believe this error to be irreducible (Hofmann, 2006). However, a large enough sample of MC events will cause the mean error in Disp to vanish.

- The error in Geo is expected to be RMS dominated by reasons of symmetry: every shower as viewed by an array of telescopes can be rotated around the geometrical array center by 180 degrees (assuming the telescopes are arranged in a symmetric way, which is approximately correct for VERITAS). As long as such symmetry is preserved, we can expect any subgroup of showers to have a small mean error compared to RMS.

One final note is that if one does find a mean error in Disp for a subset of showers that is defined by the Disp parameters (recall those are Width, Length, and Size), it is highly encouraged to correct for this error rather than incorporate it into a weighting scheme.

Empirically, we will show results later in the chapter confirming our suspicions above, showing that for a large enough sample of MC events, the RMS in error is much greater than the mean (for thousands of events we find a typical factor of approximately $\frac{RMS}{mean} = 10$).

From here on, we will use basic statistics theory to find an optimal weight that will minimize the RMS of the resulting weighted random variable. For intuition, it may be worth repeating

some results routinely derived in basic probability theory: When two *uncorrelated* random variables with similar variances are averaged, the resulting random variable has its variance halved. If the two random variables are perfectly correlated (as in being one and the same), this averaging scheme will lead to no reduction in noise levels. The discussion above on Disp and Geo demonstrates the possible different sources of error they have, as well as those that are somewhat similar, such as image noise. We expect their errors to be somewhere between uncorrelated and fully correlated. We will later show their correlation to be moderate.

To find an optimal weighting scheme between Disp and Geo, we define a new random variable $R = wD + (1-w)G$. We will first compute the standard deviation of $R$ ($\sigma_R$) as a function of the standard deviations of $D$ ($\sigma_D$) and $G$ ($\sigma_G$):

$$\begin{aligned}\sigma_R^2 &= < (R - < R >)^2 > \\ &= < R^2 > \\ &= < w^2D^2 + 2w(1-w)DG + (1-w)^2G^2 > \\ &= w^2\sigma_D^2 + 2w(1-w) < DG > + (1-w)^2\sigma_G^2,\end{aligned} \tag{5.2}$$

where $< X >$ stands for expected value of $X$, and one notes that as the sum of two random variables with vanishing means, $R$ must have a vanishing mean value as well. We shall also note that $< DG >$ corresponds to the covariance between $D$ and $G$, due to their vanishing mean values. We shall denote this as $C_{DG}$.

We can now find an optimal value of $w$ by finding where the derivative of $\sigma_R$ with respect to $w$ vanishes:

$$\begin{aligned}(\sigma_R^2)' &= 0 \\ &= 2w\sigma_D^2 + (2-4w)C_{DG} - 2(1-w)\sigma_G^2.\end{aligned} \tag{5.3}$$

Which gives us the following solution for $w$:

$$w_{opt} = \frac{\sigma_G^2 - C_{DG}}{\sigma_D^2 + \sigma_G^2 - 2C_{DG}}. \tag{5.4}$$

This expression can be written in a more compact notation by defining the correlation coefficient, $c = \frac{C_{DG}}{\sigma_D \sigma_G}$, and the ratio of the standard errors as $r = \frac{\sigma_G}{\sigma_D}$:

$$w_{opt} = \frac{r - c}{r + \frac{1}{r} - 2c} \tag{5.5}$$

(one consistency check for this solution is to invert $r$ into $\frac{1}{r}$ by assuming that we had defined $w$ and $1-w$ in reverse; that is, the former would apply to Geo and the latter to Disp. Then, we add this new expression to the original and find that both weights add to 1).

### 5.5.2 Implementation

To implement the weighting scheme concept in VEGAS, a few things must be considered. First, one has to choose a parameter space over which to produce the weights. For example, one may choose the zenith angle of observation (as Beilicke did), and the (reconstructed) energy of the shower, which will produce a 2-dimensional weighting scheme. One then has to choose

reasonably defined bins over this parameter space. For every bin, a set of Monte Carlo instances is found in simulation data, and $r$ and $c$ are estimated using standard estimators for covariances and standard deviations of a sample. Then, Equation 5.5 is applied to find the optimal weight for this bin. A table is constructed and optimal weights are stored in it. This table, henceforth known as a *weight table*, is stored on a hard drive in the local computer. A separate piece of code then has to be written in the VEGAS package. When a VEGAS analysis is run on a VERITAS observation, this code will find the correct bin for every event, go into that bin in the weight table, and apply the correct weighted average of Disp and Geo based on its findings.

For brevity, we will only discuss some of the details involved in the above description, since there many ways of achieving all steps above, most of which are straightforward and pose more of a coding challenge than a conceptual one.

One of the major concerns in constructing a weight table is choice of parameter space. One would like to find a parameter that exposes at least one of two things: a strong dependence of the resolution ratio, defined as $r$ above, or a strong dependence of the correlation coefficient, denoted as $c$. For example, we know that the zenith angle, as found by Beilicke, is suitable for the former. The error in Geo increases strongly above a certain zenith angle, whereas Disp stays approximately the same, causing $r$ to be strongly related to the zenith angle. One may consider in place (or in addition) some measure of how identical different telescope images are, as we postulate this as the source of Geo's deterioration.

One such possibility is $stdPsi$. To answer whether it is a good parameter, we first study the dependence of Disp and Geo resolution on this parameter. What we find is somewhat surprising. While we do see a pattern of Geo declining in performance as $stdPsi$ decreases, we also observe (see Figure 5.5):

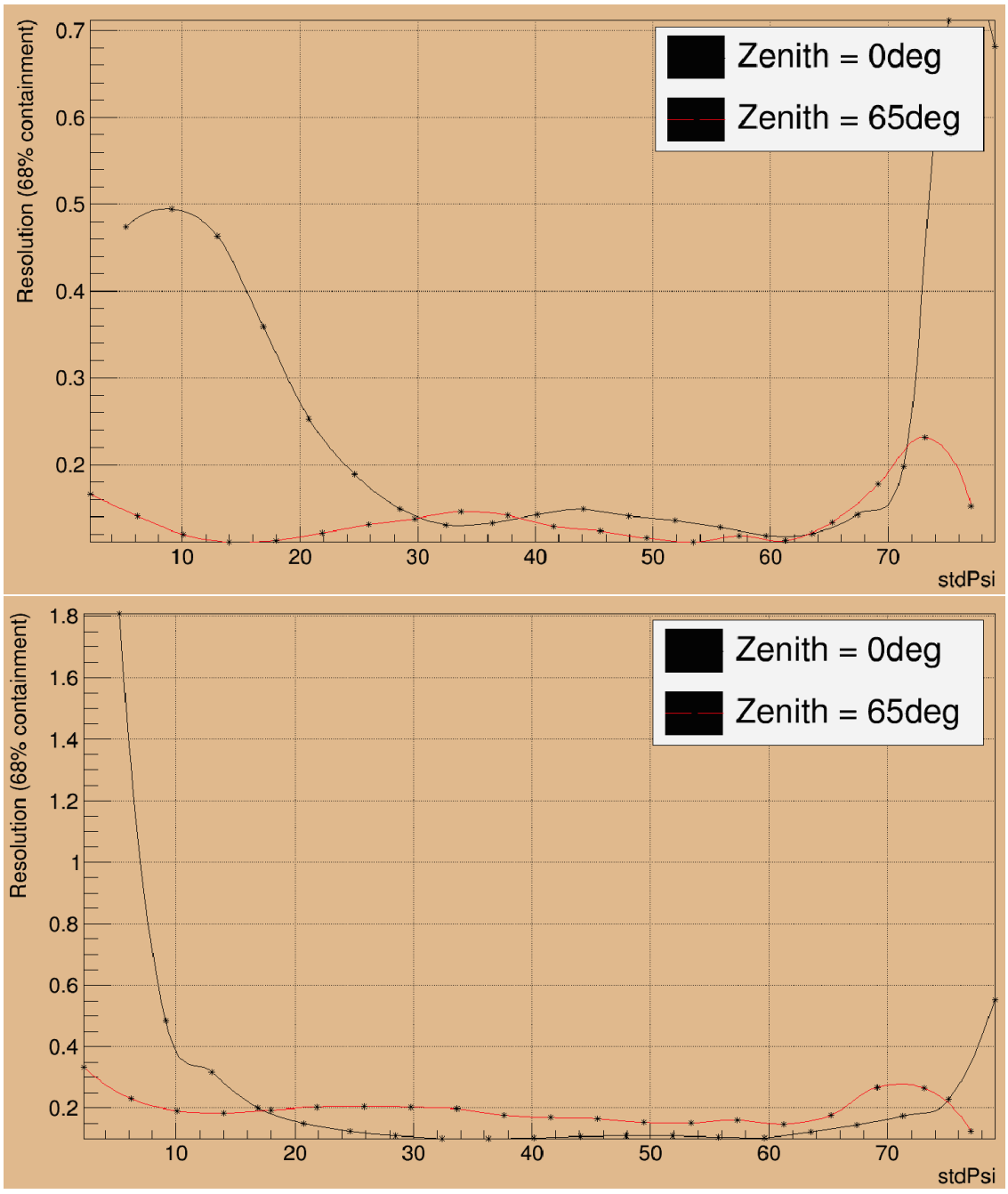


FIGURE 5.5: Resolution plots of Disp and Geo as a function of *stdPsi* at small and large zenith angles reveal the complexities of this analysis. **Top:** Disp (Method5) performance as a function of *stdPsi*, for a zenith angle of 0° (black) and 65° (red). **Bottom:** Geo (Method0) performance as a function of *stdPsi*, for a zenith angle of 0° (black) and 65° (red). Both x and y axes are in degrees.

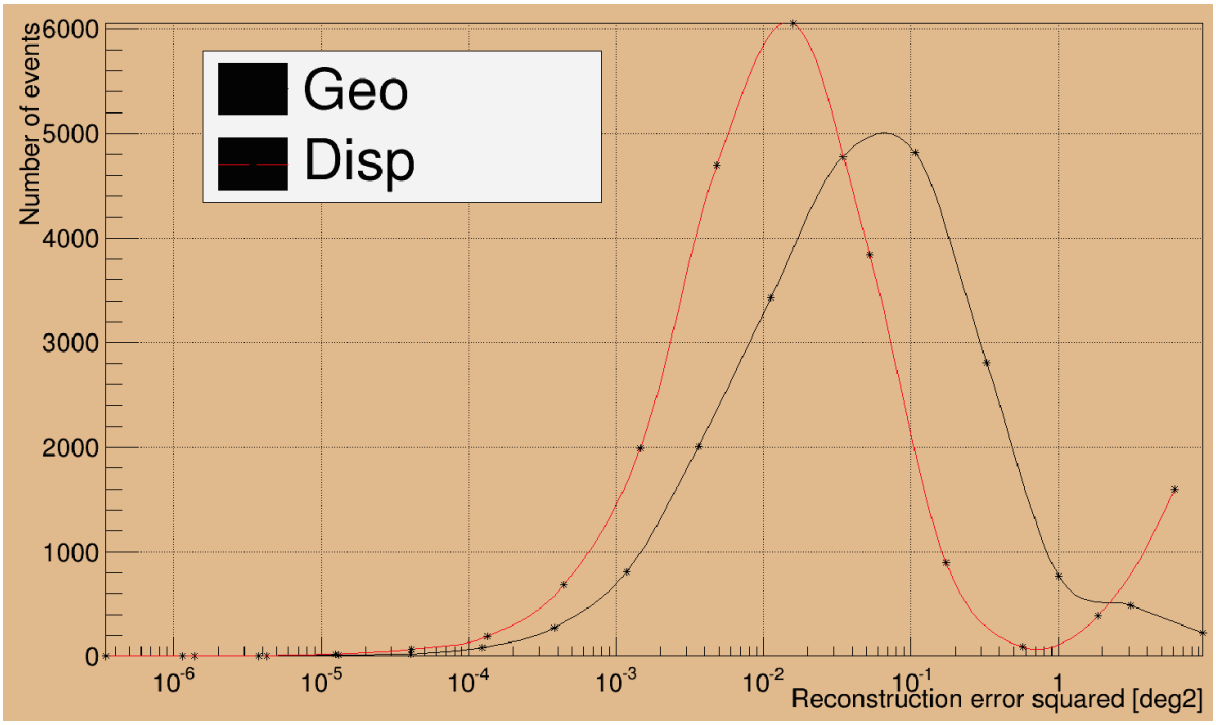


FIGURE 5.6: A deeper look into the angular error distributions of Disp and Geo for nearly parallel, large zenith events. We select all Monte Carlo events with $stdPsi < 5°$ at a zenith angle of 65°. The Disp distribution appears to be bimodal due to head/tail ambiguity.

- At the lowest values of *stdPsi*, there is a dramatic loss in performance for Disp. In fact, for the lowest *stdPsi* and small zenith angles, Disp performs almost as poorly as Geo.
- Disp outperforms Geo even for large *stdPsi* at a LZA. This clearly means that the zenith angle dependence of resolution is not fully replaceable by *stdPsi* (it may still be replaceable by other measures of the multi-telescope image angles).

We conclude that *stdPsi* is a useful parameter, but should not stand in place of the zenith angle, but rather in addition to it. One could attempt to explain our findings as a separate exercise. We will speculate that Disp may be performing poorly at very low *stdPsi* values due to the lack of sufficient statistics in Monte Carlo simulations that fall within those values, in addition to

the head/tail ambiguity. Nearly parallel images are likely to especially impact head/tail decisions that are done using the second approach described in § 5.3.1 (as is the case for VEGAS). However, Figure 5.6 should demonstrate that head/tail ambiguity cannot by itself explain the dramatic decline in performance, because the 68% containment is not highly affected by the relatively small percentage of events at the tail of the distribution.

Another parameter of importance is the energy of the primary. We have the privilege of studying it unambiguously, due to the fact that the Monte Carlo simulations provide us with a correct value for every event (rather than a reconstructed value). Our results consistently show a declining angular resolution for high energy events for the Disp method, especially at small zenith angles. Practically, it is difficult to use the energy as a parameter for the weight table, because the way it is calculated requires the angular reconstruction to be done first. To use the energy in the weight table, one would have to give a first estimation of the angular position, calculate the energy, and go back to producing a more accurate position. We will therefore choose a proxy to represent the energy, using the average Size of all images observed by the telescopes.

Some additional parameters we have considered for the weight table (this is not an exhaustive list):

- *Loss*: Some EAS images, especially those that are of high-energy primaries, or far off-center, are truncated at the edge of the camera. While this would hurt the performance of both reconstruction methods, it would likely have especially negative consequences for the Disp reconstruction (since it relies heavily on the elongation of the image). The *Loss* parameter is defined as the sum of signals in edge PMTs (in the outer ring of the camera) divided by Size.

- *Time Gradient*: Recall that particles in the EAS travel faster than the atmospheric speed of light. Thus if one is imaging a shower from underneath, the photons emitted from the top of the shower will arrive after those from the bottom. Conversely, if the shower has a distant landing position, photons from the top of the shower will arrive first, because they are taking a direct path to the telescope. There are some showers that are oriented in between those two extremes and have a very small time-gradient between arrival of photons from the top and bottom, and thus the entire EAS image arrives almost immediately. Thus calculating the difference in arrival times of photons along the major axis, typically in nanoseconds-per-degree, can be a useful measure of EAS orientation (it has been used in the past to resolve head/tail ambiguity).

- *Number of telescopes*: Here we are referring to the number of telescopes that have good quality images that can be used for reconstruction. The geometrical method requires at least two telescopes (in a typical analysis if only a single telescope has a good quality image, the event is not reconstructed). One can imagine some interesting information residing in the combination of the telescope number and some of the other parameters. For example, a small *stdPsi* value combined with a small number of telescopes, should certainly favor the Disp method. How much would this change when there is a large number of telescope images available?

- *RMS of reconstructed positions:* In the Disp method, there will be telescope-by-telescope spread in the reconstructed position, and in the Geometrical method the same would apply to any pair of telescope images which represent an intersection point. This spread could represent valuable information on how well each method is able to reconstruct an event. One additional, similar quantity, involves the uncertainty in each Disp table bin which is

used in the reconstruction process. One has to be careful on how to weigh this uncertainty, which exists separately for each image in the multi-telescope reconstruction.

Note that for the quantities that are available for every telescope image separately, and thus multiple values exist for every event, we've implemented the possibility of using the sum, mean, standard deviation, min, max, and mean of the absolute values. Our process for finding the best weight table has been to produce plots as seen above, in addition to trial and error and mixing of parameters. There is often no replacement to a trial and error approach, because the multivariate nature of this analysis makes it difficult to notice useful patterns which may work well if implemented.

In creating a weight table for testing or application purposes, we bin the multi-dimensional table such that it will have about 100 to 1000 events on average in any single bin. Bins that have many events, are "printed"[5] during the process, in addition to bins that are selected by a random-number generator. We programmed this printing not only for testing how well the code that produce this weight tables works, but also for testing our assumption that $RMS/mean \gg 1$. We also print bins that have $RMS/mean < 3$ (if any exist). In the process we found that in virtually all large bins and randomly printed ones, the assumption of low mean error has held true (with a ratio of at least 5 or so, and usually much larger). The "high mean" bins always seemed to be a result of low statistics in a bin, with no more than a few 10s of events. Our tests provide a limited sample which affirms our assumptions, however one may want to use similar method to make sure their parameter choice does not violate the low-mean assumption.

[5]The "printing" of a bin involves a message that includes the number of events in the bin, values of parameter-space represented by it, and statistical parameters related to Disp and Geo reconstructions that were discussed in the text. The mean error of both Geo and Disp is printed as well, a quantity which was assumed to be small in the development of the method.

One important pitfall that we found in the process of making the weight table, is that our usage of standard deviations rather than 68% containment can sometimes be problematic.[6] The latter definition of angular resolution likely carries more significance in observations, whereas the former can give too much weight to extremely poorly reconstructed events. We noticed this tends to disfavor the Disp method, likely due to some events with head/tail confusion. Therefore, we have implemented a "threshold" for the calculation of standard deviations and correlation coefficients, where events with very poor reconstruction (say, $> 0.3$ degrees) are not considered in the weight table construction process (i.e., those events do not pass the threshold).

In Figure 5.7, we plot some interesting distributions that are found when producing a weight table. These examples are typical of what we would find regardless of parameters and threshold used in table construction. The plots show how the correlation coefficient and weight computed (using Equation 5.5) are distributed for all bins in the weight table. The distributions are weighted by the number of events in every bin. One can see a typically moderate correlation coefficient of around 0.5 (with a wide distribution, and even some negative correlations, which could potentially correspond to sparse bins).

The bottom plot in Figure 5.7 shows the distribution of weights, with the counterintuitive result that some are greater than 1 (or less than 0). This may seem surprising, and is a somewhat curious result of strong positive correlations with different error-scalings.

Consider a method that produces a reconstruction of the position with error $\varepsilon$, where $\varepsilon$ can be distributed in any way one pleases. Consider another method that produces an error that is scaled with respect to the first method, and otherwise identically distributed: $k \times \varepsilon$. These

[6] Both definitions of angular resolution are identical if the error distribution is Gaussian, however we have already seen that this is not the case, most notably due to head/tail ambiguity.

random variables will be perfectly correlated. It is trivial to show that a weight of $\frac{k}{k-1}$ will completely eliminate the error, and give an exact reconstruction every time. This weight exploits the different scaling of errors to eliminate it entirely; it is impossible to do so when $k = 1$. To what extent this phenomenon is realistically exploitable in angular reconstruction in difficult to say: it seems to require a very large correlation coefficient, as well as a large ratio of errors.

As a first test on the performance of the weight table, we produce angular resolution plots on the same Monte Carlo data that was used to produce the table. If the bins used to construct the weight table are large enough, they should accurately represent the statistical quantities of interest, and thus should not introduce a significant bias favoring the weighted approach (something one should always watch out for when building a method and testing it on the same data). In any case, the plan is to perform any final test on source observations, which will need to confirm results based on Monte Carlo simulations. Figure 5.8 shows the angular resolution obtained by one of the weight table implementations (termed Method9a), showing a good level of improvement that seems to be constrained by the limitations of the Disp method at the smallest zenith angles.

## 5.6 A new Disp method

### 5.6.1 Motivation and implementation

In Lu (2013), the H.E.S.S. experiment has found the Disp method to outperform Geo at all zenith angles in their analysis. As we've seen in the last subsection, the VEGAS method that had existed appeared to perform poorly at small zenith angles. We have decided to upgrade our

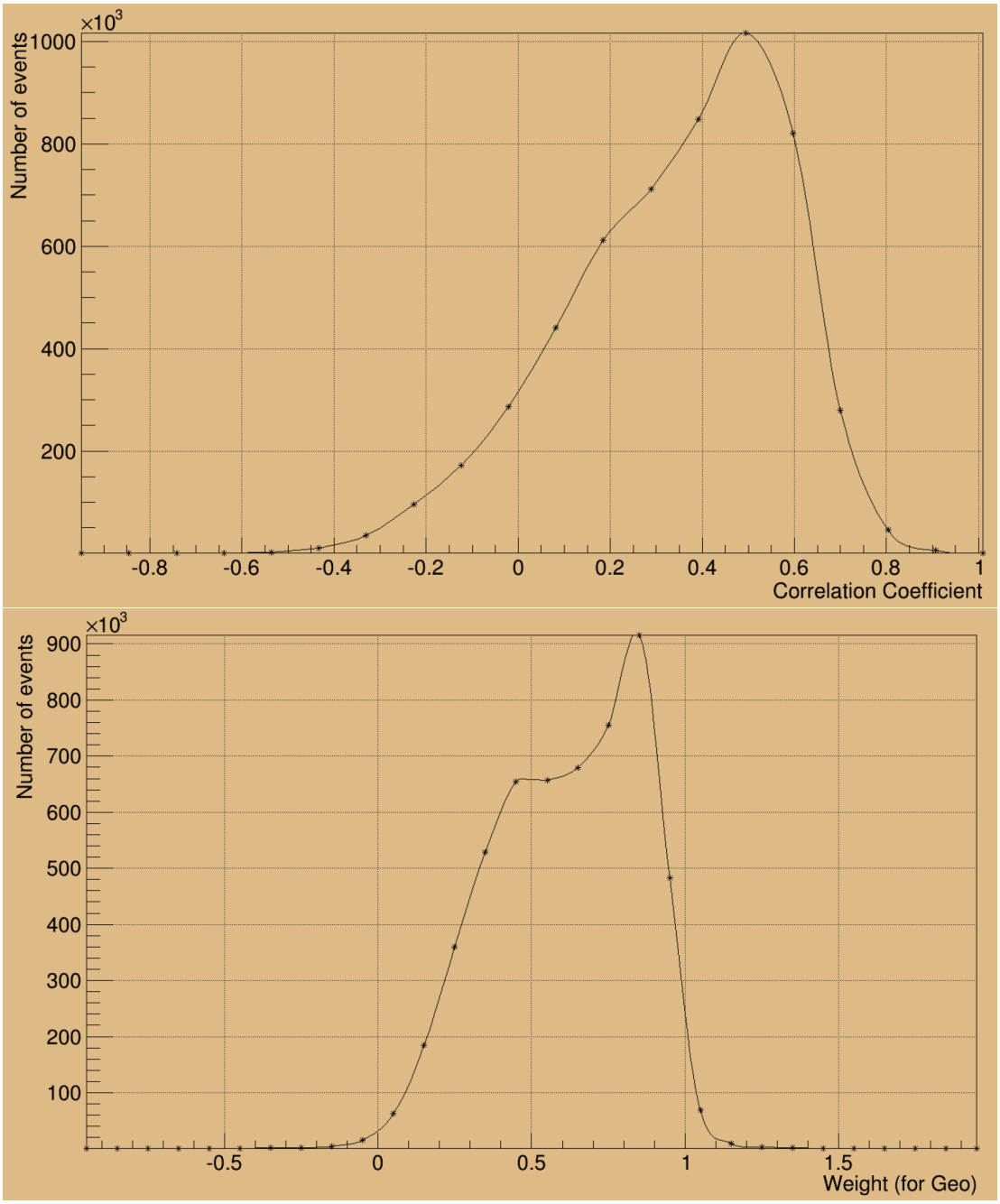


FIGURE 5.7: An example of distributions arising in the construction of a weight table. The distributions are of all bins constructed in the table, where each bin is multiplied by the number of Monte Carlo events within it. **Top:** Distribution of correlation coefficients, showing a typically moderate correlation between Disp and Geo errors. **Bottom:** Distribution of weights, notably with a small but significant fraction being greater than 1 or less than 0 (see discussion in text).

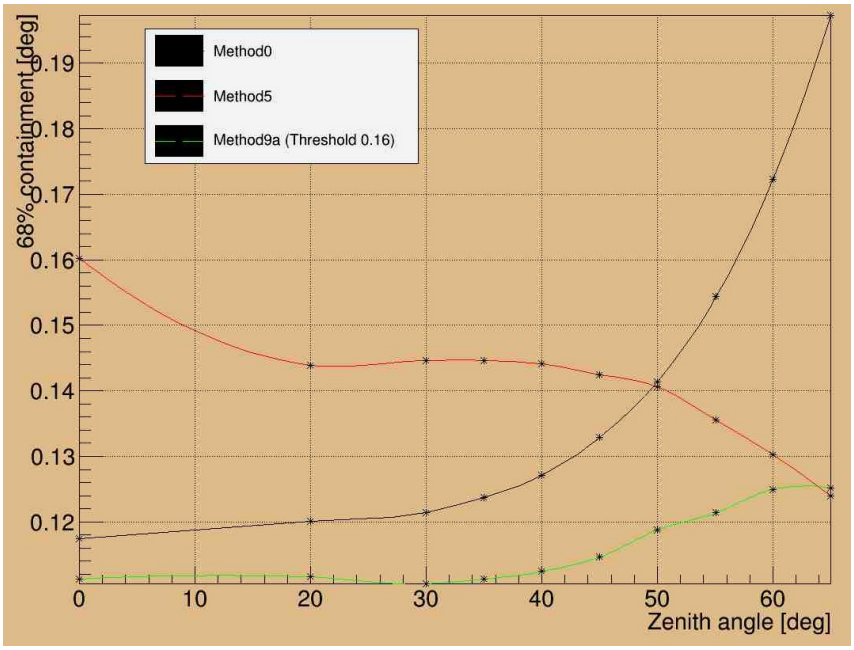


FIGURE 5.8: Angular resolution of one weight table parametrization and threshold (method9a), obtained with Monte Carlo simulation. This is compared to Disp and Geo, showing some improvement even at the smallest zenith angles.

own Disp method. The potential of a better performing Disp method at small zenith angles was very appealing, in light of encouraging results from the weight table even for the original Disp method. A weighted method that can rely on two strong moderately correlated methods can potentially deliver a very strong improvement.

Our new Disp method would rely on the Toolkit for Multivariate Data Analysis (TMVA), a package within ROOT that uses machine learning to perform multivariate analysis. It can be used as a replacement for the Disp *table*, and should outperform such a table given a similar amount of training data. It also provides a simpler and more standardized environment for training, testing, and using the results in analysis. Such an environment can be a big advantage for a future research project within VERITAS that may want to improve on our work.

To train a multivariate method, we begin by separating all Monte Carlo events image-by-image, and computing their true Disp, thus treating each telescope image as a separate event. We then ask TMVA to separate all events into two groups, one designated for testing and the other for training. After choosing some of the many multivariate techniques available (see Figure 5.9), TMVA uses the training data to build a Disp estimator for each technique that was selected. It tests the result on both the testing and training data; one should mostly consider the testing data when looking at the performance, but a discrepancy can be important for identifying overfitting, a known shortfall of some machine learning techniques.

We've also developed the necessary infrastructure in VEGAS to use the products of TMVA for each telescope, and the combine all Disp estimators of the separate images to reconstruct the position of an event. We began by simply averaging all telescope Disp estimators, but then noticed a very strong improvement when weighting the images by reliability. This weighting is achieved by training two more TMVA methods: a Disp error estimator, and major axis angle error estimator. The Disp error estimator relies on the Disp estimator; it uses the brightness of the image and its elongation to determine what is the likely error, in absolute value. Thus, the error itself cannot be used to improve Disp, but rather it is used to weight the results of high quality images over those of low quality ones.

We note that the final Disp table made use of the following parameters, all of which were discussed earlier: Width, Length, Size, Time Gradient (along the major axis), and Loss. It also makes use of the zenith and azimuth degrees of observation. The error estimators use similar parameters, but also rely on the value of the Disp estimator for the event.

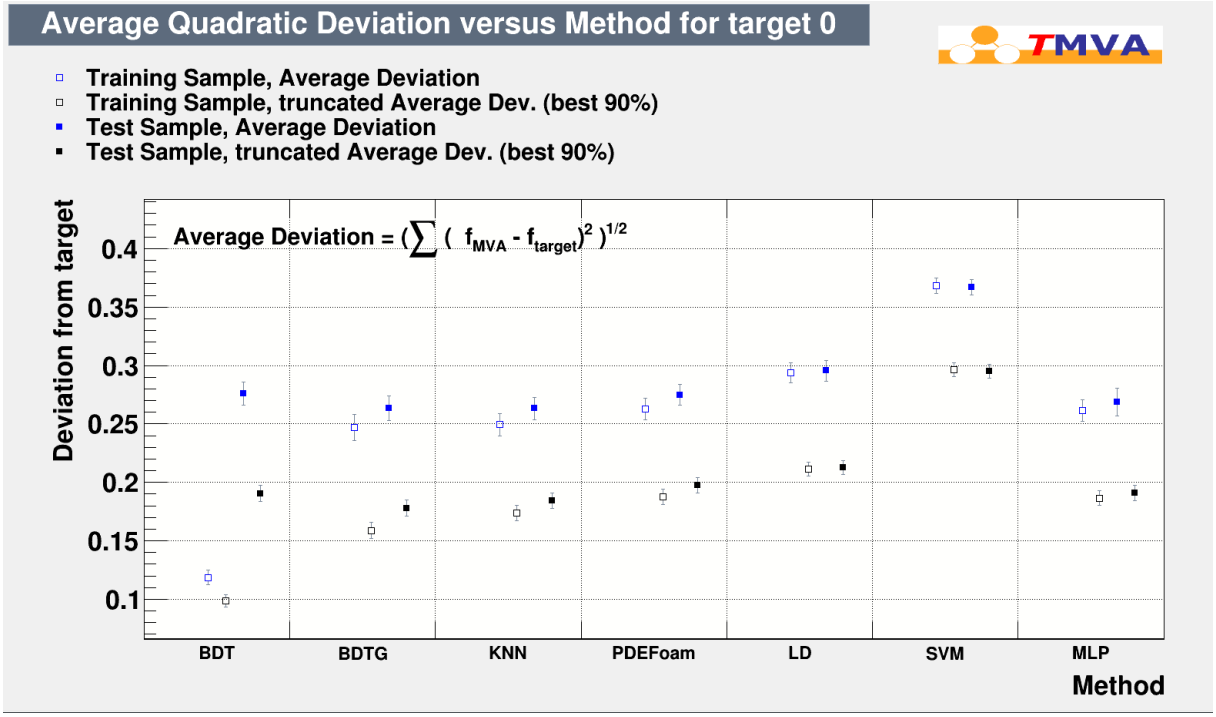


FIGURE 5.9: Comparison between different multivariate techniques available in TMVA (with relatively standard parameters). The best result we found was using Gradient Boosted Decision Trees. This has remained the best option even after more experimental testing, partially by a student collaborator (St Marie, 2014).

### 5.6.2 Correcting for a bias

It is typical to train the Disp estimator on Monte Carlo simulations that mimic events at a 0.5° distance from the center of the FOV. This practice is a result of the typical wobble observation, made at the same distance of 0.5° (for extended source observations this is often not the case).

An unexpected consequence of this type of training is that the Disp table, or TMVA estimator, can be biased and attempt to reconstruct events towards 0.5° off-center. We cannot rule out this possibility even for the simplest of Disp estimators (using only Size, Width and Length). As a possible example of this bias, the estimator might realize that a certain combination of

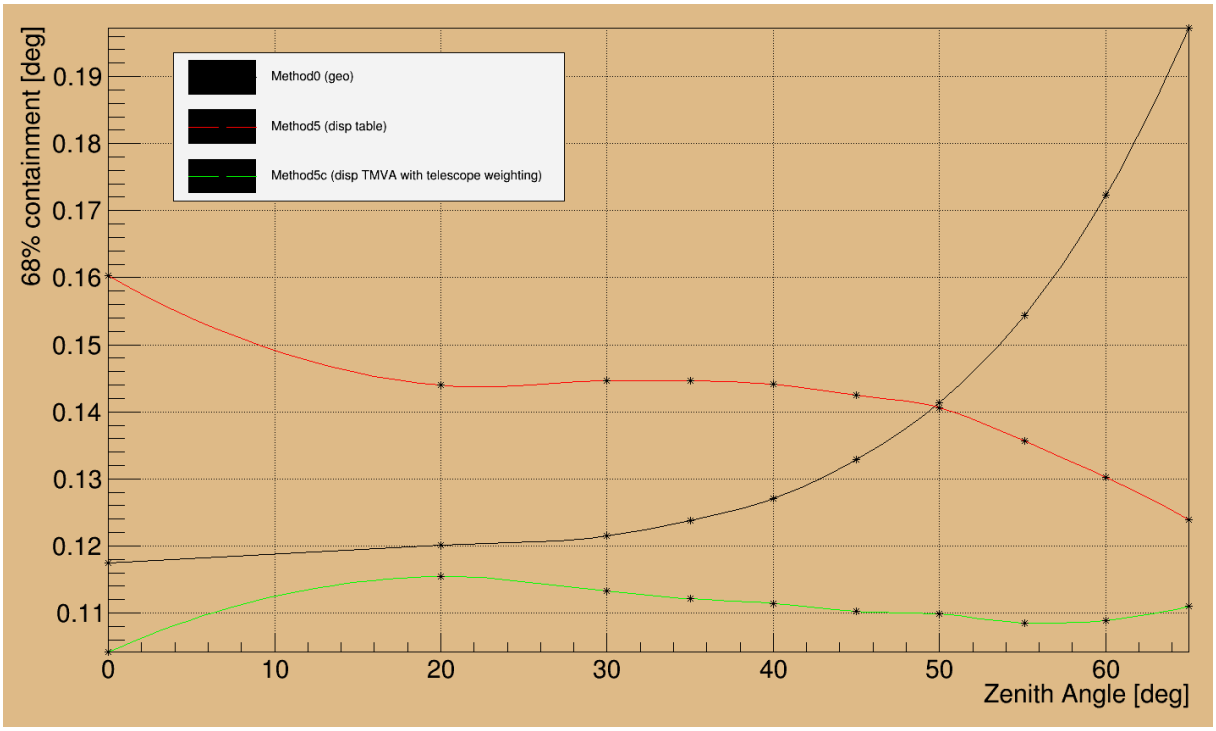


FIGURE 5.10: Angular resolution of the Disp method improves dramatically after implementing a telescope weighting based on image quality. It now performs well at small zenith angles in contrast to the Disp table.

parameters must indicate a truncated EAS image at the edge of the FOV and work backwards towards the "correct" off-center angle. In this case, the bias may not be immediately obvious, and could appear as a systematic issue at the highest energies only.

We have encountered this bias after completing the initial training of the Disp method and attempting to test the results on Crab Nebula data. Figure 5.11 shows a comparison of Disp and Geo acceptance curves, showing a clear excess at 0.5 degrees. The key to solving this issue is to realize that one must always train a Disp estimator on some distribution of events, and so it is likely impossible to always eliminate biases. However, by training on a smooth (and perhaps realistic) distribution of events in the field of view, one can achieve a method that is biased

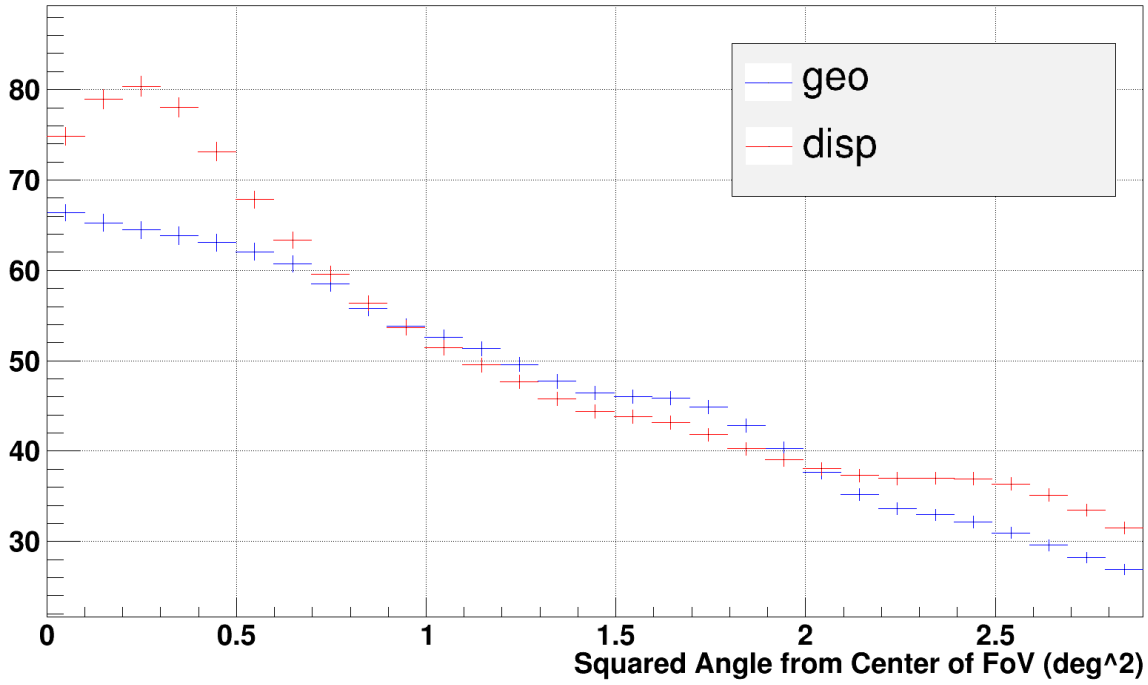


FIGURE 5.11: Plotting an acceptance curve for an analysis of 86 high quality Crab Nebula runs (with the source excluded). Both Geo and Disp are plotted. One can clearly see a bias in the Disp estimator, shifting reconstructed positions to 0.5° off-center.

in a smooth and controlled fashion. This type of bias can be handled properly using the ring background model (see Chapter 1 and Berge et al. (2007)), which may otherwise be unsuitable for "bumpy" features in the acceptance curve.

In Figure 5.12 we show this exact solution to our bias: we train the TMVA estimator on events that would form a reasonable and smooth acceptance curve. A full removal of the excess at 0.5° is only achieved after modifying the training on not just the Disp estimator, but also the error estimators (Disp and major-axis)–showing how remarkably capable machine learning can be at discovering patterns, and how careful one must be to avoid biases.

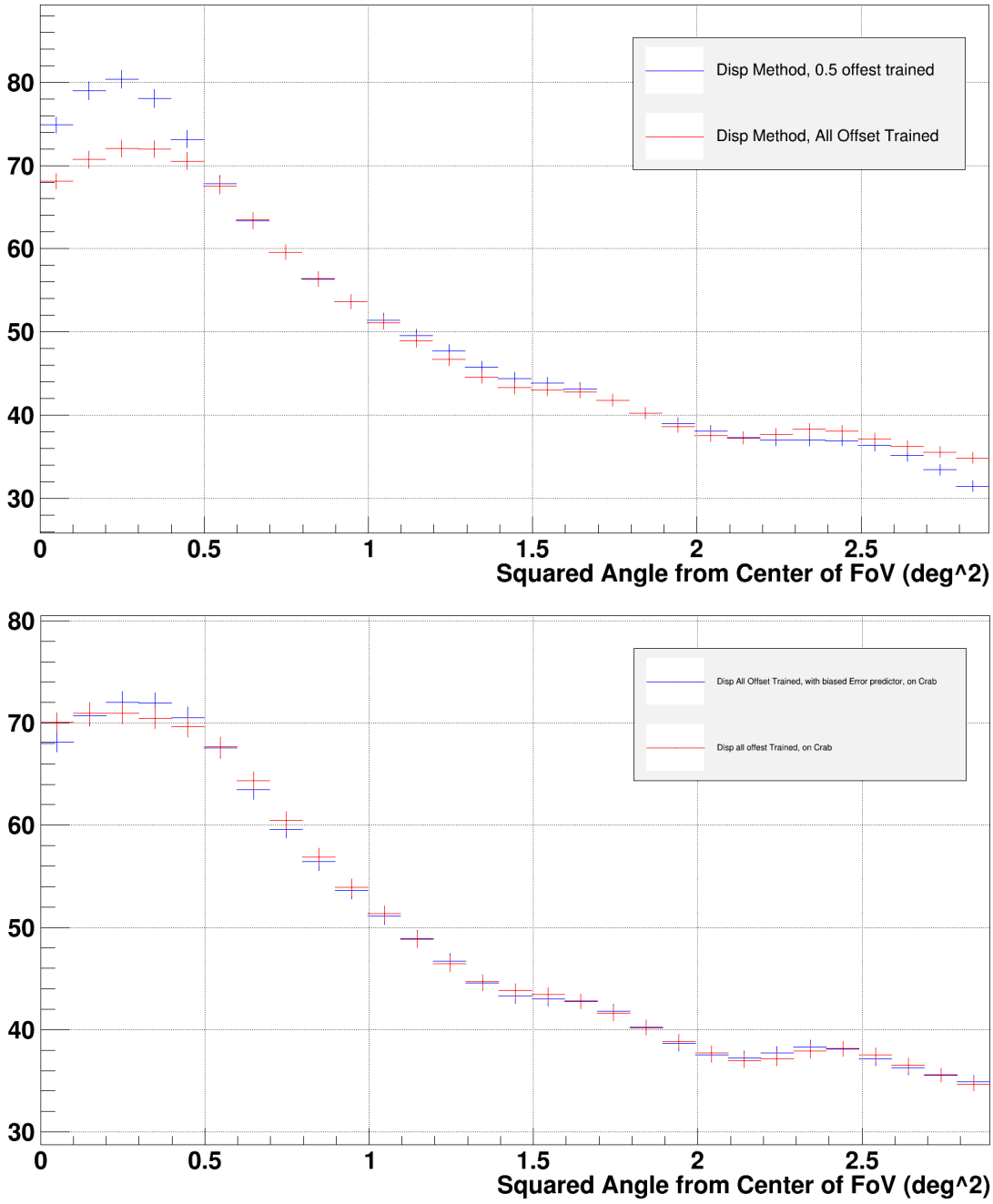


FIGURE 5.12: The bias shown previously can be corrected by training TMVA estimators on a smooth distribution of events. **Top:** we show the acceptance curve before and after modifying the Disp estimator training to an all-offset distribution. Remarkably, there still appears to be some small bias, likely due to the error estimators. **Bottom:** after modifying the error estimators to train on an all-offset distribution, the bias appears to be gone (within statistical uncertainty).

## 5.7 Another attempt at the weight tables

Given the improvement delivered by the new Disp method, especially at small zenith angles, we implemented a new weight table approach between Geo and this improved Disp method. For this iteration, we decided to use the TMVA tools rather than the original approach of a multidimensional table. This was decided due to similar reasons as with the Disp method; not only is TMVA likely to outperform a simple table, but it can be more easily replicated and modified.

The TMVA estimators required to implement a weight table:

- *Disp error:* as opposed to the estimator described in the last section, this does not refer to the expected error in the single-image Disp parameter, but rather the error in reconstruction of an event.
- *Geo error:* similar to the Disp error but for the geometrical method.
- *Covariance:* here we ask TMVA to estimate the error in Disp multiplied by the error in Geo, in either axis of the camera plane.

While the method shows significant improvement, it is clear that more trial and error in the parameter space could lead to further improvement. Given the upcoming development and testing of a new method of reconstruction that could replace Disp (based on simulation templates) (de Naurois and Rolland, 2009), we would like to see it combined with the Geometrical method–which we believe is still likely to perform better in many cases.

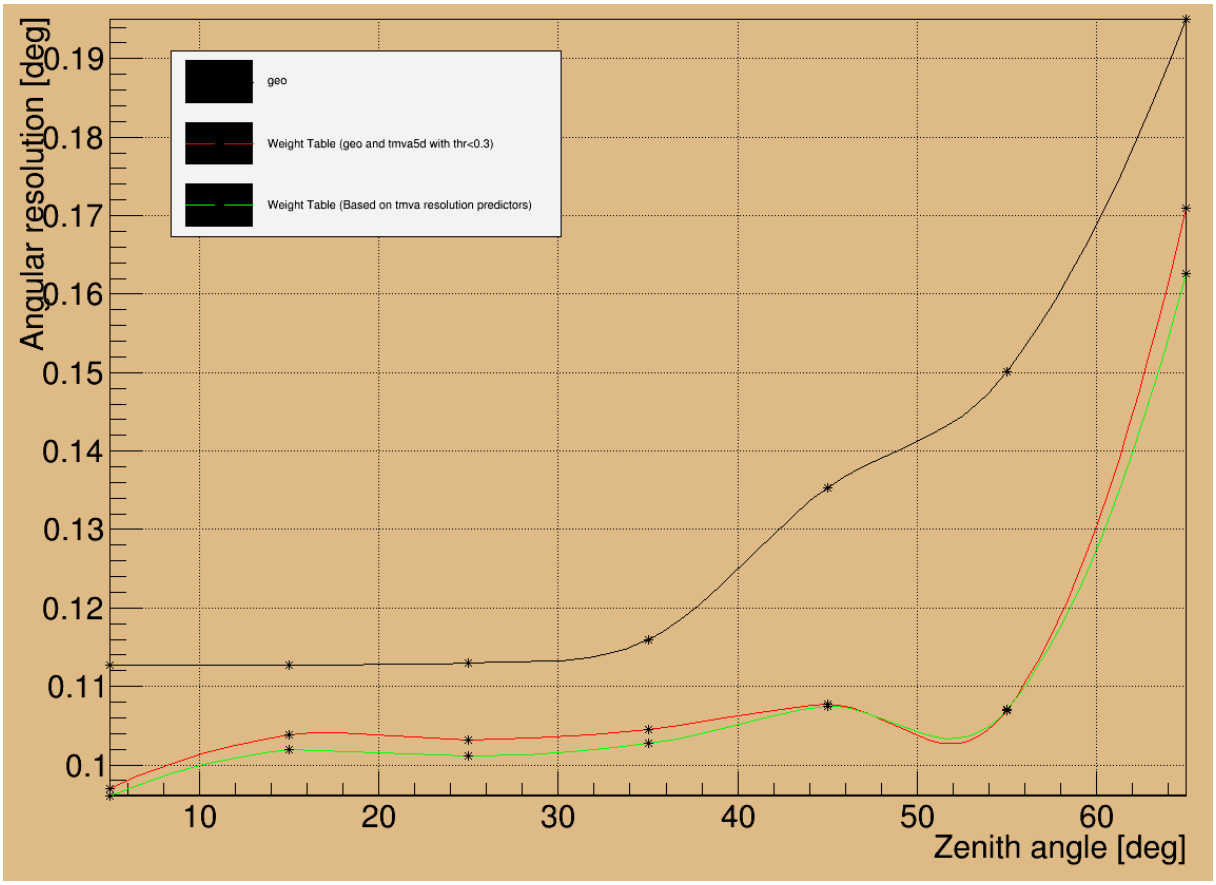


FIGURE 5.13: Angular resolution before and after changing the weight table to a TMVA approach, showing a small improvement, tested on 86 Crab Nebula runs (thanks to Nahee Park for selecting and processing those runs up to stage 2 of VEGAS). The plot is also compared to Geo.

### 5.7.1 Resolution prediction

In the process of weighting Disp and Geo, the weight table predicts the angular resolution available for each event. This can serve as powerful information, and a cut on this value could enhance analysis by, for example, separating nearby sources. One can also use this cut to attempt a higher signal purity for spectral studies.

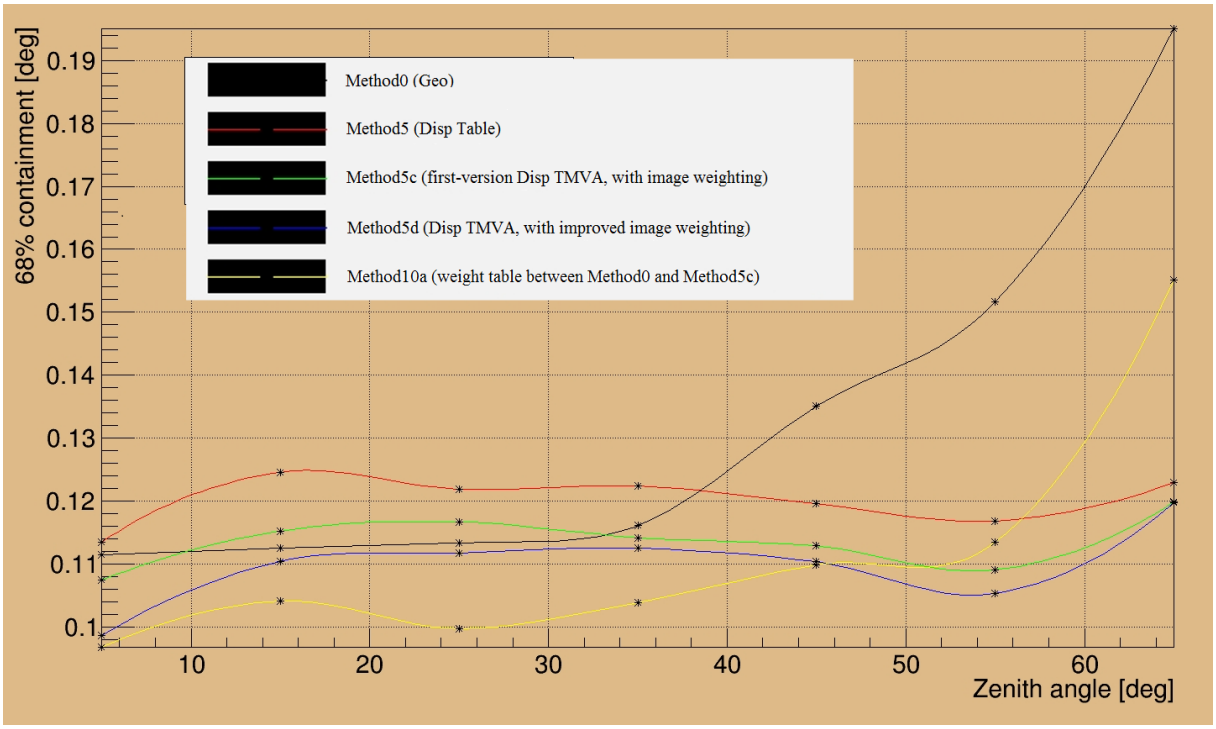


FIGURE 5.14: Angular resolution, tested on 86 Crab Nebula runs. The resolution of the weighted method represents an improvement of close to 10% at the smallest zenith angles (yellow). At the largest zenith angles, the Disp method may still be preferable, likely because the weighted method minimizes standard deviation rather than 68% containment.

Initial testing on the feasibility of such a cut showed a rule of thumb, that in order to halve the PSF radius, about 90% of the effective area needs to be sacrificed (this will also result in a reduction of background levels). More studies should be performed here, but we suspect bright extended sources could greatly benefit from this type of cut as well.

## 5.8 Conclusions

We described a new weighted method that aims to take advantage of two separate angular reconstruction techniques. Early results showed promise and a new Disp method was implemented to

further improve the performance at small zenith angles. The weight table method has resulted in about a 10% improvement in resolution even at the smallest zenith angles. It is possible that with a different choice of parameters this method can perform even better, and we encourage more experimentation in that domain.

# Chapter 6

# VERITAS observations of gamma-ray bursts: selecting and analyzing the most promising candidates for detection

Large parts of this chapter have been published in the 2015 International Cosmic Ray Conference (ICRC) proceedings (Weiner, 2015), where this work has been presented by the author. It has been reformatted and new content has been added, especially in relation to GRB 150323A.

## 6.1 Observing program and integration with GCN alerts

In the VERITAS observing program, gamma-ray bursts are considered the highest-priority sources. GCN alerts with a finer than 10° localization uncertainty radius are treated as a priority

and prompt the observers to slew immediately to any such burst that is above a 20° elevation.

VERITAS sensitivity is expected to be sufficient to detect strong bursts under reasonable assumptions about their high energy spectrum, as we've seen in § 2.4. For example, an extrapolation of LAT observations for GRB 130427A predicts an initial VERITAS flux of about 100 photons per second during the prompt phase (Aliu et al., 2014), while, for comparison, the background rate for a region the size of the point-spread-function (PSF) is on the order of 1 count per minute. At the night of GRB 130427A, VERITAS was not operating due to a full moon; however, according to the estimates, a detection of the burst would have been achieved in less than a second. Observations started the following night, and results yielded a small positive significance of 1.3 for the first night, and 1.1 for the second night (Aliu et al., 2014). There are also theoretical reasons to anticipate VHE emission during both the prompt and afterglow phases, as we've seen in § 2.6.

As of the time this analysis has been conducted (June 2015), VERITAS had observed 132 gamma-ray burst locations.[1] Of these observations, we attempted to analyze the most promising candidates for detection based on a reasonable *a priori* measure.

## 6.2 Selecting the most promising candidates for detection

The most important factors in our ability to detect a burst are the observing delay, redshift (z), and elevation angle at the time of observing. The elevation angle is particularly important for high redshift bursts, since the instrument's energy threshold rapidly increases with decreasing

[1] VERITAS has added some observations since. We haven't updated this analysis to reflect those additional observations.

elevation angle, whereas absorption of gamma-rays due to the extragalactic background light (EBL) favours a very soft spectrum. We also required the burst to have been localized as well as our angular resolution or better ($\sim 0.1^{\circ}$). Bursts with unknown redshift were left out of the analysis, considering the high z typically associated with them.

We calculated the following weight for each burst that met the conditions above: $W = e^{-\tau(z,E_{th}(\theta))}/t_{obs}$, where $\tau$ is the optical depth[2] due to EBL absorption at the threshold energy, which depends on the elevation angle of observation $\theta$, and $t_{obs}$ is the observing delay. One can recognize this expression to be approximately proportional to the incoming VHE flux at the initial time of observing, assuming the flux decays as $1/t$, as is more or less typical for Fermi-LAT observed bursts (Ackermann et al., 2013).

One significant factor that is missing from our weighting expression is the luminosity distance, which would account for the geometric factor that favors nearby bursts, approximately $1/R^2$ at nearby distances. We choose to ignore this factor to correct for selection biases of satellites. Nearby bursts are more likely to be fainter as they are easily detectable by X-ray instruments. The other factors in our weighting expression do not affect the ability of any space observatory to detect a burst, as X-rays are insensitive to EBL absorption as well as to our zenith angle of observation.

We've calculated the weighting factors for all relevant bursts. The most promising observation was found to be that of GRB 150323A. We analyzed other bursts with weights within a factor of about 100 of its weight, to account for possible intrinsic variance in the VHE emission of the bursts. We found 7 other observations that met our criteria (see Table 6.1).

[2]We obtained this value using the method described in Finke et al. (2010).

The bursts were analysed using a standard VERITAS analysis package, as described in Chapter 1. Cuts optimized for soft spectrum sources were used in the analysis (when considering EBL absorption, even nearby bursts are likely to have a soft spectrum at Earth in the VHE energy range). The VHE flux was assumed to decay as a power law with an index of $-1$, beginning at the prompt phase of emission. The results for each of the 8 bursts is described in Table 6.1. No individual burst was detected at a 5-sigma level.

| Name of Burst | Significance |
|---|---|
| GRB 111225A | -0.7 |
| GRB 120422A | 2.5 |
| GRB 130215A | -0.6 |
| GRB 130427A | 1.7 |
| GRB 130604A | -0.7 |
| GRB 140622A | -1.3 |
| GRB 150120A | -0.5 |
| GRB 150323A | -1.5 |

TABLE 6.1: Time-dependent likelihood significance of 8 selected VERITAS bursts.

## 6.3 Stacking analysis: abandoning the Kolmogorov-Smirnov test statistic in favor of a binomial test

A standard way to search for a weak signal present in multiple observation is by use of the Kolmogorov-Smirnov test statistic (e.g., Acciari et al. (2011)). Known in short as the KS test, it works by examining the largest difference between a theoretically expected cumulative distribution function (CDF) and an observed, empirical cumulative distribution function (ECDF) (e.g. Stephens (1974)). An ECDF is produced for N independent, identically distributed samples. Given the number of samples, N, and the largest difference found between the CDFs, one can determine the likelihood of this distance or greater arising under the null hypothesis; that is, if the ECDF is indeed

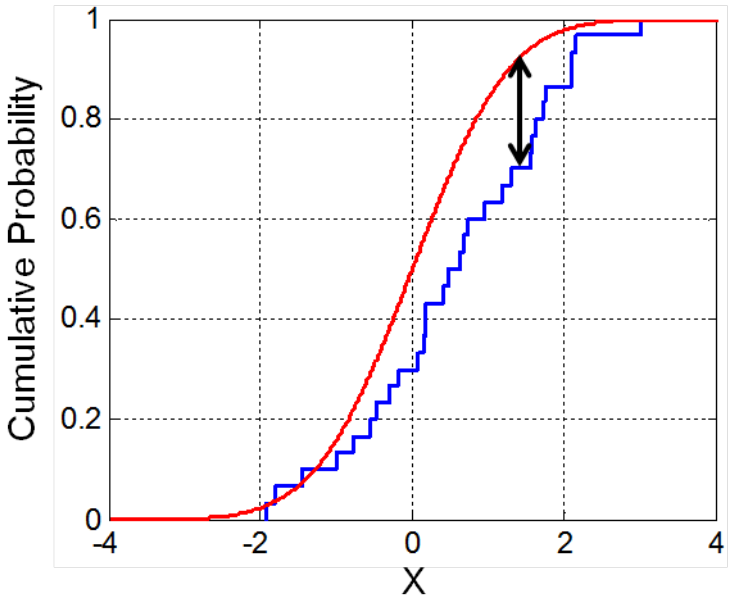


FIGURE 6.1: Illustration of the Kolmogorov-Smirnov test statistic. The red curve is the theoretical CDF, and the blue curve represents the empirical CDF (ECDF). The largest difference between the curves is found across all X values and denoted by a black arrow. The length of this arrow is the test statistic. Taken from https://en.wikipedia.org/wiki/Kolmogorov-Smirnov_test.

derived from the theoretical CDF. This largest difference between the curves is illustrated in Figure 6.1. The null probability is also known as a p-value, which may then be converted into a standard Gaussian significance.

Usually, a cumulative distribution of the significance of all observations is plotted (ECDF), and is compared to the theoretical prediction in the absence of a signal, given by Wilks' theorem. We believe this test has some substantial weaknesses with respect to our type of analysis and the kind of signal we are looking for:

- **Non specificity:** When the KS test statistic finds a significant p-value, the interpretation is highly non-specific. For example, one can consider whether Wilks' theorem is applicable in the limit of low statistics or in the presence of systematics (we have discussed some

examples in Chapter 4). The KS test will eventually discover even small inaccuracies in the theoretical CDF, without an ability to point to whether the "signal" came from such inaccuracies, or what those inaccuracies are.

- **Insensitivity to certain types of signal:** The KS test is sensitive to difference in cumulative probabilities, and thus only indirectly to rare occurrences. Suppose that out of 50 observations, two bursts were discovered at a significance only slightly under 5-sigma, and the rest follow a Wilks' theorem distribution. There is little assurance that the KS test will detect this kind of signal. Indeed, this kind of signal may be exactly what we are looking for, since we suspect some of our GRB observations may have been too late to detect VHE emission, or at a redshift to large to be seen.

- **Lack of control:** There are no free parameters in the KS test that allow us to control what we are searching for, whether we are expecting a few bright bursts, many faint bursts, or both.

- **Handling possible CDF uncertainties:** There is no clear way to handle possible uncertainties in the theoretical CDF. For example, suppose one were to widen the Wilks' theorem distribution, in order to make a "conservative" estimation of a p-value. If the true CDF is narrower than the widened CDF, the KS test will clearly detect this discrepancy as a signal over a sufficient number of observations. In other words, the KS test will only accept an exact theoretical CDF, no more or less, without room for a conservative estimation of any kind.

We devise a simple test that we believe addresses all issues above, a binomial test. It is performed as follows: Each burst is analyzed and its significance is found. A threshold significance

is decided prior to analysis, and each burst can pass a test by having a greater significance than this decided threshold, or otherwise fail the test. A p-value is calculated given the number of bursts that passed the test compared to what would be expected if their significance values followed a unit Gaussian distribution, as one would expect from the null hypothesis (Wilks' theorem).

The p-value is calculated with the following formula and then converted to Gaussian significance:

$$P = \sum_{n=l}^{N} \left( \Phi^n(s)(1-\Phi(s))^{N-n} \binom{n}{N} \right) \tag{6.1}$$

where $l$ is the number of bursts passing the test, $N$ is the total number of bursts in the analysis, and $\Phi(s)$ is defined here as the one-sided probability of obtaining a result with Gaussian significance greater than $s$: $\Phi(s) = \int_s^\infty dx \frac{1}{\sqrt{2\pi}} e^{-\frac{x^2}{2}}$. Note how one can increase the variance of this Gaussian for a conservative estimation, something which was not feasible for the KS test.

The binomial test p-value may also be multiplied by the number of trials. In this analysis, we accounted for 10 trials while using only 3 of them (see Table 6.2). The reason for this is that we are anticipating more trials on a wider selection of bursts without a known redshift.

The threshold significance values were carefully selected using a computer script, to make sure that a whole number of bursts will be required to give an exact 5-sigma result. This resulted in fractional values for the thresholds, to a precision of 3 decimal digits. Table 6.2 summarizes our test selection[3] (thresholds are calculated using a trials factor of 10). Table 6.2 describes the final p-value of all 3 binomial trials.

[3] This selection was made prior to analysis of the bursts and the results found in Table 6.1.

| Threshold significance | Minimal number of bursts needed to achieve detection | Number of bursts passing test | p-value |
|---|---|---|---|
| 1.852 | 6 out of 8 | 1 out of 8 | 0.23 |
| 2.611 | 4 out of 8 | 0 out of 8 | 1 |
| 3.998 | 2 out of 8 | 0 out of 8 | 1 |

TABLE 6.2: Description and results of all binomial tests.

## 6.4 GRB 150323A

### 6.4.1 VERITAS observation and upper limit

The results on the VERITAS analysis of this burst are detailed in VERITAS Collaboration (2017), a paper we are writing in collaboration with the group that developed the model we described in § 2.6. Here we will summarize the observation and results.

On March 23rd 2015, 02:49:14 UT, the Swift Burst Alert Telescope (BAT) triggered on a burst with a J2000 position of (128.191, +45.434) and an error radius of approximately 3 arcminutes (Amaral-Rogers et al., 2015). This error radius is both smaller than the VERITAS gamma-ray point spread function ($\sim$0.1 degrees) and the VERITAS field of view ($\sim$3.5 degrees). This position was later refined with Swift X-ray telescope (XRT) measurements to an accuracy of a few arcseconds (Goad et al., 2015). The optical afterglow was detected by the Low Resolution Imaging Spectrometer (LRIS) on the Keck I 10m telescope. Several absorption and emission lines uniformly indicated the redshift of this burst to be of $z = 0.593$ (Perley and Cenko, 2015).

VERITAS began observing the burst 270 seconds after the Swift trigger. The elevation of the source was 73 degrees at that time, and slowly rising. The observations lasted for a few hours.

We first used our test statistic for time-varying sources, with the assumption of a $1/t$ light curve; There was no detection, as seen in Table 6.1.

Upper limits are more straightforward to produce with the Li & Ma test statistic, especially since they do not rely on assumptions about the shape of the light curve. However, one must be careful to choose a sensible integration time, which should not be too large, as we've seen in Chapter 4. Our simulations indicate for the assumption of $1/t$ light curve, a 270 second delay-time, and a burst on the threshold of detection, the ideal integration time is about 40 minutes (there is no need to be too precise here, as we do not know the exact light curve and amplitude of emission). As expected, the Li & Ma test statistic did not show a detection. We found the differential upper limit at 138 GeV is $3.05 \times 10^{-6}$ TeV$^{-1}$ m$^{-2}$ s$^{-1}$, and the integral upper limit at 138 GeV to 30 TeV is $1.29 \times 10^{-7}$ m$^{-2}$ s$^{-1}$. This upper limit assumes an intrinsic photon counting power law index of $-2$, and overlays extragalactic background light (EBL) absorption based on the model described in Finke et al. (2010).

Alternatively, the 99% upper limit can be given as 16.5 photons during the first 40 minutes of VERITAS observation. This is a more natural way to quote an upper limit, as it does not require any assumptions on the spectral shape of emission.

The Swift-BAT light curve, seen in Figure 6.2, places GRB 150323A into the "precursor" category, where most of the emission is produced tens to hundreds of seconds after a weak trigger event. These types of bursts can account for as few as 3% to as many as 20% of all bursts depending on the criteria used to define them (Burlon et al., 2008). The light curve of GRB 150323A consists of one minor peak which triggered the observation, and a larger secondary peak about 135 seconds after the trigger. The VERITAS telescopes were on target 270 seconds after the BAT trigger at 02:53:44 UT, which corresponds to a 135 second delay

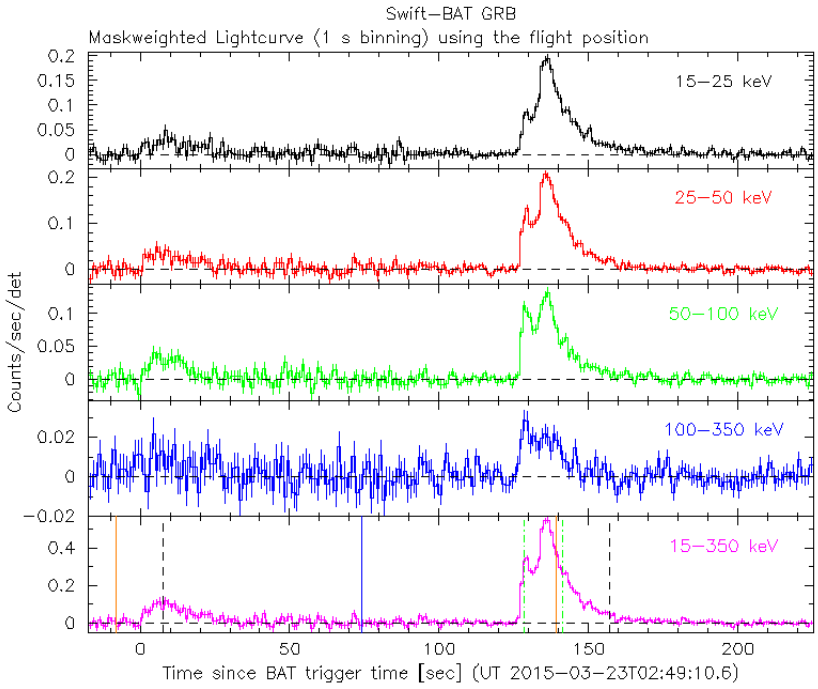


FIGURE 6.2: The Swift-BAT lightcurve for GRB 150323A, showing both the precursor and the main emission period. The different coloured plots correspond to various energy bands observed by BAT as indicated in each subplot. Taken from the batgrbproduct analysis page: http://gcn.gsfc.nasa.gov/notices_s/635887/BA/.

compared to the main BAT peak. While the VERITAS observation is delayed relative to the prompt (BAT) emission, we stress that GeV observations by LAT consistently indicate a more temporally extended emission at higher photon energies (Ackermann et al., 2013). If this result extends to the VERITAS energy band, one would expect strong VHE emission, detectable by VERITAS at the time of observing. Note that GRB 150323A was not in the LAT field of view within an hour of the Swift-BAT trigger.

### 6.4.2 Empirically driven extrapolation

Historically, the energy emitted in the GeV band by LAT-detected bursts clusters around 10% of the prompt energy detected by GBM (Ackermann et al., 2013). Assuming that comparable energy is emitted at higher frequencies, we calculated the expected fluence in the VERITAS band and compared it to the experimental upper limit. We have assumed that:

1) VHE emission begins suddenly and decays as $1/t$.[4]

2) The fluence emitted in the VERITAS energy band is given by 10% of the prompt fluence detected by the BAT.

3) EBL absorption follows the model by Finke (Finke et al., 2010).

4) We approximate the VERITAS effective area as uniform, while in reality it is very slightly changing during the observation.

Of these assumptions, we believe (2) is the most dependent on GRB-environment and theory. Assumption (1) has been established by LAT data as a good approximation,[5] (3) is in fact considered stringent in light of recent results (Abeysekara et al., 2015) and assumption number (4) is a very good approximation used for simplification purposes.

Our resulting ratios are greater than 1 (see Table 6.3), indicating that the VHE emission must be weaker than expected by extrapolation.

[4] We have the emission suddenly end after 1 day, consistent with the typical length of a LAT observation.

[5] LAT results show that in the GeV band, afterglow fluence is comparable to prompt fluence, and decays approximately as $1/t$ (Ackermann et al., 2013).

| | Emission begins at trigger[a] | Emission begins at $t = 135s$ |
|---|---|---|
| Origin time at trigger | 1.4 | 2.5 |
| Origin time at $t = 135s$ | n/a | 2.1 |

[a] With a 1-sec delay, consistent with LAT observations of prompt emission delay

TABLE 6.3: Ratio of the model fluence to the VERITAS upper-limit under different assumptions. The origin time corresponds to $t = 0$ in the $1/t$ time-decay. As an example, an origin time of 135s could correspond to a burst that was independent of the triggering emission. The emission start time corresponds to the fluence budget of TeV radiation under assumption (2).

### 6.4.3 Constraints on the GRB environment

As we discussed in § 2.6, an upper limit can be used to put constraints on the GRB environment. This relatively nearby burst had an energy output that would far exceed our upper limit of 16.5 photons, even if only 10% was emitted in VHE gamma-rays (VERITAS Collaboration, 2017). We thus arrive at the following conclusion:

For the wind medium, the maximum IC energy must have been below the VERITAS energy threshold of 138 GeV, which implies the condition

$$\frac{E_{kin}/(10^{52}\,\mathrm{erg})}{A/(10^{11}\,\mathrm{g/cm})} < 0.36. \tag{6.2}$$

The condition above is found by requiring the IC cutoff in Equation 2.3 to be below the energy threshold, while taking the pair-loading to be unity–which results in a condition on the Lorentz factor. Then, using $R_{load}$ found in Equation 2.4, we extract the condition on the enviroment from

Equation 2.5–which describes the Lorentz factor at the time the pair-loading becomes small as a function of the kinetic energy and ambient wind density.

Using the standard parameters of $E_{kin} = E_{GRB}$ and $A = 3 \times 10^{11}$ g/cm, this condition is satisfied, but barely. For a particularly dense wind, this condition would be more easily satisfied.

For the ISM, it is difficult to constrain the environment. The relatively faint X-ray afterglow would not have been sufficient to cause efficient cooling (VERITAS Collaboration, 2017), and thus it is possible that VHE emission was too faint to be seen, regardless of the density of the CBM or kinetic energy associated with the burst.

### 6.4.4 Summary

GRB 150323A was observed by VERITAS promptly and under fortunate observing conditions. At a redshift of about 0.6, it does not suffer from much EBL attenuation, especially at the lowest VHE energies. In addition, the high elevation and good weather conditions have made this burst observation an excellent target for theoretical analysis. While we did not detect the burst, our observations produced a strong upper limit which we interpreted theoretically using the model described in § 2.6.

The Wolf-Rayet wind medium has been generally found to be consistent with Fermi-LAT results (Hascoët et al., 2015). The constraint we derived from the VERITAS upper limit in Equation 6.2 is therefore significant. While it does not violate the model we use to understand the afterglow emission, it significantly constrains the wind density and kinetic energy of the burst (as we've seen, for standard parameters the condition in the equation is only marginally satisfied). In the future, more IACT observations under the same conditions (redshift, elevation, time-delay)

are expected to eventually lead to a VHE detection; in the absence of such a detection our understanding of afterglow physics would have to be questioned. Thus this result and similar observations in the future will undoubtedly further our understanding of gamma-ray bursts, and in particular their afterglow physics.

# Future prospects

To date, gamma-ray bursts have not been detected at very high energies of above 100 GeV, in spite of a significant number of observations by multiple instruments, among them 159 observation by VERITAS. As part of this work an improved and collective analysis of the most promising VERITAS burst observations has resulted in a non-detection, continuing to favor lower levels of emission at the highest energies. As discussed in Chapter 2, this could indicate a high-density CBM in the Wolf-Rayet population of progenitors, or a typically low kinetic energy budget for the GRB ejecta.

We remain optimistic about future prospects for detection. In Chapter 3, we derived a test statistic for transient source detection, increasing the sensitivity appreciably, as shown in Chapter 4. We've also implemented some improvements in angular reconstruction which can be used to increase sensitivity at all zenith angles of observation. The Disp method is now more robust, allowing it to used for large zenith observations without biases, crucial for GRB detection since most observations are at such angles and often have large uncertainty in their position.

All of the technical improvements we described in this work can be used by current and future generation IACT arrays. Additionally, the test statistic for transient source detection could be used by other gamma-ray instruments such as HAWC, which observes most of the sky at all

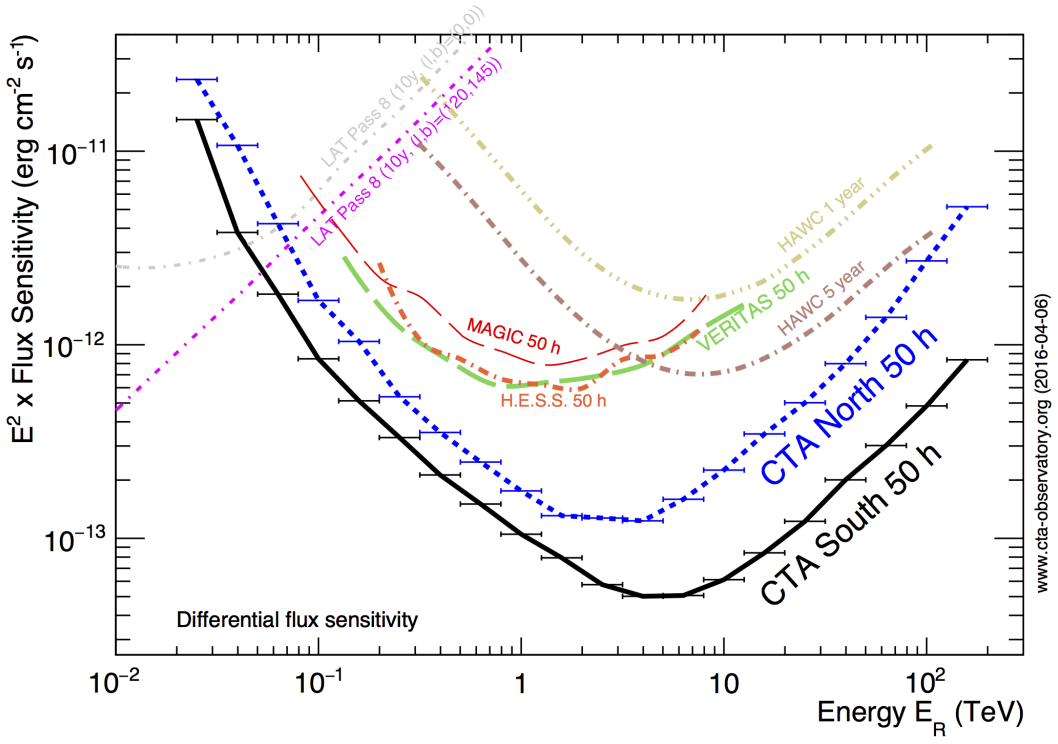


FIGURE 6.3: CTA will bring a great improvement in sensitivity in comparison to current-generation IACT arrays. This fact combined with a lower energy threshold and other improvements, will drastically increase our ability to detect and study gamma-ray bursts. Fermi-LAT will still be of vital importance due to its large sky coverage and sensitivity at 10s of GeV and below. From the official CTA webpage: https://www.cta-observatory.org/science/cta-performance/.

times and therefore has many bursts in its field of view; the non-existent delay time in such cases will likely make the test statistic we derived even more important for such observations.

An ideal scenario for studying the physics of bursts and their afterglows would be a simultaneous detection with an IACT array and Fermi-LAT. Even an IACT non-detection in the presence of bright LAT-detected emission can be very significant. LAT data can be used to find the parameters associated with the explosion and provide a definitive prediction for VHE emission in the afterglow which can then be tested independently.

The prospects for such a simultaneous detection will increase significantly with the operation of CTA, the next generation IACT array–which will in fact be composed of two separate arrays, in the Southern and Northern hemispheres (Actis et al., 2011). Any one CTA array have a sensitivity that is about an order of magnitude greater than that of current generation arrays (see Figure 6.3). It will also have a lower energy threshold at about 20 GeV, thus probing deeper into the universe by partially escaping the the impact of EBL scattering. Moreover, the larger field of view and number of telescopes, about 30 for the North and 100 for the South, allow good coverage of the nearby sky the case of a GCN alert with poor localization. This seems all but certain to guarantee interesting results that will shed light on the nature of gamma-ray bursts and their interaction with the environment surrounding the explosion.

# Bibliography


Abdo, A. A., Ackermann, M., Ajello, M., et al. (2009). A Limit on the Variation of the Speed of Light Arising From Quantum Gravity Effects. *Nature*, 462(7271):331–334.

Abdo, A. A., Allen, B. T., Berley, D., et al. (2007). Milagro Constraints on Very High Energy Emission from Short-duration Gamma-ray Bursts. *The Astrophysical Journal*, 666(1):361–367.

Abeysekara, A. U., Archambault, S., Archer, A., et al. (2015). Gamma-Rays from the Quasar PKS 1441+25: Story of an Escape. *The Astrophysical Journal Letters, Volume 815, Issue 2, article id. L22, 7 pp. (2015).*, 815.

Acciari, V. A., Aliu, E., Arlen, T., et al. (2011). VERITAS Observations of Gamma-ray Bursts Detected by Swift. *The Astrophysical Journal*, 743(1):62.

Acciari, V. A., Arlen, T., Aune, T., et al. (2010). VERITAS Search for VHE Gamma-ray Emission From Dwarf Spheroidal Galaxies. *The Astrophysical Journal*, 720(2):1174–1180.

Ackermann, M., Ajello, M., Asano, K., et al. (2013). The First Fermi-LAT Gamma-Ray Burst Catalog. *The Astrophysical Journal Supplement Series*, 209(1):11.

Actis, M., Agnetta, G., Aharonian, F., et al. (2011). Design Concepts for the Cherenkov Telescope Array CTA: an Advanced Facility for Ground-based High-energy Gamma-ray Astronomy. *Experimental Astronomy*, 32(3):193–316.

Aharonian, F., Buckley, J., Kifune, T., et al. (2008). High Energy Astrophysics With Ground-based Gamma Ray Detectors. *Reports on Progress in Physics*, 71(9):096901.

Aliu, E., Aune, T., Barnacka, A., et al. (2014). Constraints on Very High Energy Emission From GRB 130427A. *The Astrophysical Journal*, 795(1):L3.

Amaral-Rogers, A., Barthelmy, S. D., Marshall, F. E., et al. (2015). GRB 150323A: Swift Detection of a Burst. *GCN Circular 17611*.

Amelino-Camelia, G., Ellis, J., Mavromatos, N. E., Nanopoulos, D. V., and Sarkar, S. (1998). Tests of Quantum Gravity From Observations of Gamma-ray Bursts. *Nature*, 393(6687):763–765.

Antcheva, I., Ballintijn, M., Bellenot, B., et al. (2015). ROOT - A C++ Framework for Petabyte Data Storage, Statistical Analysis and Visualization.

Arlen, T., Aune, T., Beilicke, M., et al. (2013). Rapid TeV Gamma-ray Flaring of BL Lacertae. *The Astrophysical Journal*, 762(2):92.

Atkins, R., Benbow, W., Berley, D., et al. (2004). Limits on Very High Energy Emission from Gamma-Ray Bursts with the Milagro Observatory. *The Astrophysical Journal*, 604(1):L25–L28.

Atwood, W. B., Abdo, A. A., Ackermann, M., et al. (2009). The Large Area Telescope on the Fermi Gamma-ray Space Telescope Mission. *The Astrophysical Journal*, 697(2):1071–1102.

Barthelmy, S. D. (2000). GRB Coordinates Network (GCN): A Status Report. In *AIP Conference Proceedings*, volume 526, pages 731–735. AIP.

Beilicke, M. (2010). Shower Reconstruction at Large Zenith Angles (LZA).

Beloborodov, A. M. (2002). Radiation Front Sweeping the Ambient Medium of Gamma-ray Bursts. *The Astrophysical Journal*, 565(2):808–828.

Beloborodov, A. M., Hascoët, R., and Vurm, I. (2014). On the Origin of GeV Emission in Gamma-ray Bursts. *The Astrophysical Journal*, 788(1):36.

Berge, D., Funk, S., and Hinton, J. (2007). Background Modelling in Very-high-energy $\gamma$-rayAstronomy. *Astronomy and Astrophysics*, 466(3):1219–1229.

Blackett, P. (1948). Physical Society Gassiot Committee Report. page 34.

Blandford, R. D. and McKee, C. F. (1976). Fluid Dynamics of Relativistic Blast Waves. *Physics of Fluids*, 19(8):1130–1138.

Bretz, T., Anderhub, H., Backes, M., et al. (2013). FACT - The First G-APD Cherenkov Telescope: Status and Results.

Bromberg, O., Nakar, E., Piran, T., et al. (2012). An Observational Imprint of the Collapsar Model of Long Gamma-ray Bursts. *The Astrophysical Journal*, 749(2):110.

Burlon, D., Ghirlanda, G., Ghisellini, G., et al. (2008). Precursors in Swift Gamma Ray Bursts with Redshift. *The Astrophysical Journal*, 685(1):L19.

Cherenkov, P. A. (1934). Visible Emission of Clean Liquids by Action of Gamma Radiation. *Doklady Akademii Nauk SSSR*, 2:451+.

Cogan, P. (2006). *Nanosecond Sampling of Atmospheric Cherenkov Radiation Applied to TeV Gamma-Ray Observations of Blazars with VERITAS*. PhD thesis.

Cogan, P. (2007). VEGAS, the VERITAS Gamma-ray Analysis Suite.

Cortina, J., Goebel, F., and Schweizer, T. (2009). Technical Performance of the MAGIC Telescopes.

Coward, D., Howell, E., Branchesi, M., et al. (2012). The Swift Gamma-ray Burst Redshift Distribution: Selection Biases and Optical Brightness Evolution at High-z?

Cronin, J. W. (1999). Cosmic Rays: the Most Energetic Particles in the Universe. *Reviews of Modern Physics*, 71(2):S165–S172.

Davies, J. M. and Cotton, E. S. (1957). Design of the Quartermaster Solar Furnace. *Solar Energy*, 1:16–22.

Davies, M. B., Levan, A. J., Larsson, J., King, A. R., and Fruchter, A. S. (2007). Progenitors of Long Gamma-ray Bursts.

de Naurois, M. and Rolland, L. (2009). A High Performance Likelihood Reconstruction of Gamma-rays for Imaging Atmospheric Cherenkov Telescopes.

DeYoung, T. (2012). The HAWC Observatory. *Nuclear Instruments and Methods in Physics Research Section A: Accelerators, Spectrometers, Detectors and Associated Equipment*, 692:72–76.

Feldman, G. J. and Cousins, R. D. (1998). Unified Approach to the Classical Statistical Analysis of Small Signals. *Physical Review D*, 57(7):3873–3889.

Fermi, E. (1949). On the Origin of the Cosmic Radiation. *Physical Review*, 75(8):1169–1174.

Fiasson, A., Dubois, F., Lamanna, G., Masbou, J., and Rosier-Lees, S. (2010). Optimization of Multivariate Analysis for IACT Stereoscopic Systems. *Astroparticle Physics*, 34(1):25–32.

Finke, J. D., Razzaque, S., and Dermer, C. D. (2010). Modeling the Extragalactic Background Light From Stars and Dust. *The Astrophysical Journal*, 712(1):238–249.

Gal-Yam, A., Fox, D. B., Price, P. A., et al. (2006). A Novel Explosive Process Is Required for the $\gamma$-ray Burst GRB 060614. *Nature*, 444(7122):1053–1055.

Galama, T. J., Vreeswijk, P. M., van Paradijs, J., et al. (1998). An Unusual Supernova in the Error Box of the Gamma-ray Burst of 25 April 1998. *Nature*, 395(6703):670–672.

Galante, N. (2012). Status and highlights of VERITAS. *AIP Conference Proceedings*, 1505:202–208.

Galbraith, W. and Jelley, J. V. (1953). Light Pulses from the Night Sky Associated with Cosmic Rays. *Nature*, 171(4347):349–350.

Gehrels, N., Chincarini, G., Giommi, P., et al. (2004). The Swift Gamma-ray Burst Mission. *The Astrophysical Journal*, 611(2):1005–1020.

Gehrels, N., Sarazin, C. L., O'Brien, P. T., et al. (2005). A Short Gamma-ray Burst Apparently Associated With an Elliptical Galaxy at Redshift z = 0.225. *Nature*, 437(7060):851–854.

Gieseler, U. D. J. and Jones, T. W. (2000). First Order Fermi Acceleration at Multiple Oblique Shocks. *Astronomy and Astrophysics, v.357, p.1133-1136 (2000)*, 357:1133–1136.

Gilmore, R. C., Madau, P., Primack, J. R., et al. (2009). GeV Gamma-ray Attenuation and the High-redshift UV Background. *Monthly Notices of the Royal Astronomical Society*, 399(4):1694–1708.

Goad, M. R., Osborne J. P., Beardmore A. P., and Evans P. A. (2015). GRB 150323A: Enhanced Swift-XRT Position. *GCN Circular 17615*.

Hanna, D. (2007). Calibration Techniques for VERITAS.

Hanna, D., Mccann, A., Mccutcheon, M., and Nikkinen, L. (2009). An LED-based Flasher System for VERITAS.

Hascoët, R., Vurm, I., and Beloborodov, A. M. (2015). Measuring Ambient Densities and Lorentz Factors of Gamma-Ray Bursts from GeV and Optical Observations. *The Astrophysical Journal*, 813(1):63.

Hillas, A. M. (1985). Cerenkov Light Images of EAS Produced by Primary Gamma. *In NASA. Goddard Space Flight Center 19th Intern. Cosmic Ray Conf.*, 3:445–448.

Hinton, J. A. (2004). The Status of the H.E.S.S. Project.

Hjorth, J., Sollerman, J., Møller, P., et al. (2003). A Very Energetic Supernova Associated With the $\gamma$-ray Burst of 29 March 2003. *Nature*, 423(6942):847–850.

Hofmann, W. (2006). Performance Limits for Cherenkov Instruments. *arXiv.org*, astro-ph:3076.

Holder, J. (2015). VERITAS: HAWC's Neighbour to the North.

Holder, J., Aliu, E., Arlen, T., et al. (2011). VERITAS: Status and Highlights.

Jelley, J. V. (1955). Cerenkov Radiation and Its Applications. *Br. J. Appl. Phys*, 6:227–232.

Kildea, J., Atkins, R., Badran, H., et al. (2007). The Whipple Observatory 10m Gamma-ray Telescope, 1997–2006. *Astroparticle Physics*, 28(2):182–195.

Klebesadel, R. W., Strong, I. B., and Olson, R. a. (1973). Observations of Gamma-Ray Bursts of Cosmic Origin. *The Astrophysical Journal*, 182:L85–L88.

Klepser, S. (2012). A generalized likelihood ratio test statistic for Cherenkov telescope data. *Astroparticle Physics*, 36(1):64–76.

Kouveliotou, C., Meegan, C. A., Fishman, G. J., et al. (1993). Identification of Two Classes of Gamma-ray Bursts. *The Astrophysical Journal*, 413:L101–L104.

Krause, M., Pueschel, E., and Maier, G. (2017). Improved $\gamma$/hadron Separation for the Detection of Faint $\gamma$-ray Sources Using Boosted Decision Trees. *Astroparticle Physics*, 89:1–9.

Krennrich, F., Bond, I. H., Boyle, P. J., et al. (2004). VERITAS: The Very Energetic Radiation Imaging Telescope Array System. *New Astronomy Reviews*, 48(5-6):345–349.

Kumar, P. and Zhang, B. (2015). The Physics of Gamma-ray Bursts and Relativistic Jets. *Physics Reports*, 561:1–109.

Lamb, D. Q. and Reichart, D. E. (2000). Gamma-ray Bursts as a Probe of the Very High Redshift Universe. *The Astrophysical Journal*, 536(1):1–18.

Laskar, T., Berger, E., Zauderer, B. A., et al. (2013). A Reverse Shock in GRB 130427A. *The Astrophysical Journal*, 776(2):119.

Lessard, R. W., Buckley, J. H., Connaughton, V., and Le Bohec, S. (2001). A New Analysis Method for Reconstructing the Arrival Direction of TeV Gamma Rays Using a Single Imaging Atmospheric Cherenkov Telescope. *Astroparticle Physics*, 15(1):1–18.

Li, T.-P. P. and Ma, Y.-Q. Q. (1983). Analysis Methods for Results in Gamma-ray Astronomy. *Astrophysical Journal*, 272:317–324.

Liang, E. and Zhang, B. (2005). Modelindependent Multivariable GammaRay Burst Luminosity Indicator and Its Possible Cosmological Implications. *The Astrophysical Journal*, 633(2):611–623.

Lu, C. (2013). Improving the H.E.S.S. Angular Resolution Using the Disp Method. *eprint arXiv:1310.1200*.

Maier, G. (2007). Monte Carlo Studies of the VERITAS Array of Cherenkov telescopes.

Maselli, a., Melandri, a., Nava, L., et al. (2014). GRB 130427A: a Nearby Ordinary Monster. *Science (New York, N.Y.)*, 343(January):48–51.

McEnery, J. E., Michelson, P. F., Paciesas, W. S., and Ritz, S. (2012). Fermi Gamma-Ray Space Telescope. *Optical Engineering*, 51(1):011012.

Meegan, C., Lichti, G., Bhat, P. N., et al. (2009). The Fermi Gamma-ray Burst Monitor. *The Astrophysical Journal*, 702(1):791–804.

Nakar, E. (2007). Short-hard Gamma-ray Bursts. *Physics Reports*, 442(1):166–236.

Paciesas, W. S., Meegan, C. A., Pendleton, G. N., et al. (1999). The Fourth BATSE Gammaray Burst Catalog (Revised). *The Astrophysical Journal Supplement Series*, 122(2):465–495.

Pačiesas, W. S. and S., W. (2004). The BATSE Gamma-ray Burst Legacy. *Baltic Astronomy, Vol. 13, p. 187-192*, 13:187–192.

Paczynski, B. (1995). How Far Away Are Gamma-Ray Bursters? *Publications of the Astronomical Society of the Pacific*, 107:1167–1175.

Panaitescu, A. and Kumar, P. (2001). Fundamental Physical Parameters of Collimated Gamma-Ray Burst Afterglows. *The Astrophysical Journal*, 560(1):L49–L53.

Park, N. (2015). Performance of the VERITAS Experiment.

Pawitan, Y. (2013). *In All Likelihood: Statistical Modelling and Inference Using Likelihood*. OUP Oxford.

Perley, D. A. and Cenko, S. B. (2015). GRB 150323A: Keck Redshift. *GCN Circular 17616*.

Rolke, W. A., López, A. M., and Conrad, J. (2005). Limits and Confidence Intervals in the Presence of Nuisance Parameters. *Nuclear Instruments and Methods in Physics Research Section A: Accelerators, Spectrometers, Detectors and Associated Equipment*, 551(2):493–503.

Röver, C., Messenger, C., and Prix, R. (2011). Bayesian Versus Frequentist Upper Limits.

Ruderman, M. (1975). Theories of Gamma-ray Bursts. *Annals of the New York Academy of Sciences*, 262(1 Seventh Texas):164–180.

Sahakian, V., Aharonian, F., and Akhperjanian, A. (2006). Cherenkov Light in Electron-induced Air Showers. *Astroparticle Physics*, 25(4):233–241.

Sari, R., Piran, T., and Narayan, R. (1998). Spectra and Light Curves of Gamma-ray Burst Afterglows. *The Astrophysical Journal*, 497(1):L17–L20.

Sentürk, G. (2011). The Disp Method for Analysing Large Zenith Angle Gamma-ray Data. *ArXiv e-prints*, pages 1–3.

Sentürk, G. D. (2013). *Observational Properties of Gigaelectronvolt-Teraelectronvolt Blazars and the Study of the Teraelectronvolt Blazar RBS 0413 with VERITAS*. PhD thesis.

Shayduk, M. (2013). Optimized Next-neighbor Image Cleaning Method for Cherenkov Telescopes.

Sironi, L. and Spitkovsky, A. (2011). Particle Acceleration in Relativistic Magnetized Collisionless Electron-ion Shocks. *The Astrophysical Journal*, 726(2):75.

Smith, A. J. (2015). HAWC: Design, Operation, Reconstruction and Analysis.

Sobczyńska, D. (2007). Natural Limit on the $\gamma$/hadron Separation for a Stand Alone Air Cherenkov Telescope. *Journal of Physics G: Nuclear and Particle Physics*, 34(11):2279–2288.

Spengler, G. (2015). Significance in Gamma Ray Astronomy With Systematic Errors. *Astroparticle Physics*, 67:70–74.

St Marie, L. (2014). The Disp Method for Reconstructing Gamma-ray Source Direction With VERITAS. Technical report.

Stephens, M. A. (1974). EDF Statistics for Goodness of Fit and Some Comparisons. *Journal of the American Statistical Association*, 69(347):730–737.

Tamm, I. (1939). Radiation Emitted by Uniformly Moving Electrons. *Journal of Physics USSR*, 1(1):439–454.

Tang, Q.-W., Peng, F.-K., Wang, X.-Y., and Tam, P.-H. T. (2015). Measuring the Bulk Lorentz Factors of Gamma-ray Bursts With Fermi. *The Astrophysical Journal*, 806(2):194.

Vacanti, G., Fleury, P., Jiang, Y., et al. (1994). Muon Ring Images With an Atmospheric Čerenkov Telescope. *Astroparticle Physics*, 2(1):1–11.

VERITAS Collaboration (2017). A Strong Limit On the VHE Emission of GRB 150323A (in preparation).

Vurm, I. and Beloborodov, A. M. (2016). On the Prospects of Gamma-ray Burst Detection in the TeV Band.

Vurm, I., Hascoët, R., and Beloborodov, A. M. (2014). Pair-dominated GeV-optical Flash in GRB 130427A. *The Astrophysical Journal*, 789(2):L37.

Weekes, T. C. (2006). Revealing the Dark TeV Sky: The Atmospheric Cherenkov Imaging Technique for Very High Energy Gamma-ray Astronomy. *Proceedings of the International Workshop on "Energy Budget in the High Energy Universe"*, pages 1–21.

Weekes, T. C., Cawley, M. F., Fegan, D. J., et al. (1989). Observation of TeV Gamma Rays From the Crab Nebula Using the Atmospheric Cerenkov Imaging Technique. *Astrophysical Journal*, 342:379–395.

Weinberg, S. (1995). *The Quantum Theory of Fields*. Cambridge University Press.

Weiner, O. M. (2015). A New Time-dependent Likelihood Technique for Detection of Gamma-ray Bursts With IACT Arrays.

Weinstein, A. (2007). The VERITAS Trigger System.

Wilks, S. S. (1938). The Large-Sample Distribution of the Likelihood Ratio for Testing Composite Hypotheses. *The Annals of Mathematical Statistics*, 9(1):60–62.

Zhang, B. and Kobayashi, S. (2005). GammaRay Burst Early Afterglows: Reverse Shock Emission from an Arbitrarily Magnetized Ejecta. *The Astrophysical Journal*, 628(1):315–334.

Zitzer, B. (2013). The VERITAS Upgraded Telescope-Level Trigger Systems: Technical Details and Performance Characterization.